รายงานวิจัยฉบับสมบูรณ์

โครงการ การประมาณระดับพลังงานของ Li-Ion แบตเตอรี่แบบเวลาจริงด้วยระบบจำลองสำหรับระบบพลังงานแบบไฮบริด (Model-Based Real-Time Estimation of Li-Ion Battery Energy Level for Optimal Control of Hybrid Energy System)

โดย

ดร.เกษมศักดิ์ อุทัยชนะ
มหาวิทยาลัยเชียงใหม่

มิถุนายน 2555

(ปกใน)

รายงานวิจัยฉบับสมบูรณ์

โครงการ การประมาณระดับพลังงานของ Li-Ion แบตเตอรี่แบบเวลาจริงด้วยระบบจำลองสำหรับระบบพลังงานแบบไฮบริด
(Model-Based Real-Time Estimation of Li-Ion Battery Energy Level for Optimal Control of Hybrid Energy System)

โดย

ดร.เกษมศักดิ์ อุทัยชนะ
มหาวิทยาลัยเชียงใหม่

มิถุนายน 2555

สัญญาเลขที่ MRG5380011

รายงานวิจัยฉบับสมบูรณ์

โครงการ การประมาณระดับพลังงานของ Li-Ion แบตเตอรี่แบบเวลาจริงด้วยระบบจำลองสำหรับระบบพลังงานแบบไฮบริด

(Model-Based Real-Time Estimation of Li-Ion Battery Energy Level for Optimal Control of Hybrid Energy System)

ผู้วิจัย ดร.เกษมศักดิ์ อุทัยชนะ
สังกัด ภาควิชาวิศวกรรมไฟฟ้า มหาวิทยาลัยเชียงใหม่

สนับสนุนโดยสำนักงานกองทุนสนับสนุนการวิจัย

กิตติกรรมประกาศ (ACKNOWLEDGEMENT)

ผู้วิจัยและคณะขอขอบคุณเงินทุนอุดหนุนจากสำนักงานกองทุนสนับสนุนการวิจัย ระหว่างปี 2553-2555 นอกจากนี้ยังขอขอบคุณภาควิชาวิศวกรรมนิวเคลียร์และภาควิชาวิศวกรรมไฟฟ้าและคอมพิวเตอร์ Purdue University ที่ให้ความอนุเคราะห์ในข้อมูลด้านการทดสอบการใช้งานของแบตเตอรี่ในโครงข่ายเซนเซอร์ไร้สาย จนชิ้นงานวิจัยนี้สำเร็จไปได้ด้วยดี

ขอขอบคุณกระทรวงวิทยาศาสตร์และเทคโนโลยีที่ให้ความช่วยเหลือด้านเงินทุนการศึกษาและการวิจัยผู้วิจัยมาตั้งแต่ปี 2538

ABSTRACT

Project Code : MRG5380011

Project Title : Model-Based Real-Time Estimation of Li-Ion Battery Energy Level for Optimal Control of Hybrid Energy System

Investigator : Dr. Kasemsak Uthaichana, Electrical Engineering Department, Faculty of Engineering, Chiang Mai University

E-mail Address : uthaichana@gmail.com, kasemsak@chiangmai.ac.th

Project Period : June 2010 – June 2012

In this paper, we develop a non-chemical based input-output battery power model for control purpose, as the information on battery state-of-charge and expected battery lifetime, is essential for mobile applications such as in a parallel hybrid electric vehicle (HEV), wireless sensor network (WSN), etc. First, the battery model is developed for solving the power management control problem (PMCP) in an internal combustion engine (ICE) based parallel HEV. The PMCP consists of a supervisory dynamical model, and a performance index (PI) with two modes of operations consistent with the electric drive (ED) modes interfaced with the battery. The PI mainly penalizes the fuel consumption. The first approach to solve for the power-split strategy is obtained by creating the embedded optimal control problem (EOCP) from the original switched system. The direct collocation and the nonlinear predictive control technique (NMPC) in conjunction with and a sequential quadratic programming (SQP) approach is used to compute the numerical solutions to the PMCP. The performance is evaluated against various driving profiles.

Next, we illustrated that with properly tuned parameter values the model can be extended to different battery types including the Li-ion. The validation results of the model against measured data in terms of power and efficiency at different temperatures are then presented. The model is incorporated with the recovery effect for accurate lifetime estimation. The obtained lifetime estimation results using the proposed model are similar to the standard battery model on a given set of typical loads at room temperature. A possible incorporation of the cycling effect, which determines the battery life or the state of health (SOH), is also suggested. The usage of the proposed model is computationally inexpensive, hence implementable in many applications, such as, low power system design, real time energy management in distributed sensor network, etc. The obtained model structure can be easily extended to other battery types to result in a model that is relatively simple to use and yet can sufficiently describe the battery SOC.

Keywords : ***Li-Ion Battery, Hybrid Electric Vehicle, Estimation, Optimal Control***

บทคัดย่อ

รหัสโครงการ : MRG5380011

ชื่อโครงการ : Model-Based Real-Time Estimation of Li-Ion Battery Energy Level for Optimal Control of Hybrid Energy System

ผู้วิจัย และ สังกัด : Dr. Kasemsak Uthaichana, Electrical Engineering Department, Faculty of Engineering, Chiang Mai University

อีเมลล์ : uthaichana@gmail.com, kasemsak@chiangmai.ac.th

ระยะเวลาโครงการ : June 2010 – June 2012

แบบจำลองในตัวแปรอินพุตและเอาท์พุตสำหรับการควบคุมที่ไม่ได้ใช้หลักของสมการด้านปฏิกิริยาทางเคมีได้ถูกสร้างขึ้นมาเพื่อที่จะคำนวณสถานะของประจุของแบตเตอรี่ ของแบตเตอรี่มีความสำคัญในชิ้นงานที่เคลื่อนที่เช่น ในรถยนต์ไฮบริด เครือข่ายเซ็นเซอร์ไร้สาย ฯลฯ แบบจำลองแบตเตอรี่จะถูกใช้เพื่อการแก้ปัญหาการควบคุมจัดการกำลังงานในรถเครื่องยนต์ไฮบริดแบบขนาน ปัญหานี้ประกอบไปด้วยแบบจำลองทางพลวัตระดับบัญชาการ ดัชนีวัดสมรรถนะ ที่มีอยู่สองโหมดการทำงานตรงกับโหมดของเครื่องจักรกลไฟฟ้า ที่เชื่อมต่อเข้ากับชุดแบตเตอรี่ โดยส่วนประกอบหลักในดัชนีคือประมาณน้ำมันที่ใช้ วิธีการแรกที่ใช้ในการจัดหากลยุทธ์การจัดแบ่งกำลังงานคือการสร้างปัญหาให้เป็นประเภทการควบคุมเหมาะสมที่สุดแบบฝังตัวจากระบบสลับเดิม วิธีการโคโลเคชันแบบตรง และ เทคนิคการควบคุมแบบทำนายไม่เชิงเส้น ร่วมกับการโปรแกรมกำลังสองตามลำดับ ได้ถูกใช้ในการคำนวณหาคำตอบเชิงตัวเลขสำหรับปัญหาการจัดการกำลังงานที่สนใจ โดยสมรรถนะนั้นได้ถูกคำนวณโดยตางการวิ่งแบบต่างๆ จากนั้นแบบจำลองของแบตเตอรี่ที่ได้พัฒนามาสามารถที่จะประยุกต์ใช้กับแบตเตอรี่อื่นๆได้รวมทั้งลิเทียมไอออน ซึ่งเราได้มีการตรวจสอบความถูกต้องของแบบจำลองนี้กับข้อมูลการทำงานจริงที่เก็บได้มา โดยแบบจำลองได้รวมผลของประสิทธิภาพ อุณหภูมิที่แตกต่าง รวมทั้งผลจากการฟื้นสภาพในแบตเตอรี่อีกด้วย และสามารถใช้ในการทำนายค่าอายุของแบตเตอรี่ได้อย่างแม่นยำ โดยได้มีการเปรียบเทียบการทำงานของแบบจำลองนี้กับ แบบจำลองมาตรฐานเมื่อเทียบกับตารางการวิ่งแบบต่างๆ นอกจากนี้เรายังได้กล่าวถึงการรวมผลของจำนวนรอบที่ใช้งานเพื่อคำนวณหาสภาพของแบตเตอรี่ เนื่องจากแบบจำลองนี้ใช้การคำนวณไม่มากจึงสามารถนำไปใช้ได้ในงานหลายประเภท เช่น เพื่อการออกแบบให้ใช้กำลังงานให้กำลังงานต่ำ การควบคุมการใช้กำลังงานในโครงข่ายเซ็นเซอร์แบบกระจายตัว นอกจากนี้แบบจำลองที่ได้ยังสามารถถูกนำไปใช้ในการอธิบายการสถานะของประจุในแบตเตอรี่ประเภทอื่นๆได้อีกด้วย

คำสำคัญ แบตเตอรี่ลิเทียมไอออน รถยนต์ไฮบริด การประมาณค่า การควบคุมแบบเหมาะสมที่สุด

บทสรุปสำหรับผู้บริหาร (EXECUTIVE SUMMARY)

รายงานวิจัยฉบับนี้ทำขึ้นมาเพื่อส่งให้สำนักงานกองทุนสนับสนุนการวิจัยตามข้อบังคับของการรับทุนนักวิจัยรุ่นใหม่เมื่อเดือน มิถุนายน 2553 ตามสัญญาเลขที่ MRG5380011 โดยมีกำหนดระยะเวลาการทำวิจัย 2 ปีบัดนี้งานวิจัยเรื่อง การประมาณระดับพลังงานของ Li-Ion แบตเตอรี่แบบเวลาจริงด้วยระบบจำลองสำหรับระบบพลังงานแบบไฮบริด (Model-Based Real-Time Estimation of Li-Ion Battery Energy Level for Optimal Control of Hybrid Energy System) ได้ดำเนินการมาเสร็จสิ้นแล้ว

สาระสำคัญในงานวิจัยชิ้นนี้คือการสร้างแบบจำลองสำหรับการประมาณค่าระดับประจุไฟฟ้าในแบตเตอรี่ที่มีความแม่นยำและมีรูปแบบที่ไม่ซับซ้อนเกินไปและมีความเหมาะสมในการใช้งานทางด้านการควบคุมโดยเฉพาะระบบกำลังงานแบบไฮบริด ซึ่งแบบจำลองที่ได้สามารถนำไปประยุกต์ใช้ได้กับแบตเตอรี่หลายประเภท เช่น ตะกั่วกรด ลิเทียมไอออน นิเกิลเมททอลไฮดราย ฯลฯ และได้มีการนำแบบจำลองนี้ไปใช้เพื่อการจัดการกำลังงานแบบเหมาะสมที่สุดในระบบรถยนต์แบบไฮบริด

โดยนอกจากรายงานวิจัยฉบับนี้แล้ว ผลลัพธ์ที่ได้จากโครงการวิจัยชิ้นนี้คือ ผลงานวิชาการที่ได้รับการตีพิมพ์ในวารสารระดับนานาชาติ 1 ฉบับ และ ผลลัพธ์อื่นๆคือ ผลงานวิชาการที่ได้นำเสนอในระดับนานาชาติ

ดร.เกษมศักดิ์ อุทัยชนะ
คณะวิศวกรรมศาสตร์ มหาวิทยาลัยเชียงใหม่
ผู้จัดทำรายงาน

สารบัญเนื้อหา (TABLE OF CONTENTS)

สารบัญตาราง (LIST OF TABLES)

สารบัญรูปภาพ (TABLE OF FIGURES)

1. INTRODUCTION AND OBJECTIVES

1.1 Introduction

Batteries are widely used as a finite source of energy for a variety of applications ranging from low-power design of portable devices to high-power hybrid electric vehicle (HEV). Battery performance is affected by various factors such as operating temperature, humidity, discharging/charging cycles, etc. This creates a need for battery models that capture essential application dependent characteristics of real batteries to estimate/predict battery behavior under various operation conditions of charge/discharge. Battery models are also essential for any battery-powered system design that aims at extending the battery's expected life and in battery power management especially in the hybrid propulsion system.

In a hybrid propulsion system, power distribution from two or more energy sources/storages coordinate to deliver the performances demanded by the drivers while considering fuel efficiency and operational constraints. In a parallel hybrid electric vehicle (PHEV), the power demand can be delivered by the main power converter and/or the energy-storage device. Such energy storage devices could be batteries with or without supercapacitors [1, 2]. Examples of main power converters are internal combustion engines (ICEs), fuel cells [3-7], etc. In any case, as illustrated in [8-11], the power distribution among the main PHEV subsystems is computed at the supervisory level. The model of the PHEV at the supervisory level in this investigation is represented as a bi-modal switched system.

The description of the PMCP for constructing the model-based control strategies consists of the PHEV dynamical model, and a performance index (PI), both of which are formulated at the supervisory level. Approaches to solve the PMCP in the literatures can be categorized according to computational requirements as the real-time implementable type, and the global optimal type. The dynamic programming (DP) approaches compute optimal solutions over the driving cycles [10-12]. Thank to the recent advances in optimization, approximation approaches have been adopted and alleviated this problem [13, 14]. Since full knowledge on driving cycles is still required, the control implementation using DP is not real-time implementable. Nevertheless, the results can be used as benchmarks for comparing the degree of the optimality under repeated driving conditions.

Real-time implementable control strategies for the HEV, not optimal over driving cycles, usually undergo fine-tuning on the actual vehicles for desired performances under various assumptions and driving conditions. The list includes but not limited to classical instantaneous/static optimization, adaptive equivalent fuel consumption minimization strategy (A-ECMS) [9], simplified rule based , fuzzy logic based [1, 15, 16], neural network based [3].

The Nonlinear Model Predictive Control (NMPC) technique can provide suboptimal solution with respect to the PI over the predictive-window. The degree of the optimality of the NMPC is bounded by the instantaneous and the global optimization. Note that the NMPC still requires a few predictive window (preview) of the driving profile, but not as extensive as the dynamic programming approach. The problem underlying the NMPC strategy for PMCP [17] is a mixed integer optimization problem, e.g., [18], which is computationally expensive. The embedding technique in [19] is adopted formulate the PMCP as an (convex) embedded optimal control problem, EOCP, from the original (non-convex) switched optimal control problem, SOCP. Hence, the degree of complexity for the embedded version of the NMPC problem is lower.
Numerical methods for solving optimization problems include single shooting, multiple-shooting and direct collocation [20-23] , etc. Difficulties with the single shooting for the bi-modal PHEV illustrated in [24]. Therein the necessary conditions are used to solve for the optimal controls. A superior version, called multiple shooting method, is adopted to solve an optimization problem in [25]. Instead of dealing with adjoint equations in the multiple-shooting method, the direct collocation is adopted in this investigation. The embedding technique in conjunction with the direct collocation method is used to transform the problem into an NLP. The numerical solution to the NLP is computed using sequential quadratic programming (SQP) over a predictive window. More details on other methodologies to obtain solutions to NMPC problems can be found in [26, 27].

The conversion of chemical energy within the battery into electric energy is a complex electrochemical process. The battery behavior, depending upon the application can be approximated by an empirical model or by highly accurate and complex electrochemical model. Rao et al. [28] classified battery models as (i) Physical models, (ii) Empirical models, (iii) Abstract models, and (iv) Mixed models.

Physical models are also known as electrochemical models [28]. They are highly accurate and involve detailed consideration of electrochemical processes, thermal dynamic process, and the physical construction for both charging/discharging characteristics [29, 30]. The main disadvantages of electrochemical models are that the number of parameters to be carefully selected are large and it is computational expensive. Hence the usage of the physical models in practical applications is limited.

Empirical battery models are easy to configure and are represented by simple mathematical expression [31, 32] with less number of parameters. The parameters are usually obtained as a solution of a least squares problem using charging-discharging data, operating conditions, and physical properties. Empirical models often fail to provide accurate representation/estimation under varying load conditions. On the other hand, abstract models are simplified equivalent representation of electrochemical process within a battery, and their choice is usually application specific. The equivalent representation for example can be in terms of electric circuits [33] or stochastic process [34]. Mixed models are based on high level abstraction, avoiding excessive details of physical laws (for example, electrochemical process) governing battery characteristics which leads to the derivation of a simplified analytical expression. The parameters of simplified analytical expression are derived from the experimental data. The number of parameters to be selected is usually low in mixed models. Rakhmatov and Virudhula [35] and Rong and Pedram [36] battery models are examples of mixed models.

In this research, we show that with appropriately tuned parameters, the battery model can be extended to additional battery types (alkaline, Lithium ion (Li-ion), Nickel-metal hydride (Ni-MH)) and this extension is validated against actual data, i.e., the battery model can be used accurately to represent charge and discharge behavior. By incorporating the recovery effect, the model can be used for battery lifetime estimation under various discharging load conditions. Hence the versatility of the model to different battery types widens its utility for practical applications. For example, in distributed sensor network application, estimation of battery longevity, estimates of scheduled maintenance and battery replacement are some of the key issues in such application [37-39].

The report is organized as follows: First is the discussion on Rakhmatov and Virudhula battery model [35], and the development of nonlinear and partially linearized battery model with recovery is presented next. The relationship between both battery models is also discussed. The validation of the proposed model for different battery types against actual data for both discharging and charging is also illustrated. The application of the proposed model with the incorporated recovery model for Li-ion battery lifetime estimation under varying load conditions is also presented. Then the battery model is used to solve for the PMCP for the PHEV. Finally conclusions and future works are drawn.

1.2 Objectives

The objectives of this study are:

(1.2.1) To estimate the battery SOC during the operation

(1.2.2) To use the above battery information to improve the efficiency in the power management of a hybrid system

2. BATTERY MODELING

Given various forms of battery models, we briefly summarize the Rakhmatov and Virudhula battery model and develop a partially linearized input-output battery powerflow model. The versatility of the battery powerflow model to different type of batteries and its validation against actual data for both charging and discharging are some of the main contributions of the paper. In addition, a differential equation describing the recovery effect is presented.

2.1 Rakhmatov and Virudhula Battery Model

Rakhmatov and Virudhula [35] developed an analytical expression to estimate battery lifetime for various time varying loads by taking into account the changes in the concentration of the electro-active species inside the battery. The model is based on a one-dimensional diffusion process of the concentration of the species, where the concentration of the species at time t, and at distance x from the electrode is denoted by $C(x,t)$. The battery lifetime L is defined as the time at which the concentration at the electrode surface $C(0,t)$ drops from the initial concentration of the species, C^*, to a specific threshold C_{cutoff}. The cutoff concentration C_{cutoff}, depending on the battery type and size, is the concentration level below which no further power can be drawn.

Rakhmatov and Virudhula obtained an analytical expression for the concentration behavior by defining two partial differential equations based on Fick's law as follows:

$$J(x,t) = -D\frac{\partial C(x,t)}{\partial x} \tag{2.1}$$

$$\frac{\partial C(x,t)}{\partial x} = D\frac{\partial^2 C(x,t)}{\partial^2 x} \tag{2.2}$$

where (i) $J(x,t)$ denotes the flux of the species at time $t \in [0,L]$ and at distance $x \in [0,w]$ from the electrode, in which w is length of the battery and (ii) D denotes the diffusion coefficient. The boundary conditions at the electrode surface $x = 0$ based on the Faraday's law, and at the other electrode $x = w$ based on constant concentration, are expressed in terms of the concentration gradient as

$$\frac{i(t)}{nFA} = D\left.\frac{\partial C(x,t)}{\partial x}\right|_{x=0} \tag{2.3}$$

$$0 = D\left.\frac{\partial C(x,t)}{\partial x}\right|_{x=w} \tag{2.4}$$

where F is Faraday's constant, n is the number of electrons involved in the electrochemical reaction at the electrode surface, A is the surface area of the electrode, and $i(t)$ is the discharging current and represents the load on the battery. Throughout this paper, "the electrode" refers to the one that receives the electro-active species, and "the other electrode" refers to the one that generates the species.

It can be shown that an analytical solution for (2.1) and (2.2), at the electrode surface ($x = 0$) with the boundary conditions (2.3) and (2.4) is,

$$C(0,t) = C^* - \frac{1}{vFAw}\left[\int_0^t i(t)\, d\tau + \lim_{\varepsilon \to 0} 2\sum_{m=1}^{\infty}\int_0^{t-\varepsilon} i(t)\, e^{-\frac{\pi^2 D(t-\tau)m^2}{w^2}}\, d\tau\right] \tag{2.5}$$

The details on the derivation of (2.5) are presented in [40]. An observation can be made that the concentration of the species at the electrode surface decreases with time due to the usage ($i(t) > 0$). Once the concentration $C(0,t)$ drops to C_{cutoff} we obtain the measure of battery lifetime L.

In certain applications, it is important to obtain an estimate of the amount of energy consumed and consequently the remaining battery stored energy; this then allows estimates of the battery lifetime given nominal loading profiles. To make the model more amendable to various applications, equation (2.5) has been expressed in terms of battery capacity, α as shown in (2.6).

$$\alpha = \int_0^{\mathrm{L}} \mathrm{i}(\tau)\, \mathrm{d}\tau + 2\sum_{\mathrm{m}=1}^{\infty}\int_0^{\mathrm{L}} \mathrm{i}(t)\, e^{-\beta^2 \mathrm{m}^2 (\mathrm{L}-\tau)}\mathrm{d}\tau \tag{2.6}$$

The first term in (2.6) is the total charge drawn by the load and battery losses. The second term of (2.6) is the unavailable charge left in the battery due the non-uniform distribution of the electro-active species during discharging. Here, the two battery parameters α and β are introduced. The parameter $\alpha = vFAwC^*\left(1 - {C_{cutoff}}\big/{C^*}\right)$

denotes the battery capacity, i.e., the estimated amount of charge used during the battery lifetime and $\beta = \pi\sqrt{D}/w$ denotes the discharge time constant. The values of both parameters depend on the battery type. Note that the non-uniform distribution of the electro-active species in the second term of (2.6) results in lower concentration at the electrode surface $C(0,t)$ than at the other electrode $C(w,t)$. If a rest period is introduced, the non-uniformity decreases over time and more charge are available at the electrode surface, which is a part of the recovery effect. The specific equation capturing this phenomenon is described in [41].

In general, the load, $i(t)$, is unknown and non-constant. Even if known, the nonlinear and random behavior would make the usage of (2.6) numerically difficult. Nevertheless, if $i(t)$ has an average value over small intervals of time, the time varying discharge rate can be approximated by piece-wise constant loads, i.e., $i(t)$ is approximated in the time interval $[0,T]$ by *N*-equal size staircase basis functions as,

$$i(t) \approx \sum_{k=0}^{N-1} I_k \left[U\left(t-t_k\right) - U\left(t-t_{k+1}\right) \right] \tag{2.7}$$

where $U(t)$ is the unit step function.

Given a set of M constant experimental current loads $I_i,\ i=1,\ 2,......M$ and corresponding set of M lifetimes L_i, the battery parameters α and β are selected as a least squares solution minimizing $\sum_{i=1}^{M}\left|\hat{I}_i - I_i\right|^2$, where $\hat{I}_i = \hat{I}_i(\hat{\alpha},\hat{\beta})$ is an estimate of the experimental current load based on the most recent values of $\hat{\alpha}$ and $\hat{\beta}$ within the iteration process.

Given the estimated battery parameters and *N*-step staircase approximation of the load (2.7), the battery lifetime computation involves two steps. The first step is to find the sub-interval ($\Delta T_k = t_{k+1} - t_k,\ k = 1,2,....,N-1$) such that the concentration at the electrode surface $C(0,t_{k+1})$ is below C_{cutoff} at t_{k+1}, i.e., find the subinterval ΔT_k such that $L \in [t_k, t_{k+1}]$. The second step is to determine the smallest t ($t_k \le t < t_{k+1}$) within the sub-interval ΔT_k such that $C(0,t_{k+1}) \approx C_{cutoff}$. The search for the smallest t can be performed using modified secant method, as in [42].

2.2 Development of Nonlinear and Partially Linearized Battery Model

As mentioned earlier, the motivation to solve the power management problem of an HEV led to the development of partially linearized (control-oriented) battery model discussed below. Here, normalized battery energy, denoted by $\overline{W}_{bat}(t)$, is defined as the ratio of the instantaneous stored charge to the maximum stored charge, i.e., $\bar{W}_{bat}(t)=\frac{W_{bat}(t)}{W_{bat}^{\max}}$ where $W_{bat}(t)$ is the instantaneous stored battery energy and $W_{bat}^{\max}$ is the maximum rated storage energy of the battery. $\bar{W}_{bat}(t)$ approximates the state-of-charge of the battery under the reasonable assumption of a relatively constant open circuit battery voltage during operation.

To achieve a dynamic model for measuring the SOC of the battery, we differentiate the normalized stored energy (state) $\bar{W}_{bat}(t)=\frac{W_{bat}(t)}{W_{bat}^{\max}}$ with respect to time to obtain a relationship to the discharging and charging power of the battery:

$$\dot{\bar{W}}_{bat}=\frac{\dot{W}_{bat}(t)}{W_{bat}^{\max}}=-\frac{1}{W_{bat}^{\max}}\eta_{bat}\left(\bar{W}_{bat},P_{bat},v\right)P_{bat}(t) \tag{2.8}$$

where (i) v is the battery mode of operation where $v=0$ means the battery is discharging and $v=1$ means the battery is charging, (ii) $\eta_{bat}\left(\bar{W}_{bat},P_{bat},v\right)$ is a generic efficiency for discharging and charging, and (iii) P_{bat} is the discharging/charging battery power flow (input) as expressed in (2.9). The negative sign in (2.8) indicates decrease in the battery SOC during discharging, while (2.8) becomes positive during charging, as P_{bat} is negative, thereby indicating increase in the battery SOC.

$$P_{bat}(t)=\begin{cases}>0 & \text{Discharging}\\ <0 & \text{Charging}\end{cases} \tag{2.9}$$

In general during discharging, when $0\le P_{bat}(t)<\varepsilon$, where ε is a small threshold and usually negligible compared to the discharging loads, a battery undergoes charge recovery which is described in Section II.D. During battery discharge, the generic efficiency $\eta_{bat}\left(\bar{W}_{bat},P_{bat},v\right)=1/\eta_{bat}^{0}\left(\bar{W}_{bat},P_{bat}\right)>1$, where $\eta_{bat}^{0}<1$ is the actual discharging efficiency. A desired power output causes the battery to discharge more rapidly than what is required to account for losses. On the other hand, during charging $\eta_{bat}\left(\bar{W}_{bat},P_{bat},v\right)=\eta_{bat}^{1}\left(\bar{W}_{bat},P_{bat}\right)<1$, where η_{bat}^{1} is the actual charging efficiency, indicates that more power is needed to overcome losses.

Given this relationship, the approximations of the generic efficiency, $\eta_{bat}\left(\bar{W}_{bat},P_{bat},v\right)$, $v\in\{0,1\}$ as a function of state and input for both cases is done by interpolating a nonlinear function against the downscaled battery efficiency map for $v\in\{0,1\}$. Intuitively observing that generic efficiency curves of a battery appear to have a logarithmic characteristic, the following approximation was empirically determined,

$$\eta_{bat}\left(\bar{W}_{bat}, P_{bat}, v\right) = \ln\left(d_{1,v}\bar{W}_{bat} + d_{2,v}\right) + d_{3,v}P_{bat}(t) + d_{4,v} \tag{2.10}$$

Given appropriate coefficients, an objective of this paper is to show the quality of this approximation for four distinct battery types. The coefficients $d_{k,v}$, $k = 1,...,4$ are chosen to fit the generic battery efficiency map. The coefficients during battery discharging and charging are computed as a solution to a nonlinear least squares regression similar to that described earlier for obtaining parameters of the Rakhmatov and Virudhula model. Specifically, in each mode, the coefficients $d_{k,v}$ for $i = 1,...,4$ are the numerical solutions to the following minimization:

$$\min_{d_i \in R}\left\|\eta_{bat}\left(\bar{W}_{bat}, P_{bat,}v\right) - \ln(d_{1,v}\bar{W}_{bat} + d_{2,v}) + d_{3,v}P_{bat}(t) + d_{4,v}\right\| \tag{2.11}$$

This nonlinear minimization problem is solved via a subroutine *nlinfit* in MATLAB's statistical toolbox in this study.

As per the above development, the differential equation for $\dot{\bar{W}}_{bat}(t)$ is nonlinear in the control input ($P_{bat}(t)$). In order to make the battery model amenable to a large body of control literature, (2.8) is partially linearized about the mode-dependent nominal battery operating power, $P_{bat,nom}^{v}$. The resulting linearized differential equation is:

$$\begin{aligned}\dot{\bar{W}}_{bat}(t) = {} & \frac{d_{3,v}}{W_{bat}^{\max}}\left(P_{bat,nom}^{v}\right)^{2} \\ & -\left[\ln\left(d_{1,v}\bar{W}_{bat}(t) + d_{2,v}\right) + 2d_{3,v}P_{bat,nom}^{v} + d_{4,v}\right]\frac{P_{bat}(t)}{W_{bat}^{\max}}\end{aligned} \tag{2.12}$$

2.3 Relationship between Rakhmatov and Virudhula and Partially Linearized Battery Models

In many practical applications, the actual knowledge about state-of-charge of the battery is essential. In Rakhmatov and Virudhula [35] battery model the concentration of the electro-active species at the electrode surface is given by (5). Since the specific gravity of the electro-active species is greater than that of water, the higher the concentration of electro-species is the higher the specific gravity. When battery is fully charged (SOC = 1), then the concentration in the electrolyte is at its maximum and so is the specific gravity. On the other hand, if the concentration of the species is at C_{cutoff} (SOC $= \in_C \simeq 0$), then the specific gravity is at minimum operating value. In fact, there is a linear relationship between the battery SOC and the specific gravity as shown in [43] under an assumption of uniform concentration of the electro-active species at equilibrium. Based on above discussion, there exists a relationship between the battery SOC and concentration in the Rakhmatov and Virudhula battery model at equilibrium. The battery model approximates the battery SOC as normalized battery energy ($\overline{W}_{bat}$) under the assumption of relatively constant open circuit voltage. This constitutes relationship between the concentration in the Rakhmatov and Virudhula battery model and $\overline{W}_{bat}$ as expressed below.

$$C(t) = \overline{W}_{bat}(t)(C^{*} - C_{cutoff}) + C_{cutoff} \tag{2.13}$$

where $C(t)$ is the concentration of the species. Note that at equilibrium, the concentration of the species is uniform, i.e., $C(0,t) = C(w,t) = C(t)$.

2.4 Battery Recovery Model

The recovery effect is the increase in the state-of-charge, $\overline{W}_{bat}$, due to the adjustment of the concentration gradient towards zero when there is no load on the battery, i.e., $0 \le P_{bat}(t) < \varepsilon$, on the battery, where ε is a small threshold and usually negligible compared to the discharging loads. The recovery effect depends upon the power discharge rate and the battery type. The recovery of the $\overline{W}_{bat}$ reaches its steady state value after a few time constants. However, when the magnitude of the battery discharge load power $P_{bat}(t)$ is less than or equal to ε, the derivative of $\overline{W}_{bat}(t)$ given by the partially linearized model approximately reduces to ${d_{3,v}}\big/{W_{bat}^{\max}}\left(P_{bat,nom}^{v}\right)^{2}$ for $v = 0$. This is not equivalent to the charge recovery effect. Therefore, to achieve a better representation of the battery behavior, we incorporate the recovery effect by augmenting an additional equation below to the partially linearized battery model.

$$\begin{aligned} &\dot{\overline{W}}_{bat}^{r}(t) = -\lambda \overline{W}_{bat}^{r}(t) + (1+\delta)\overline{W}_{bat}(t_i) \\ &0 \le P_{bat}(t) < \varepsilon \end{aligned} \tag{2.14}$$

where (i) $\lambda = 1/\tau$; τ is the recovery time constant, (ii) $\overline{W}_{bat}^{r}(t)$ denotes the state-of-charge of the battery during recovery, (iii) the superscript *r* denotes recovery, and (iv) δ denotes the percentage of recovery whose value depends upon battery type and is usually obtained from experimental data [44] . In (2.14), $\overline{W}_{bat}(t_i)$ denotes the battery SOC level at time t_i, where t_i is the time instance when recovery starts, hence the initial condition of $\overline{W}_{bat}^{r}(t)$ is $\overline{W}_{bat}(t_i)$. The value of λ is computed using the logarithmic approach.

3. PARTIALLY LINEARIZED BATTERY MODEL VALIDATION FOR CHARGING AND DISCHARGING

In this section, we validate the partially linearized battery model developed in Section II.B for different battery types without incorporating the recovery model. The recovery model is not used during validation for charging and discharging because the selected magnitude of the input power (P_{bat}) during validation is greater than the threshold ε. Hence the recovery effect is negligible during validation process. The procedure to validate the partially linearized model without recovery effect for each battery type can be briefly summarized as follows: First, we obtain the battery efficiency data. Second, we estimate the efficiency coefficients $d_{k,v}$ for charging and discharging as described in Section II.B. Finally, we evaluate the quality of the partially linearized model without recovery effect against the actual data by computing the 2-norm normalized error. Specifically, we compute the error between $\dot{\overline{W}}_{bat}$ given by (2.12) at a given $P_{bat,nom}^{v}$ and the actual data for charging and discharging under various loads and SOC.

The validation results during discharging are shown for 30 of 12 Ah 12 V lead-acid, 1.41 W-h Li-ion, 900 mAh Ni-MH, and 2850 mAh alkaline batteries. On the other hand, the validation results during charging for only lead-acid and Li-ion are shown. Since alkaline batteries in the market are mostly non-rechargeable and the data on the internal resistance during charging for rechargeable Ni-MH is not available to us at the time of publication, so we do not validate the approximation of linearized battery model for Ni-MH battery during charging.

3.1 Efficiency Data for Validation

The efficiency data for lead-acid battery is obtained by downscaling the lead-acid battery efficiency maps in [45]. On the other hand, to obtain the efficiency data for Li-ion, Ni-MH, and alkaline batteries, we follow the procedure described in [46]. In [46] the battery is represented by a simple resistive Thevenin equivalent circuit. The internal resistance value is obtained as an average value under various loads for each SOC. The battery efficiency is then obtained as the ratio of the terminal voltage to the open circuit voltage for discharging and vice versa for charging where the voltage difference is due to the losses through the internal resistance.

3.2 Validation Results for Lead-acid and Lithium-ion Batteries

Initially, we present the discharging and charging validation results of the partially linearized battery model without considering the recovery model for 30 of 12 Ah 12 V lead-acid and 1.41 W-h Li-ion batteries. In the case of a 30 of 12 Ah 12 V lead-acid battery, the 2-norm normalized error is 8.06% during discharging, and is 4.78% during charging. The linearized generic battery efficiency approximation during battery discharging is accurate around the nominal input power (15 kW). Similarly, the linearized approximation during battery charging is accurate around the nominal input power (-13 kW). Note that these nominal input power levels for both discharging and charging are selected based on the average battery power flow in the HEV application [45]. In Fig. 1, whose y-axis is $P_{bat}\eta_{bat}$, illustrates the accuracy of the efficiencies from the linearized approximation against actual data for both discharging and charging. The approximation error increases for large excursion from the nominal input power level as shown in Fig. 1 as expected. Since the partially linearized battery model was initially developed for an HEV application, the range of SOC was restricted between 0.4 and 0.8. This is due to the fact that the discharging efficiency deteriorates below the SOC of 0.4, and the charging becomes inefficient above the SOC of 0.8. However, it is shown in the case of other battery types that the model is not limited by the restriction on the range of SOC as shown in the case of lead-acid battery.

In the case of a 1.41 W-h Li-ion battery, the same validation procedure is applied. The 2-norm normalized error for discharging is 3.45% and for charging is 1.85%. The approximation of the linearized battery model is accurate around the input nominal power level of 283 mW for discharging and -250 mW during charging, as shown in Fig. 2. The approximation error increases during both discharging and charging as the load power level deviates from respective nominal power level, but not significantly over the range for both batteries.

The coefficients used to validate the linearized approximation during discharging and charging for both 30 of 12 Ah 12 V lead-acid and 1.41 W-h Li-ion batteries are summarized in Table I.

3.3 Validation Results for Nickel-Metal Hydride and Alkaline Batteries

We now present the validation result of partially linearized battery model for 900 mAh Ni-MH and 2850 mAh alkaline batteries during discharge alone. Since alkaline batteries are mostly non-rechargeable and the data on the internal resistance during charging for rechargeable Ni-MH is not available to us at the time of publication, so we do not validate the approximation of partially linearized battery model for Ni-MH battery during charging.

Table I. Battery Parameters For The Nonlinear Efficiency Approximation For Both Discharging and Charging

Mode	Battery	Coefficients			
		$d_{1,v}$	$d_{2,v}$	$d_{3,v}$	$d_{4,v}$
Discharging ($v = 0$)	Lead-acid	-0.3550	1.830	0.0075	0.4660
	Li-ion	0.0034	0.5238	-0.0598	1.6433
Charging ($v = 1$)	Lead-acid	-0.0999	0.6220	0.0089	1.530
	Li-ion	-0.0033	0.5251	0.0290	1.647

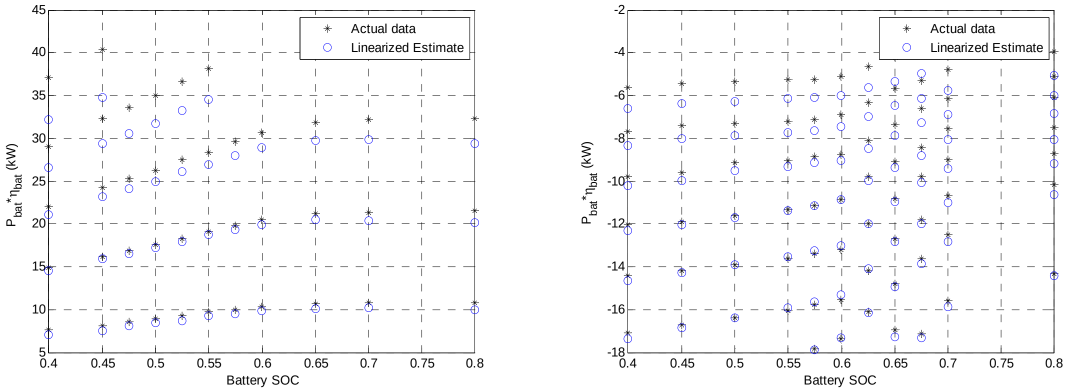

(a) (b)

Fig. 1 Linearized approximation of 30 of 12 Ah 12 V lead acid battery during (a) battery discharging around nominal power of 15 KW and (b) battery charging around nominal power of -13 KW.

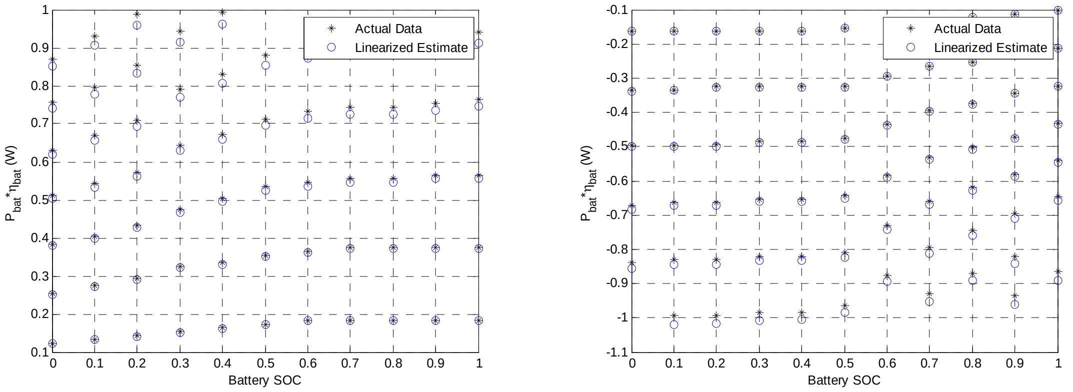

(a) (b)

Fig. 2 Linearized approximation of 1.41 W-h Li-ion battery during (a) battery discharging around nominal power of 253 mW and (b) charging around nominal power of -250 mW.

Figs. 3(a) and 3(b) show the accuracies of the battery model for Ni-MH and alkaline which is linearized about nominal input power levels of 250mW and 125mW respectively. The 2-norm normalized error is 2.26% and 1.23% for Ni-MH and alkaline batteries respectively. In Figs. 3(a) and 3(b), a similar accuracy pattern over the range of battery power is observed. The coefficients used to validate the linear approximation during discharging for 900 mAh Ni-MH and 2850 mAh alkaline are listed in Table II.

The linearized approximation of the battery captures the fact that battery efficiency decreases as SOC decreases and battery input power increases. This is consistent with the behavior of the battery efficiency maps.

4. LITHIUM-ION BATTERY LIFETIME ESTIMATION USING PARTIALLY LINEARIZED MODEL WITH RECOVERY

In this section, we present the description of typical power load usage during battery operation and numerical estimation of 1.41 W-h Li-ion battery lifetime using the partially linearized model during discharging ($v = 0$) with the incorporated recovery model. The actual lifetime measurements on a real 1.41 W-h Li-ion battery for various typical load usages are not available. The DUALFOIL simulator [30], which numerically solves set of partial differential equations governing the chemical reaction in the rechargeable Li-ion batteries, can be used to obtain lifetime estimates of 1.41 W-h Li-ion battery for a given set of typical power loads.

Table II. Battery Parameters For The Nonlinear Efficiency Approximation For Discharging Alone ($v = 0$)

Mode	Battery	Coefficients			
		$d_{1,v}$	$d_{2,v}$	$d_{3,v}$	$d_{4,v}$
Discharging ($v = 0$)	Ni-MH	0.0023	0.5240	-0.0761	1.6440
	Alkaline	0.0344	0.8360	-0.4086	1.0690

However, we do not use DUALFOIL simulator because it is a cumbersome processes to appropriately choose over 50 parameters in order to obtain accurate simulation results. Therefore, to estimate the lifetime of 1.41 W-h Li-ion battery, we downscale the power loads used during the actual lifetime measurement of same type 2.2 W-h Li-ion battery in [40]. Under the downscaling assumption, (see Appendix B), the lifetime of 2.2 W-h Li-ion battery subject to typical power loads summarized in Tables III and IV and the lifetime of 1.41 W-h Li-ion battery subject to downscaled typical power loads also summarized in Tables III and IV must be the same.

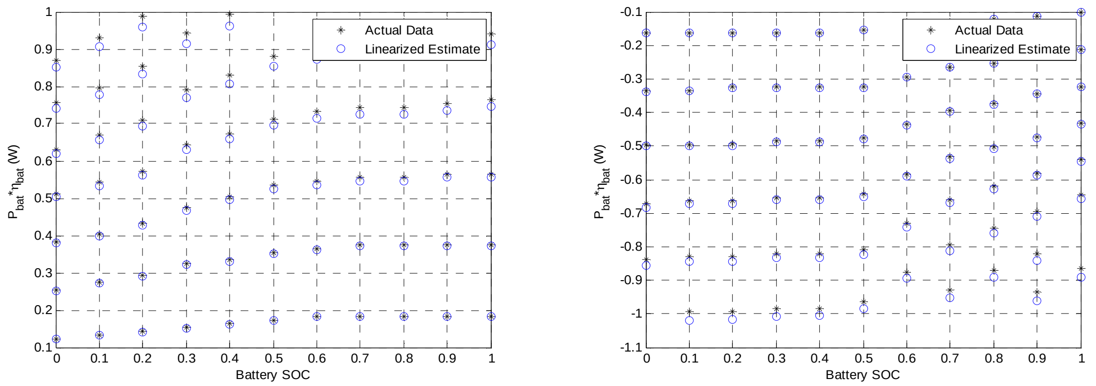

(a) (b)

Fig. 3 Linearized approximation during discharging for (a) 900 mAh Ni-MH around nominal power of 250 mW and (b) 2850 mAh alkaline around nominal power of 125 mW.

We compare the aforementioned actual battery lifetime with the estimate obtained using the battery model in previous sections and with the estimate obtained using the Rakhmatov and Virudhula battery model.

In general, the battery open-circuit voltage, V_{oc}, is a function of battery state-of-charge and operating temperature. In this paper, all the computation assumes room temperature. Initially, $\overline{W}_{bat}(t=0)=1$ corresponds to fully charged battery with the initial open-circuit voltage, $V_{oc}=V_{oc}^{*}$, while $\overline{W}_{bat}(t=L)=0$ corresponds to V_{oc} dropping to the cut-off voltage (V_{cutoff}). The value of V_{oc}^{*} and V_{cutoff} depends upon the battery type. So under a typical load, battery V_{oc} drops to V_{cutoff} over time. Hence, the battery lifetime L can also be defined as the time taken by battery V_{oc} to drop to V_{cutoff} below which no power (current) can be further drawn from the battery. This definition is consistent with the battery lifetime definition in Section II.A, i.e., the time duration during which the concentration of the electro-active species drops from its initial concentration, C^{*}, to a specific threshold C_{cutoff}.

4.1 Description of Typical Power Load Usage

The typical power loads (both constant and varying) used in this paper are the average power consumed during various operating modes of the “Itsy” pocket computer which is powered by a 2.2 W-h Li-ion battery [40, 47]. The power loads used to estimate battery lifetime in this paper were taken from [47] in which the power consumption of Itsy pocket computer were reported. Let P represent a set consisting of various actual average power loads (both constant and varying). The set P is divided into two subsets, $\mathrm{P_T}$ and $\mathrm{P_C}$ where the subset $\mathrm{P_T}$ consists of 15 constant average power loads and the subset $\mathrm{P_C}$ consists of 7 varying average power loads. The average power loads in both subsets are downscaled and are used to estimate the lifetime of 1.41 W-h Li-ion battery as mentioned earlier. The actual and downscaled power loads are summarized in Tables III and IV were computed using average current and average voltage of 3.75 V [47]. So the lifetimes estimated and measured are average lifetimes. Given the upper and lower bounds on the load values, the models discussed in Section II can be used to estimate upper and lower bounds on the actual lifetimes. From here-onwards, we will refer “average power load” used to estimate battery lifetime as “power load” for simplicity.

In Table III, the constant power loads (T1–T10) represent the power consumed during different operating modes of Itsy computer. In addition, peripheral devices such as Microdrive hard disk and a WaveLAN wireless card were attached to “Itsy”, and power consumptions (T11–T15) were recorded for different operating modes of “Itsy” and peripheral devices [40, 47]. The following letter abbreviations are used to describe the operation modes of Itsy and peripheral devices in Table III.

- Itsy: I – Idle, M – MPEG, D – Dictation, T – Talk, W – WAV1, S – SleepDC.
- Microdrive: S – Standby, A – Access.
- WaveLAN: D – Doze, R – Receive, and T – Transmit.

The power loads in Table IV represent the measured power consumption when Itsy operation is switched between different modes. In Table IV, the second column represents the actual power measurements, the third column represents the downscaled power measurements, and the fourth column represent the time duration in which each power level was measured. Cases C1 and C2 have the same load power levels. However the order in which the battery is subjected to power load is reversed. In case C1, load power is a decreasing staircase function, except for the last period in which the load power jumps up and remains constant. In case C2, load power is an increasing staircase function and that remains constant at the same power value as case C1 during the final period. Case C3 is similar to C2, except it has a rest period of 50 minutes. Case C4 is a periodic repetition of C2 for ten cycles (represented by superscript 10 in Table IV) but the time for each power level is downscaled by a factor of ten (also represented by superscript 10 in Table IV); hence the total load power consumption in Cases C2 and C4 is identical. Case C5 is similar to C4 except that the first two power levels in C5 are lower than the ones in C4. The time interval column in

Table III. Description Of Actual And Downscaled Power Loads Of Subset P_T

Test	Operating Modes	Description	Actual P (mW)	Downscaled P (mW)
T1	MPEG	Video, 206 MHz	835.0	534.4
T2	Dictation	Speech input, 206 MHz	767.0	490.8
T3	Talk 1	Speech output, 206 MHz	406.0	259.9
T4	Talk 2	Speech output, 74 MHz	403.0	258.0
T5	Talk 3	Speech output, 74 MHz LV)	356.0	227.8
T6	WAV 1	Audio, 206 MHz	316.0	202.3
T7	WAV 2	Audio, 59 MHz	283.0	181.2
T8	Idle 1	Operating system, 206 MHz	105.0	67.2
T9	Idle 2	Operating system, 59 MHz	73.0	46.8
T10	Sleep DC	Sleep with a daughter card	11.0	7.2
T11	SSD	SleepDC-Standby-Doze	122.0	78.0
T12	ISD	Idle 1-Standby-Doze	216.0	138.4
T13	WSD	WAV1-Standby-Doze	427.0	273.4
T14	TSD	Talk-Standby-Doze	517.0	330.9
T15	ISR	Idle-Standby-Receive	1096.0	701.4

Table IV. Description Of Actual And Downscaled Varying Power Loads Of Subset P_C

Case	Actual P (mW)	Downscaled varying P (mW)	Time intervals (min)
C1	(835 767 406 316 835)	(534.4 490.8 259.9 202.3 534.4)	(0 50 100 150 200)
C2	(316 406 767 835 835)	(202.3 259.9 490.8 534.4 534.4)	(0 50 100 150 200)
C3	(316 406 767 0 835 835)	(202.3 259.9 490.8 0 534.4 534.4)	(0 50 100 150 200 250)
C4	([316 406 767 835]^{10} 835)	([202.3 259.9 490.8 534.4]^{10} 534.4)	([0 5 10 15]$^{10}_{200}$ 200)
C5	([283 356 767 835]^{10} 835)	([181.2 227.7 490.8 534.4]^{10} 534.4)	([0 5 10 15]$^{10}_{200}$ 200)
C6	(835 0 835)	(534.4 0 534.4)	(0 105.7 140.9)
C7	(1096 0 1096)	(701.4 0 701.4)	(0 74.6 99.5)

Table IV for cases C4 and C5 has a subscript 200 which means that after 10 load cycles the total time duration is 200 minutes. Cases C6 and C7 have different rest periods. Cases C3, C6, and C7 are used to evaluate the recovery effect of the battery since they contain rest period.

The typical power loads summarized in Table III and Table IV represent a broad range of loading condition used to exercises the battery.

4.2 Numerical Estimation of Battery Lifetime

Given the partially linearized battery model during discharging ($v = 0$) with the incorporated recovery model, the discharging coefficients $d_{k,v=0}$, $k = 1,\ldots,4$ in Table I, and various downscaled power loads in Table III and Table IV, a numerical lifetime estimation of 1.41 W-h Li-ion battery is computed in MATLAB. Note that, all the parameters and the downscaled power load profiles used in the lifetime estimation process is for 1.41 W-h Li-ion battery. The downscaled nominal operating input power $P_{bat,nom}$ is 181.2 mW, which is obtained by downscaling the average battery power flow in the Itsy pocket computer. The recovery time constant (λ) computed using the downscaled load data is 0.016 seconds^{-1}. The percentage of recovery δ is selected as 3% because the partially linearized battery model during discharging without the recovery model under-estimated the battery lifetime by 3% on average.

The results of lifetime estimation using the partially linearized battery model during discharging ($v = 0$) with the incorporated recovery model for downscaled power load profiles $\mathrm{P_T}$ and $\mathrm{P_C}$ are summarized in Tables V and VI respectively. Based on the downscaling assumption in Appendix C, the lifetime of 1.41 W-h Li-ion battery computed using the downscaled power loads must be equal to the lifetime of 2.2 W-h Li-ion battery computed (measured) using the actual power loads. Henceforth, the estimated lifetimes of 2.2 W-h Li-ion battery using Rakhmatov and Virudhula battery model [35] for $\mathrm{P_T}$ and $\mathrm{P_C}$ are also summarized in Tables V and VI along with measured lifetimes in the first column. The Rakhmatov and Virudhula battery model parameters: $\alpha = 33706$ and $\beta = 0.750$ reported in [40] is used to estimate battery lifetime. The error between the measured and the estimated lifetime is computed using (2.15) and is also listed in Tables V and VI.

$$\text{Error (\%)} = \frac{\text{Measured Lifetime - Estimated Lifetime}}{\text{Measured Lifetime}} \times 100 \qquad (2.15)$$

4.3 Discussion on the Battery Lifetime Estimation

In this section, we analyze and discuss the performance of the partially linearized model with the incorporated recovery model under varying load conditions. A broad range of selected load profiles used to exercise the battery model in this paper is a real time power consumption of Itsy computer under different operating modes. The typical loads presented in Table III and Table IV captures both static and dynamic nature of the power usage observed in many real time applications. In addition, to lifetime estimation using the partially linearized model with the incorporated recovery model, we also compute the percentage of recovery observed in cases C3, C6 and C7. We define a few terms as in [35]. Let $L_{original}$ represent the estimated lifetime for the power profile when no load relaxation (no rest period) is exercised. When the rest period is present, let ξ denote the rest period in a load profile and let $L_{unaffected}$ denotes the expected lifetime as if no recovery takes place during the rest period of duration ξ, i.e., $L_{unaffected} = L_{original} + \xi$. In general, the lifetime L should be greater than $L_{unaffected}$ due to recovery effect. The quantity $\frac{L - L_{unaffected}}{L_{original}} \times 100\%$ represents the lifetime extension due to recovery effect. Table VII summarizes the recovery percentage (i.e., lifetime extension) obtained by using the partially linearized battery model with the incorporated recovery model.

Cases C3, C6, and C7, having a rest period of 50, 35.2, and 24.9 minutes respectively, show an increase in estimated battery lifetime by 1.6%, 2%, and 2.5% respectively due to recovery effect. These observations ascertain the fact that the partially linearized battery with the incorporated battery model is able to capture the recovery effect. However, the percentage of recovery observed in C3, C6, and C7 can be slightly higher than the actual recovery of real battery. This is due to the fact that the partially linearized model underestimates the power losses when the load power is higher than $P_{bat,nom}$ as shown in Fig. 2. In general, the battery recovery has more profound effect when the power discharge rate is high. Since the power discharge rate in C7 is higher than one in C6, C7 exhibits higher percentage recovery as indicated in Table VII.

Table V. Measured And Estimated Lifetime For Each Constant Power Load

Measured		Rakhmatov and Virudhula Model		Partially linearized Model	
Test	min	min	Error (%)	min	Error (%)
T1	141.0	139.9	0.8	152.7	8.3
T2	156.6	156.0	0.0	166.3	6.6
T3	307.8	331.4	7.6	319.8	3.9
T4	312.0	334.1	7.1	324.2	3.9
T5	358.2	384.0	7.2	368.9	3.0
T6	397.2	437.5	10.2	406.3	2.3
T7	448.2	493.3	10.1	455.4	1.6
T8	1248.0	1400.0	12.2	1264.2	1.3
T9	1818.0	2029.0	11.6	1839.8	1.2
T10	12690.0	13417	5.8	13566.6	7.7
T11	1069.0	1032.0	3.5	1080.8	1.1
T12	592.4	579.7	2.1	593.6	0.02
T13	293.5	290.5	1.0	306.7	4.5
T14	240.8	239.0	0.8	256.2	6.4
T15	110.7	109.9	0.7	120.1	8.5

Table VI. Measured And Estimated Lifetime For Each Constant Power Load

Measured		Rakhmatov and Virudhula Model		Partially linearized Model	
Case	min	min	Error (%)	min	Error (%)
C1	208.6	206.8	0.9	212.3	1.8
C2	207.4	206.7	0.3	210.9	1.7
C3	257.6	258.7	0.4	264.3	2.6
C4	209.3	206.7	1.2	214.1	2.3
C5	213.7	211.7	0.9	219.3	2.6
C6	182.7	181.1	0.9	191.0	4.5
C7	136.0	134.8	0.8	148.0	8.8

Intuitively, battery at a higher state-of-charge must be able to handle large power load better against the battery at a lower state-of-charge. This assists in identifying the power load pattern that would result in better lifetime. The cases C1 and C2 have same power load values except the order in which the battery is subjected to load power is reversed. As expected, the lifetime of C1 is slightly higher than the lifetime of C2. Case C4 is a periodic repetition of an increasing staircase as in C2 for ten cycles but the time for each power level is downscaled by a factor of ten while the total load power consumption in both cases is identical. The battery in case C2 handles high load power at low SOC while in case C4 the battery is subject to periodic variation of both low and high load power at low SOC. As a result, the lifetime estimated in case C4 is slightly better than the lifetime estimated in case C2.

In the case of selected constant loads (Table III), the lifetime estimation widely ranges from 2 hours to 10 days. Table V shows the comparison of the accuracy of the lifetime estimations between the partially linearized model and the chemical based Rakhmatov and Virudhula battery model. The estimation error of the partially linearized battery model is less than 10% for the typical constant loads listed in Table III. We observe that the estimation error increases as the load power level increases or decreases from the nominal input power. This observation is consistent with the assumption made during the linearization of nonlinear battery efficiency and the validation results presented in the previous section. For example, the estimation error for 701.4 mW load power, which is 502.2 mW more than nominal input power, is 8.5 %, while the error for 7.2 mW load power, which is 174 mW less than nominal input power, is 7.7%. In the case of Rakhmatov and Virudhula battery model , the estimation error increases as the load on the battery decreases.

Table VII. Measure of Battery Recovery

Case	$L_{original}$ (min)	$L_{unaffected}$ (min)	L (min)	Recovery (%)
C3	210.9	260.9	264.3	1.6
C6	152.7	187.9	191.0	2.0
C7	120.1	145.0	148.0	2.5

Based on the numerical results presented above, we observe that the input-output partially linearized model with incorporated recovery model provides reasonably accurate lifetime estimation in comparison to the estimation result obtained from Rakhmatov and Virudhula model.

At this point, we have obtained the sufficiently accurate and appropriate battery model in terms of input-output power flow to/from the battery pack. The next step is to apply this information to the hybrid power system in the HEV, as shown in the next section.

5. SOLVING THE POWER MANAGEMENT CONTROL PROBLEM FOR HYBRID ELECTRIC VEHICLE

In the hybrid propulsion system such as in the HEV, the computation at the supervisory level is done based on the presumption that the desired power level can be implemented at the subsystem level. The local closed loop controllers must track the corresponding reference power demand thereby decoupling the supervisory and local level control problems. Hence, the modeling at the supervisory level should reflect the closed loop behaviors of subsystems.

5.1. Summary of Considered Hardware Descriptions

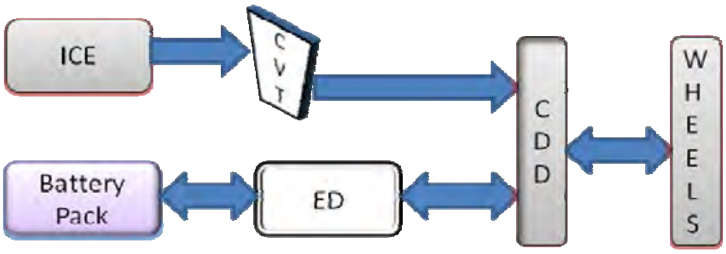

Fig. 4 Power flow diagram of PHEV in this study

The main power source in this investigation is the 1.9 L ICE, coupled to the driveshaft through a continuously variable transmission (CVT) (and clutch in the post-transmission configuration. Thirty 13Ah 12V, lead-acid batteries in series is interfaced with a 30 kW induction ED. Hotel loads are handled by a traditional engine-based charging system. The coupling device and differential (CDD) is the summing junction, for redirecting the power flow among the ICE-CVT, battery-ED, and the wheels. Fig. 4 illustrates power distributions among the main subsystems.

5.2. Modes of Operation

In [11], five modes of operation describe the essential behavior of the PHEV. Since the PMCP complexity increases exponentially with increased numbers of modes [48, 49], an effort is put in this investigation to reduce the number of modes at the supervisory level.

Through careful consideration of the dynamics in each mode of operation, the essential behavior can be approximated using only two modes. As a preview, the mode reduction concept from five-to-two is illustrated via the numerical results obtained in this study in

Fig. 5. In

Fig. 5, $P_{ED} + P_{ICE} = P_{load}$, i.e., the sum of ED power, and the ICE power is delivered to the load (the planetary efficiency is ignored for now).

The details of the mode reduction concept, when the HEV is operating, can be described as follows:

For $v = 0$ $(P_{ED} \geq 0)$: the engine-only mode $(P_{ICE} > 0, P_{ED} = 0)$ corresponds to zero power flow from the ED which can be achieved by a zero-value of the ED control variable; the motor only mode $(P_{ICE} = 0, P_{ED} > 0)$ corresponds to no power flow from the ICE that is also achievable by a zero-value of the engine control variable; in motor assisted mode $(P_{ICE} > 0, P_{ED} > 0)$ both ICE power and ED power are strictly positive to the wheels achievable by non-zero control variables of the ED and ICE.

For $v = 1$ $(P_{ED} < 0)$: the regenerative-braking mode $(P_{load} < 0, P_{ED} < 0)$ corresponds to a reverse of the ED power flow to charge the battery with ICE power at zero (or nearly so); and the engine-charging-battery mode $(P_{ICE} > 0, P_{ED} < 0)$ corresponds to the case when the ED operates as a generator with positive ICE power flow to the ED and possibly to the wheels.

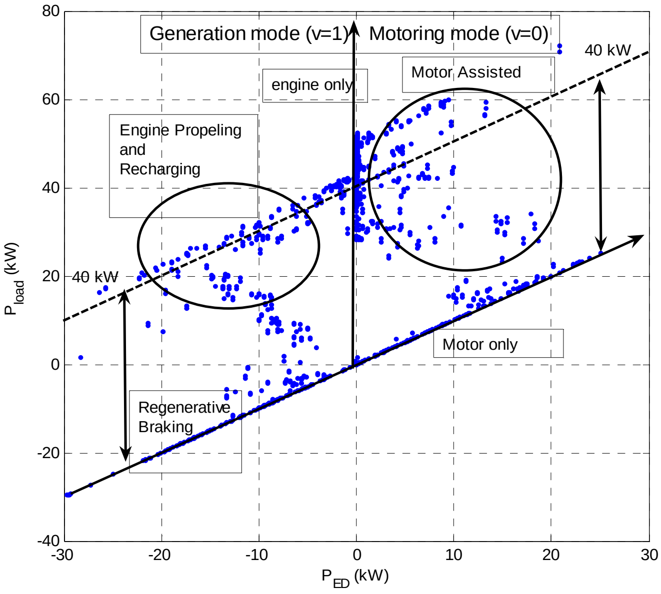

Fig. 5 Power Flow strategy obtained in this study using NMPC tracking EPA highway profile showing the concept of mode reduction from five-to-two

It can be seen that the two modes of operation at the supervisory level coincide with the modes of the ED denoted (using superscripts) as $v=0$ (motoring) and $v=1$ (generating). The summary of bi-modal switched system describing the essential dynamics of the power-flow at the supervisory level is given next.

5.3 HEV State Model Overview

The summary of the modeling equations, detailed in [45, 50], are summarized in this subsection. The input-output power relationships of subsystems consist of algebraic and dynamical equations. The input-output relationship is considered algebraic when the its internal powerflow dynamics are much faster than others. The essential dynamical state is

$$x(t) \triangleq \left[P_{ICE}, SOC, V\right]^T \tag{5.1}$$

where P_{ICE} is the ICE power, SOC is the battery state-of-charge, and V is the longitudinal vehicle's velocity. The mode-dependent nonlinear state equation for the PHEV in this study is:

$$\dot{x}(t) = f_{v(t)}(x(t), u_{v(t)}(t)) \tag{5.2}$$

where $f_v(\cdot)$ denotes the dynamics in the motoring, $v=0$, or generating mode, $v=1$. The modulating control in modes-0/1 are

$$\begin{aligned} u_{0/1}(t) = \left[u_{ICE}(t), u_{FR}(t), u_{EM/GEN}(t)\right]^{\mathrm{T}} \\ \in \Omega \subset \mathbb{R}^3 \end{aligned} \tag{5.3}$$

where (i) the compact and convex set,

$$\Omega = [0,1]\times[0,1]\times[0,1] \tag{5.4}$$

(ii) $u_{ICE}(t) \in [0,1]$ modulates the maximum available ICE power; (iii) $u_{FR}(t)$ modulates the maximum frictional braking; and (iv) $u_{EM/GEN}(t) \in [0,1]$ modulates the maximum available ED power in the mode-0 and mode-1, respectively.

The motivation for this control structure is four-fold. First, the model is scalable in terms of numbers of power sources (ICE's or ED's) so that the corresponding increase in the number of operating modes leads to only a polynomial increase in complexity for numerical optimization methods [51]. Second, the model has a form compatible with hybrid optimal control theory. Third and more critically, the fact that the controls take values in a convex compact set Ω makes the PMCP amenable to hybrid optimal technique. Fourth, any optimization algorithm searches for the optimal controls and switching function $v(t)$ in a hypercube as opposed to a (non-convex) state and time-dependent region.

5.3.1 State Equation for the ICE

The variable P_{ICE} denotes the unidirectional instantaneous ICE power flow, quantified at the flywheel and including losses due to parasitic loads. The ICE dynamical equation is given by equation (5.5), i.e.,

$$\dot{P}_{ICE} = -\frac{1}{\tau_{ICE}} P_{ICE} + \frac{1}{\tau_{ICE}} P_{\text{ICE}}^{\max}\left(\omega_{ICE}\right) \cdot eng\left(\omega_{ICE}\right) \cdot u_{ICE}(t) \tag{5.5}$$

where τ_{ICE} is the nominal engine power delivery delay averaging the effect of the firing delay, smoke limit map, crankshaft speed, fueling shot mode, etc. Further, this also ensures that the command handed down by the supervisory controller can be followed. $P_{ICE}^{\max}$ is an ω_{ICE}-dependent maximum available ICE power; ω_{ICE} is the CVT controller-selected engine speed using the strategy modified slightly from the speed-envelope for a non-hybrid ICE in [52]. Specifically,

$$\omega_{ICE} = \left(1-p\right)\omega_{\text{ICE}}^{\min}(V) + p\omega_{\text{ICE}}^{\max}(V) \tag{5.6}$$

where $p \in [0,1]$ modulates the speed curve according to the ICE power level; $\omega_{ICE}^{\min}(V)$ and $\omega_{ICE}^{\max}(V)$ are the minimum and the maximum allowable speeds at each vehicle's velocity and illustrated in Fig. 6. For better driveability, ICE-CVT's transition from non-engaged to engaged is not allowed when the vehicle's velocity is too low for jerk reduction. Note that in this study, the capitalized superscript indicates constant whereas lower-case superscripted means parameter dependent.

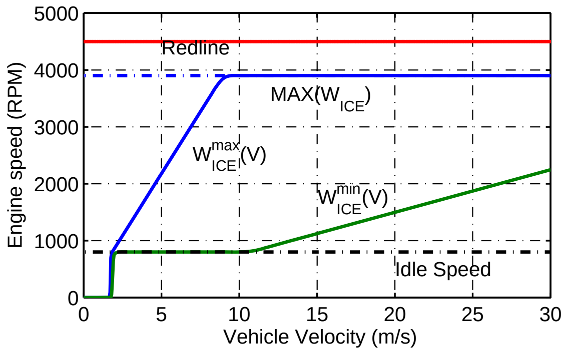

Fig. 6 Maps of minimum and maximum engine speeds for each vehicle's velocity

According to ICE dynamical equation (5.5), and the constraints on the input, (5.4), it can be shown that P_{ICE} belongs in compact and convex set shown below.

$$P_{ICE} \in [P_{ICE}^{MIN}, P_{ICE}^{MAX}] \subset \mathbb{R} \tag{5.7}$$

The range of ICE power (5.7) is not an additional state constraint, but rather is a direct result from the aforementioned relationships. This information is useful during the computation for the solution as the numerical search-space is smaller.

5.3.2 State Equation for Battery Operation

For a relatively new battery, its normalized energy and the SOC are equivalence [28, 53]. The state equation describing the SOC dynamics is derived based on the conservation of power and energy. The parameters are computed to fit the battery data. The *partial* linearization about the mode-dependent nominal battery operating power, $P_{bat,nom}^{v}$, describing the SOC is given by:

$$\dot{SOC}(t) = \frac{d_{3,v}}{W_{bat}^{MAX}}\left(P_{bat,nom}^{v}\right)^2 - \left[\ln\left(d_{1,v}SOC(t)+d_{2,v}\right)+2d_{3,v}P_{bat,nom}^{v}+d_{4,v}\right]\frac{P_{bat}}{W_{bat}^{MAX}} \tag{5.8}$$

In equation (5.8), W_{bat}^{MAX} is the rated maximum battery energy, P_{bat} is the battery power either drawn by (positive for $v=0$) or provided by the ED (negative for $v=1$) and is implicitly controlled by $u_{EM/GEN}$. Specifically,

$$P_{bat} = \begin{cases} P_{ED,in}^{0}, & v=0 \\ -P_{ED,out}^{1}, & v=1 \end{cases} \tag{5.9}$$

$d_{k,v}$, $k=1,...,4$ are the appropriate coefficients. The consideration of the recovery, cycling, and aging effects are beyond the scope of this investigation. This formulation makes equation (5.8) scalable to a variety of battery storage capacities and types.

5.3.3 State Equation for Vehicle Motion

The conventional longitudinal vehicle's velocity, is described, not in terms of torques, but rather in the acting power flow as:

$$\dot{V} = -\left[\frac{k_{v1}}{m_c}V^2 + k_{v2}\cos\left(\alpha(t)\right)\right]sgn\left(V\right) - g\sin\left(\alpha(t)\right) + \frac{1000}{m_c\left(V+\varepsilon_V\right)}\left[P_{CDD,wh}^{v} - P_{FR}\right] \tag{5.10}$$

In equation (5.10), ε_V is a regularization term; m_c is vehicle mass; ${k_{v1}}/{m_c}\,V^2$ is normalized aerodynamic drag; $k_{v2}\cos(\alpha(t))$ is the rolling resistance; $\alpha(t)$ is the time-varying angle of road inclination; $P_{CDD,wh}^{v}$ is the power delivered from (≥ 0) and to (<0) the CDD; Finally,

$$P_{FR} = P_{FR}^{\max}(V)u_{FR}(t) \tag{5.11}$$

is the frictional braking power.

As a result from equation (5.10), the vehicle's velocity is also in an invariant set,

$$V \in \left[V^{MIN}, V^{MAX}\right] \subset \mathbb{R} \tag{5.12}$$

5.3.4 Mode Dependent ED Modeling Equations

The derivation of the ED algebraic input-output power flow equations for both modes can be found in [54]. The ED in this study, operated under a maximum torque/amp (MTA) control strategy, can be represented at the supervisory level as

$$P_{ED}^{v} = \eta_{ED}^{v}(\omega_{ED})P_{ED,in}^{v} \tag{5.13}$$

Each term in equation (5.13) is mode dependent. The ED output power is denoted P_{ED}^{v}, the efficiency $\eta_{ED}^{v}(\omega_{ED})$ strongly depends on the choice of closed-loop control, a phenomena largely underweighted in HEV literature. $\omega_{ED} = \beta \cdot V$ is the ED rotor speed; β is a positive constant.

The ED input power in modes 0, and1 are

$$P_{ED,in}^{0} = P_{ED,in}^{max}\left(\omega_{ED}\right) \cdot u_{EM}(t) \tag{5.14}$$

$$P_{ED,in}^{1} = P_{ED,in}^{max}\left(\omega_{ED}\right) \cdot u_{GEN}(t) \tag{5.15}$$

where $P_{ED,in}^{max}\left(\omega_{ED}\right)$ is the speed dependent ED maximum input power modulated by the control $u_{EM}(t)$ in mode-0, and $u_{GEN}(t)$ in mode-1.

5.3.5 CVT and mode-dependent CDD Power Flow Equations

No power response lag between the input and output CVT powers is assumed at the supervisory level, leading to the algebraic equation

$$P_{cvt,out}(t) = \eta_{cvt} P_{cvt,in} \tag{5.16}$$

where η_{cvt} is the CVT efficiency; $P_{cvt,in}(t) = P_{ICE}$ is the CVT input power; and the output power is delivered to the CDD, i.e., $P_{cvt,out}(t) = P_{CDD,cvt}$.

The CDD's input/output power flows are given by

$$P_{CDD,wh}^{0}(t) = \eta_{cdd1} P_{CDD,cvt} + \eta_{cdd2} P_{CDD,ED}^{0} \tag{5.17}$$

and

$$P_{CDD,ED}^{1}(t) = \eta_{cdd2} P_{CDD,cvt} - \eta_{cdd2} P_{CDD,wh}^{1} \tag{5.18}$$

(i) η_{cdd1}, and η_{cdd2} are the appropriate power transfer efficiency among the ED, CVT and wheels; (ii) $P_{CDD,ED}^{0} = P_{ED}^{0}$ is the propulsion power coming directly from the output of the ED in mode-0; in mode-1 $P_{CDD,ED}^{1} = P_{ED,in}^{1}$ is an output power port of the CDD providing mechanical power to the input of the ED (generator); (iii) in mode-0, $P_{CDD,wh}^{0} \geq 0$. However, in mode-1, $P_{CDD,wh}^{1}(t)$ can be either positive or negative Note that $P_{CDD,wh}^{0}$ is represented as P_{load} in the mode reduction concept in section 2.2.

5.4 Performance Index

To incorporate the desired behaviors of the HEV operation, we consider the optimization functional for each mode, as follows:

$$\begin{aligned} J_v(x_0,u,[t_0,t_f]) &= g(t_0,x_0,t_f,x_f) \\ &+\int_{t_0}^{t_f} L_v(t,x,u)dt \end{aligned} \tag{6.1}$$

The mode-dependent integrand $L_v(t,x,u)$ depends on the optimization objectives, such as minimizing only fuel consumption as in [55], or a combination of fuel consumption and emissions as in [11, 56, 57]. In this research the PI consists of terms that are consistent with the power flow management framework and have meaningful physical interpretations. The integral quadratic PI that uses the same integrand for both modes of operation, i.e., $L_0(t,x,u)=L_1(t,x,u)$ is adopted in this study. The integrand for both modes is

$$L_v = C_V\left(V - V^{des}(t)\right)^2 + C_{ICE}\left(\frac{P_{ICE}}{\eta_{ICE}(\bullet)}\right)^2 + C_{FR}\left(P_{FR}\right)^2 \tag{6.2}$$

The integrand penalize the velocity tracking error, $C_V\left(V - V^{des}(t)\right)^2$, the frictional braking power, $C_{FR}\left(P_{FR}\right)^2$, and the fuel usage. The fuel usage is approximated by ICE power usage divided by fuel conversion efficiency [[58]], i.e.,

$C_{ICE}\left(\frac{P_{ICE}}{\eta_{ICE}(\bullet)}\right)^2 = C_{ICE}(P_{fuel})^2$ where $\eta_{ICE}\left(P_{ICE},V\right)$ is the ICE efficiency that depends on the ICE power-and-speed. Fig. 7 depicts the efficiency map of the ICE superimposed with the iso-efficiency curves.

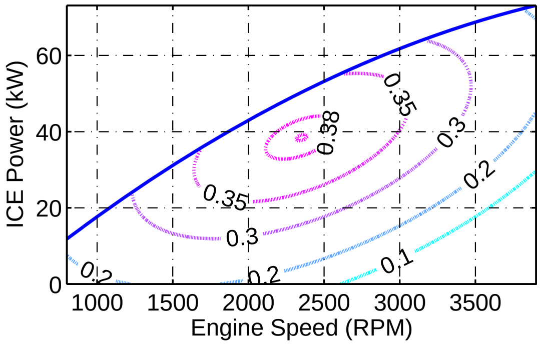

Fig. 7 ICE power-vs.-engine speed superimposed with iso-efficiency curves.

The penalty on the variation in the boundary conditions, $g(t_0, x_0, t_f, x_f)$, in PI (6.1) is taken as $C_{bat}(\bullet)\left(SOC(t_f) - SOC^{NOM}\right)^2$. This choice of the penalty pushes the SOC at t_f toward the nominal level, SOC^{NOM}. It is also desirable to operate the SOC in a predefined range to prolong battery lifetime. It will be shown in the simulation results that this choice of penalty on the battery SOC can be used to encourage

$$SOC \in \left[SOC^{MIN}, SOC^{MAX}\right] \subset \mathbb{R} \tag{6.3}$$

Note that if the constraints (6.3) are violated, the penalty term on the SOC must be more stringent. This SOC strategy is to enforce the charge-sustaining operation.

A more elaborate PI accounting for drivetrain losses in each mode has the form

$$\begin{aligned} L_v = {} & C_V^v\left(V - V^{des}\right) + C_{ICE}^v\left(P_{fuel}\right)^2 + C_{cvt}^v\left(P_{cvt,loss}\right)^2 \\ & + C_{CDD}^v\left(P_{C,loss}^v\right)^2 + C_{ED}^v\left(P_{ED,loss}^v\right)^2 \\ & + C_{bat}^v\left(P_{bat,loss}^v\right)^2 + C_{FR}^v\left(P_{FR}\right)^2 \end{aligned} \tag{6.4}$$

where the additional power loss terms are CVT losses, CDD loses, ED losses, and battery losses, whose identity should be clear from the notation. More details on the generalized PI can be found in [45].

5.5 Power Management Control Problem and the EOCP

For the switched optimal control problem (SOCP), the modal switching function $v(t)$ belongs to a discrete set $\{0,1\}$, $v(t) \in \{0,1\}$. In contrast, for the EOCP the modal switching function $v(t)$ takes values in the closed interval $[0,1]$, a continuum of possible values. The enlargement of $v(t) \in \{0,1\}$ to $v(t) \in [0,1]$ constitutes an embedding of the SOCP into a larger family of continuously parameterized problems. This embedding converts a non-convex SOCP into a convex EOCP. As per [19] the SOCP can almost always be solved by first solving the EOCP and any solution of the EOCP can be approximated to any degree of precision by some solution of the switched state model (5.2). Further, in this study, projection techniques are also presented as alternatives for approximating the EOCP with the SOCP.

5.5.1 Specification of the embedded optimal control problem

The embedding requires creating a convex combination of the vector fields of the switched state model according to the equation,

$$\begin{aligned}\dot{x}(t) &\triangleq f_E\left(x(t),u_0(t),u_1(t),v(t)\right)\\ &=\left[1-v(t)\right] f_0\left(x(t),u_0(t)\right)+v(t)\,f_1\left(x(t),u_1(t)\right)\end{aligned} \tag{7.1}$$

where $u_i(t)\in\Omega$, $i=0,1$. Clearly if $v(t)=0$, f_E reduces to the 0-mode vector field and similarly for $v(t)=1$.

The performance index (PI) of the EOCP results from a similar convex embedding of the PIs associated with each mode of operation of the SOCP:

$$\begin{aligned}J_E(x_0,u_0,u_1,v,[t_0,t_f]) &= g(t_0,x_0,t_f,x_f)\\ &\quad+\int_{t_0}^{t_f} L_E(t,x,u_0,u_1,v)dt\end{aligned} \tag{7.2}$$

$$\begin{aligned}&= g(t_0,x_0,t_f,x_f)\\ &\quad+\int_{t_0}^{t_f}\left[\left(1-v(t)\right)L_0(t,x,u_0)+v(t)L_1(t,x,u_1)\right]dt\end{aligned}$$

with $L_i(t,x,u_i)$, $i=0,1$ denoting the convex-in-u_i integrands of the PI. When $v(t)\in\{0,1\}$, the minimization of equation (7.2) subject to (7.1) defines the SOCP, while when $v(t)\in[0,1]$, the minimization of equation (7.2) subject to (7.1) constitutes the EOCP. Formally the EOCP (the structure for solving the PMCP) becomes:

$$\min_{u_0,u_1,v}\; J_E(x_0,u_0,u_1,v,[t_0,t_f]) \tag{7.3}$$

with $J_E(\cdot)$ given by equation (7.2), subject to

$$\dot{x}(t)= f_E(x(t),u_0(t),u_1(t),v(t)) \tag{7.4}$$

with f_E given in equation (7.1), $v(t)\in[0,1]$, and u_0, $u_1\in\Omega$.

5.5.2 Relationships between EOCP and SOCP

If the EOCP has a bang-bang type solution (wherein $v(t)$ only takes values in $\{0,1\}$) then clearly it is also a solution to the original SOCP. Further it can be shown (Corollary 2 in [19]) that the set of trajectories of the switched system (equation (7.1) with $v(t)\in\{0,1\}$) is dense in the set of trajectories of the embedded system (equation (7.1) with $v(t)\in[0,1]$). Thus when/if the EOCP does not have a bang-bang type solution (wherein $v(t) \in (0,1)$ for some non-zero measure sets of time) then the EOCP solution can be approximated by a trajectory of the switched system to any desired degree of precision. These relationships between the SOCP and EOCP motivate and justify the effort in determining SOCP solutions by solving the EOCP. Additional relationships between SOCP and EOCP can be found in [19].

5.5.3 Approximation to Singularities in EOCP

This subsection describes approximation techniques when the control $v(t)$ obtained via the EOCP is not bang-bang. When, $v(t) \in (0,1)$, i.e., $v(t)$ takes on fractional values, over an interval $t_1 \le t \le t_2$, it would suggest that for the HEV the ED operate simultaneously in both modes for this time interval, an impossibility. In another words, when $v(t) \in (0,1)$, the SOCP does not have a solution, but epsilon-approximating solutions can be constructed as follows. Given a desired error of approximation, ε, one can construct subintervals $t_1 < T_1 < T_2 .... < t_2$ such that $|T_{i+1} - T_i| < \delta$, where delta is generated based on ε, vector fields, f_i, and cost integrand, L_i. In the case when the switching interval--constrained by the embedded controller loop time, actuator bandwidth, etc--is larger than δ, one would have to increase the approximating error, ε, and re-construct the intervals. The approximating error will need to be sufficiently large to accommodate the constraint $\delta > T_{\min}$, where $T_{\min}$ is the minimum switching period.

The construction of the switching subintervals in the case of complex vector fields, such as the case for the HEV model, can be alleviated by considering empirical based switching intervals such as described below.

One approach to empirical switching is to average the fractional values of $v(t)$ over $t_1 \le t \le t_2$ and the average value, denoted $\bar{v}$, over $t_1 \le t \le t_2$, can be interpreted as a a duty cycle, or a pulse width modulation (PWM) control. So there exists a time t' such that for $t_1 \le t < t'$, the system is in mode 0 and for $t' \le t < t_2$ the system is in mode 1 so that the average over the whole interval is $\bar{v} = \dfrac{t_2 - t'}{t_2 - t_1}$. Thus, a PWM or switched approximation to the embedded $v(t)$ is made.

The previously computed $u_i(t)$ are associated with the embedded solution $v(t)$, not the new approximation. One possibility is to simply use these values for each associated subinterval. A second possibility is to set $v(t)$ equal to its PWM approximation and then find the optimal u_0 and u_1 associated with this choice. Switching can be minimized by beginning the duty cycle for the next interval in the ending mode of the prior interval.

A third possibility is as follows: let $T_{\min}$ be the smallest switching interval of time. For each time unit, $t_1 \le t \le t_2 = t_1 + T_{\min}$, one can project the fractional value of $v(t)$ onto the set $\{0,1\}$ according to the formula:

$$\left\| \overline{(1 - v(t)) \cdot u_0(t)} \right\|_2 \begin{cases} \ge \left\| \overline{v(t) \cdot u_1(t)} \right\|_2 & \rightarrow \quad v(t) = 0 \\ < \left\| \overline{v(t) \cdot u_1(t)} \right\|_2 & \rightarrow \quad v(t) = 1 \end{cases} \tag{7.5}$$

where over-bars denote averages over the interval $t_1 \le t \le t_2 = t_1 + T_{\min}$. As before one can either use the previously calculated values of u_i or resolve the optimization with $v(t)$ fixed at the desired mode. For the simulation studies of this work, equation was used to fix the bang-bang solution for $v(t)$ and then the optimization was resolved for the best pair of $u_i(t)$ given the fixed mode sequence.

5.5.4 Embedded PI for PMCP

As mentioned earlier, the integrand and the penalty on the boundary conditions in both modes are the same. The embedded PI for the PMCP is obtained by substituting appropriate terms in the PI (7.2), i.e.,

$$\begin{aligned} J_E = {} & C_{bat}(\bullet)\left(SOC(t_f) - SOC^{NOM}\right)^2 + \int_{t_o}^{t_f} \left(C_V \left(V - V^{des}(t)\right)^2 + C_{ICE} \left(\frac{P_{ICE}}{\eta_{ICE}(\bullet)} \right)^2 \right. \\ & \left. + C_{FR} \left(P_{FR}^{MAX}(\bullet) u_{FR}(t) \right)^2 \right) dt \end{aligned} \tag{7.6}$$

where the physical meaning of each term is given in a previous section.

5.6 Summary on Theoretical Foundations

When the discrete input $v \in \{0,1\}$ presents, it renders, in general, the SOCP non-convex. For a variety of assumptions on system vector fields f_v, an SOCP performance index, and mode-switching penalties and constraints, several approaches have been employed in the literature for characterizing and computing SOCP solutions, consisting of: searches over or assumptions on mode sequences and switching instants, after which one computes the continuous control values and the cost to compare the different scenarios. These approaches do not allow the switching function to be chosen in concert with the continuous time control as is the case with the embedded approach.

Other Approaches include pre-assigned switching sequence method (for a limited class of problems) in [59], and a hybrid Bellman inequality approach in [60]. Mixed integer programming (MIP) approaches have also been employed to find optimal solutions [18]. Solving the problem using MIP methods, however, is non-deterministic polynomial-time hard (NP-hard); indeed the scalability of this technique is problematic [61].

The nonconvexity of the problem and the inapplicability of the mentioned existing techniques—too general and impractical, or very specific results, or insufficient characterization of the solution— to the SOCP has led to the development of the parameterized family of problems, the EOCP, set forth in the previous section.

5.6.1 EOCP: Sufficient Existence Conditions

This section summarizes the main sufficient conditions for EOCP solutions. Sufficient conditions for optimality are [Theorem 9, in [19]]:

(i) the admissible pair set (control, trajectory) is nonempty;

(ii) the points $(t, x(t))$ are included in a compact set for all $t \in [t_0, t_f]$;

(iii) the terminal set is compact;

(iv) the input constraint set is compact and convex;

(v) the vector fields f_0 and f_1 are linear in their (control) inputs u_0, and u_1, respectively i.e.,

(S1) $f_0(t, x, u_0) = A_0(t, x) + B_0(t, x)u_0$

(S2) $f_1(t, x, u_1) = A_1(t, x) + B_1(t, x)u_1$

(vi) for each $(t, x(t))$, the integrands of the penalty functions, $L_0(t, x, u_0)$ and $L_1(t, x, u_1)$, are convex functions of u_0, and u_1, respectively.

Based on the assumptions made on the input constraint set and on the vector fields f_0 and f_1, one can conclude that conditions (i), (ii), and (iv) are met. Further, a sufficiently large compact set can be substituted for the terminal set, meeting condition (iii). Condition (v) is also met as it can be observed based on the modeling equations from Sections 2. The power terms that depend on the continuous control inputs, and they can be factored into the product of a control input and a term that depends on the state, $x(t)$. Utilizing the form of these power terms, and the forms of $L_0(t,x,u_0)$ and $L_1(t,x,u_1)$ one concludes that condition (vi) is also met. Hence the EOCP has a solution.

The above sufficient conditions only guarantee the existence of the EOCP's solutions, but do not provide a solution methodology. In conjunction with the SOCP-EOCP relationships mentioned above, the necessary conditions obtained by direct application of the Maximum Principle [24] provide a method for obtaining at least suboptimal solutions of the SOCP. By using this approach, the optimization problem is transformed into a two-point boundary value problem on the state and adjoint equations. The single shooting method is applied to compute the numerical solution in [24], and the solution is very sensitive with respect to the co-state initial condition. The multiple shooting method can be applied to reduce the sensitivity issue. This paper takes an alternate approach for computing numerical solutions to the EOCP, i.e., via the direct collocation method, described in the next section.

5.7 Numerical Technique and NMPC

This section briefly describes the direct collocation method and the nonlinear model predictive control (NMPC) strategy. Both are used in conjunction to formulate the PMCP as a nonlinear programming problem (NLP).

5.7.1 Discretization via Direct Collocation

Given the PI (7.6) and the state equation and constraints of equations (7.1), one discretizes these equations using the direct collocation method. The discretization of the PI uses a variation of the trapezoidal rule and constraint equations use the mid-point rule, respectively. These discretized equations convert the EOCP into a finite dimensional NLP where states and inputs are treated as unknown variables. The direct collocation technique consists of several steps that have two main stages: (i) time discretization, and state and input function approximations by a finite number of polynomial basis functions; (ii) approximation of the continuous state dynamics and cost index integrand by discrete-state and discrete-input-dependent counterparts.

Without going through a lengthy derivation, the continuous time interval $[t_0, t_f]$ is discretized into a sequence of points $t_0 < t_1 < t_2 < \cdots < t_{N-1} < t_N = t_f$ where, for simplicity, we take $t_j - t_{j-1} = h$, for $j = 1,\ldots, N$. A "hat" notation is also used to distinguish the numerically estimated state and control values from their actual counterparts that are "hatless", e.g., $\hat{x}_j = \hat{x}(t_j)$, $\hat{u}_{0,j} = \hat{u}_0(t_j)$, $\hat{u}_{1,j} = \hat{u}_1(t_j)$ and $\hat{v}_j = \hat{v}(t_j)$. The collocation method used here assumes triangular basis functions for the state and piecewise constant basis functions (derivatives of triangular functions) for the controls. Specifically, the estimated state is given by

$$\hat{x}(t) = \sum_{j=0}^{N} \hat{x}_j \varphi_j(t) \tag{9.1}$$

where the $\hat{x}_j$'s are to be determined and the triangular basis functions are given by

$$\varphi_j(t) = \begin{cases} \dfrac{t - t_{j-1}}{h}, & t_{j-1} < t \le t_j \\ \dfrac{t_{j+1} - t}{h}, & t_j < t \le t_{j+1} \\ 0, & \text{elsewhere} \end{cases} \tag{9.2}$$

We note two points: the method is not restricted to using triangular basis functions and each of the $\varphi_j(t)$'s is a time shift of the previous one.

As summarized in [20], the theoretical approach for computing the controls is to extend the state space with new state variables, $x_{ext} \in R^{m+1}$, whose derivative are the desired controls, $u(t) \in R^m$ and $v(t) \in [0,1] \subset R$, to be computed. However, our choice of triangular basis functions for the states renders the control inputs piecewise constant and we simply solve directly for these (constant) control values. Specifically, the estimates of the control inputs are given by

$$\begin{bmatrix} \hat{u}(t) \\ \hat{v}(t) \end{bmatrix} = \sum_{j=1}^{N} \begin{bmatrix} \hat{u}_j \\ \hat{v}_j \end{bmatrix} \psi_j(t) \tag{9.3}$$

where the piecewise constant basis functions are given by

$$\psi_j(t) = \begin{cases} 1 & t_{j-1} < t \le t_j \\ 0 & \text{elsewhere} \end{cases} \tag{9.4}$$

The essence of the midpoint rule in the collocation method is to enforce the constraints at the midpoints of each interval $[t_{j-1}, t_j]$ for $j = 1, ..., N$. There results the discretized embedded state dynamics

$$\begin{aligned} \hat{x}_j = \hat{x}_{j-1} + h \cdot (1 - \hat{v}_j) \cdot f_0\left(\frac{\hat{x}_{j-1} + \hat{x}_j}{2}, \hat{u}_{0j} \right) \\ + h \cdot \hat{v}_j \cdot f_1\left(\frac{\hat{x}_{j-1} + \hat{x}_j}{2}, \hat{u}_{1j} \right) \end{aligned} \tag{9.5}$$

for $j = 1, ..., N$, with $f_0(\cdot)$ and $f_1(\cdot)$ the discretized state dynamics in modes -0 and -1, respectively. Thus, the solution to the EOCP is given by the following NLP: Minimize

$$\begin{aligned} \hat{J}_E = C_{bat}(\bullet)\left(\overset{\wedge}{SOC}_N - SOC^{NOM} \right)^2 \\ + \sum_{j=1}^{N} \frac{1}{2} h \Big\{ L_E\left(t_j, \hat{x}_j, \hat{u}_{0j}, \hat{u}_{1j}, \hat{v}_j, \hat{p}_j \right) \\ + L_E\left(t_{j-1}, \hat{x}_{j-1}, \hat{u}_{0j}, \hat{u}_{1j}, \hat{v}_j, \hat{p}_j \right) \Big\} \end{aligned} \tag{9.6}$$

over the controls $(\hat{u}_j, \hat{v}_j) \in \Omega \times [0,1]$, subject to equation (9.6) and all other equality/power-flow constraints represented as $g(\hat{x}_{j-1}, \hat{x}_j, \hat{u}_j, \hat{v}_j, \hat{p}_j) = 0$. Here $L_E(\cdot)$ is the integrand of equation properly discretized and $\widehat{p}_j$ represents the various power flows in the model.

5.7.2 Nonlinear Model Predictive Control

The NMPC solution strategy in this study uses a moving four-second predictive-window with the control applied over one-second sub-interval. In particular the NLP for $t = t_j$ is solved over $[t_j, t_{j+1}, t_{j+2,} t_{j+3}, t_{j+4}]$ instead of the entire driving cycle. The resulting control at each iteration is applied only over $[t_j, t_{j+1}]$ to the system model. Using the constant controls computed by NMPC algorithm, the system model is then simulated over $[t_j, t_{j+1}]$ to obtain an updated state at t_{j+1}. This updated state represents what would be measured in a real-world implementation of the NMPC control [27, 62].

$t_{f,j}$ denotes the final time of each NMPC iteration, and hence is the final time in the PI (7.6). Further for the NMPC strategy the coefficient penalizing the deviation from nominal SOC, $C_{bat}(t_{f,j})$ is linearly interpolated according to the equation

$$C_{bat}(t_{f,j}) = (t_{f,j}/t_f)C_{bat}^{nom} \tag{9.7}$$

Otherwise, the NMPC control will try to maintain the SOC at SOC^{NOM} over each iteration unduly restricting the use of battery power.

Difficulties arise for real world implementation since this strategy presumes knowledge of t_f. Nevertheless, it can be entered by drivers, or becomes an adaptive function of the recent history of the vehicle's power consumption. The estimation problem of t_f is beyond the scope of this paper.

In the beginning of each NMPC window, we assume the knowledge of the current road grade (e.g., through an accelerometer or future GPS). The control algorithms assume that over each partition of the NMPC window, the road grade is constant at the value at the beginning of the NMPC window. Although the road grade may change over the NMPC window, since the control is only applied over the first partition, after which a new measurement is taken, potential error is believed negligible.

5.8. Simulation Results

The NLP of the PMCP is applicable to various numerical solvers such as AIMMS, TOMLAB, etc. In this study, a sequential quadratic programming (SQP) based NLP solver, *fmincon*, is adopted. This section details simulation results for PHEV tracking different driving profiles. The first set of simulations compare the overall hybrid optimal control and the NMPC tracking the sawtooth driving profile with road grades. The next simulation details the PHEV tracking the standard 765 s EPA Highway driving profile to which is added a sinusoidal road grade to better exercise the controller performance. The second simulation looks at the 600 s US06 FTP supplemental driving schedule. The numerical solutions to various driving profiles are shown below.

5.8.1 Optimal and NMPC Tracking of Sawtooth Velocity Profile with Road Grades: Cases 1 and 2

The performances of the overall hybrid optimal control and the NMPC strategies are compared using the sawtooth driving profile suggested in [50]. The sawtooth profile demands higher rates of acceleration/deceleration than typical driving cycles.

To further test the limits of performance of the vehicle powertrain, positive sinusoidal road grades are superimposed in this paper.

The coefficients of the PI (7.6) are $C_V = 10$, $C_{ICE} = 10^{-3}$, $C_{FR} = 10^{-4}$, and $C_{bat}(\bullet) = C_{bat}^{nom} = 10^5$. This study compares the performances of two hybrid optimal control strategies. Case 1 uses a control that minimizes the PI of equation (7.6) with the above coefficients over the entire driving cycle and is thus optimal over the driving cycle. Case 2 constructs an NMPC version that can be compared to the optimal solution.

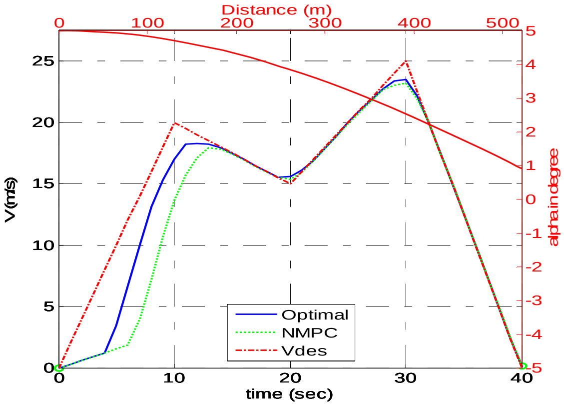

Fig. 8 Velocity tracking performance for overall optimal hybrid control and NMPC tracking sawtooth profile with road grades

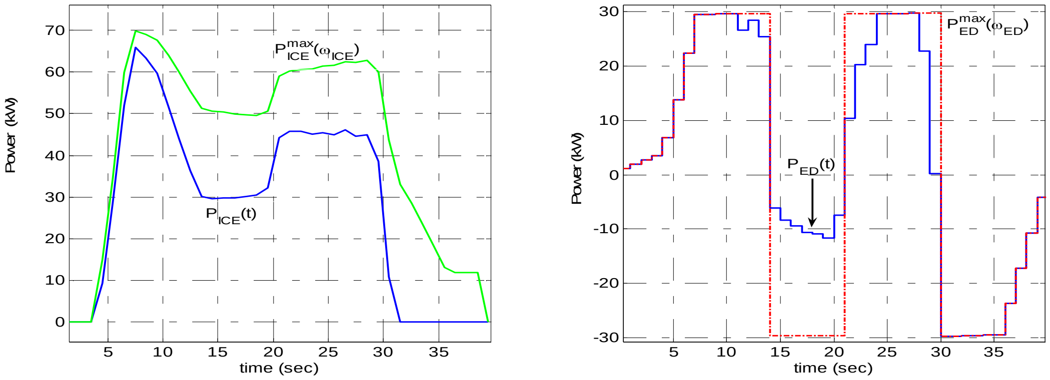

(a) (b)

Fig. 9 Output power for tracking sawtooth profile with road grades in case 1 showing (a) ICE power; and (b) ED power

Fig. 8 shows that initially the vehicle in both cases fail to provide perfect tracking. Initial tracking error is due to the insufficient available propelling power from the ICE and ED both of which already operate at their maximum levels, as shown in Fig. 9 for case 1. As per Fig. 9 (a), the ICE is off at startup (propelling from ED alone) due to the closed-loop local control constraint, until a minimum operating speed of 800 RPM is reached. Further, the tracking error during the first 14 s for the NMPC version is larger due to the fact that the NMPC decides to turn the ICE on slightly later. The rest of the driving profiles except the peak at 30 s can be tracked relatively well in both cases. After 30 s, when the desired velocity is decreasing and the road grades are positive but small; the ICE is turned off (Fig. 9 (a)) and the ED provides negative power to charge the battery in both cases as shown in Fig. 9 (b). Between 14 and 21 s the ICE in case 1 provides power both to charge the battery and to the wheels, while in case 2, the ICE only provides propelling power. The ICE profiles in this specific region for the NMPC are lower and circled in Fig. 10 (a). This contributes to slightly better fuel economy for the NMPC version of 14.7 MPG vs. 14.2 MPG for case 1.

Simultaneously, the ED in case 1 operates as a generator (mode-1) more often, specifically between 14 and 21 s, as depicted in Fig. 9 (b) and Fig. 10 (b). The NMPC hands down non-generating decision in this time interval because of a relatively lower penalty (coefficient) on the deviation from nominal SOC according to equation (9.7).

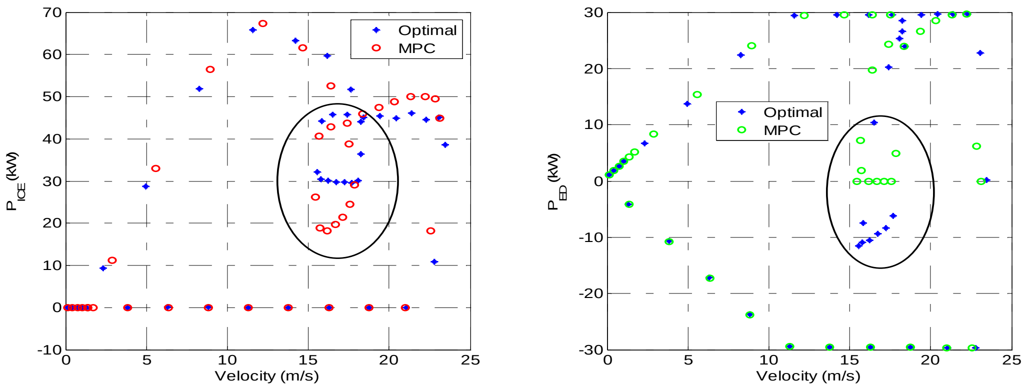

(a) (b)

Fig. 10 Output profiles vs vehicle's velocity for overall optimal hybrid control and NMPC tracking sawtooth with road grades showing (a) ICE power; (b) ED power

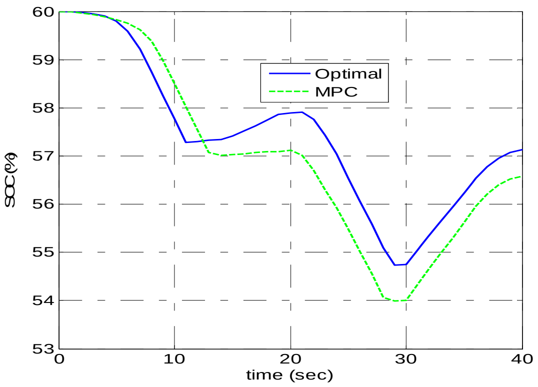

Fig. 11 Battery SOC for overall optimal hybrid control and NMPC tracking sawtooth with road grades

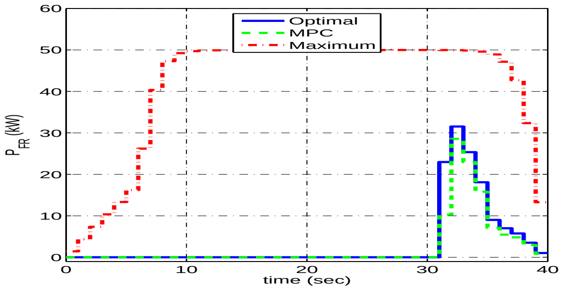

Fig. 12 Frictional-braking power for overall optimal hybrid control and NMPC tracking sawtooth with road grades

Fig. 11 depicts the battery SOC profiles. Case 1 shows consistency with the mode of operation and returns to the vicinity of the 60% nominal level at the end of the cycle. In case 2, SOC deviation is only mildly penalized allowing lower levels than in case 1 during the first half cycle. In the second half of the driving cycle, with an increasing penalty on the deviation from nominal SOC, the NMPC tries to recharge the battery and returns SOC to the level slightly lower than in case 1.

During the last 10 s, the ED operates as a generator in both cases as expected to provide regenerative braking power. Further, the demanded power is more (negative) than the maximum level that the ED can deliver in both cases as shown in Fig. 9 (b). To achieve the desired velocity tracking, the extra kinetic energy is expended in frictional braking as shown in Fig. 12. Indeed, frictional braking is only used during the last 10 s of the driving profile as one would expect.

5.8.2 NMPC Tracking of EPA Highway Driving Cycle with Road Grade: Case 3

In this case study, the vehicle is to follow the EPA highway driving profile for 765 seconds on a nonzero road grades as shown in Fig. 13. Also shown (in red) in Fig. 13, is the road grades, which has a positive angle (uphill) over the first 382.5 s, and then has a negative angle (downhill) over the final 382.5 s The coefficients of the PI of equation (7.6) are the same as those used in the sawtooth driving profiles with a sliding penalty on the deviation of the SOC from nominal as $t \rightarrow t_f = 765$ s Fig. 13 shows that the NMPC strategy provides nearly perfect tracking for this case.

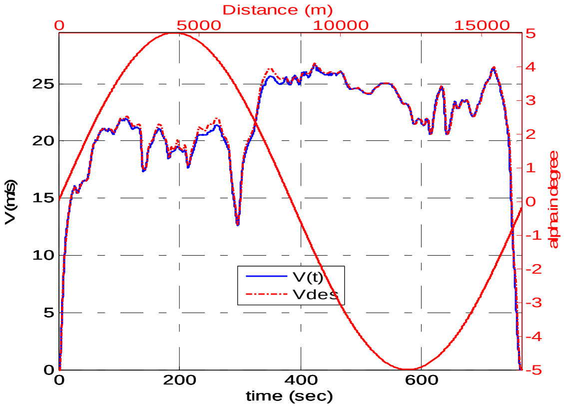

Fig. 13 Velocity tracking performances for case 3 on a road grades whose angle in degrees is indicated by the sinusoidal curve with values in degrees on the right vertical axis

Since there is very little penalty on battery usage initially (see equation (9.7)) and a relatively significant penalty on fuel consumption, mode 0 is active for 135 s (Fig. 14(a)) at which the desired velocity starts to decrease. Initially, the ED supplies roughly 20 kW of propelling power, and eventually decays to near zero at 135 s. In contrast, the ICE is initially off, and gradually ramps to supply propulsion demand reach 40 kW at roughly 135 s (Fig. 16). In other words, the NMPC strategy decides to drain the power from the ED-battery pack to as low as 45% during this time period as shown in Fig. 14(b).

After 60 seconds, the ICE power contribution continues to ramp and then remains relatively constant at about 45 kW until 400 seconds as per Fig. 16. Over this period, fuel efficiency is relatively high according to the ICE efficiency map in Fig. 7.

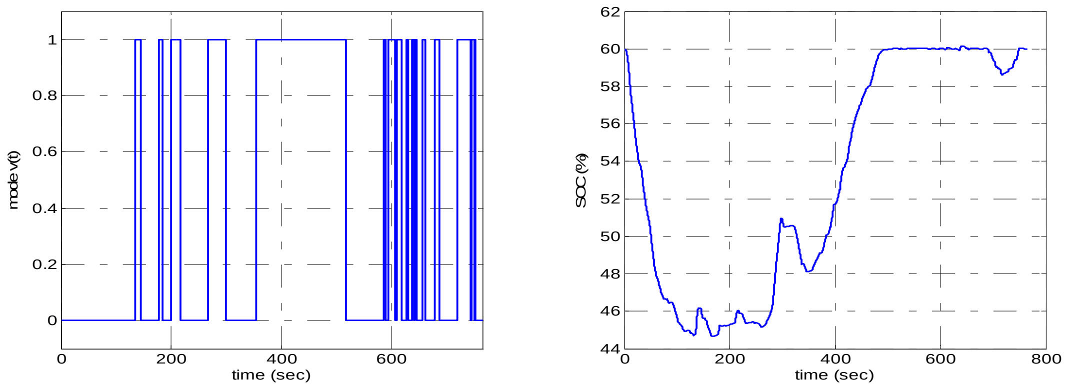

(a) (b)

Fig. 14 NMPC strategy for tracking EPA highway profile showing (a) Mode of operation; (b) Battery SOC Profiles.

Around 260 sec, the road profile becomes less demanding and the vehicle operates in the generating mode more often. Further, after 382.5 sec, the road grades are negative, which leads to regenerative braking. Fig. 15 shows that the ED operates more frequently in the generating mode for recharging the battery back to its nominal value of 0.6. Further, there is little need for propelling power to maintain perfect tracking, hence the ICE is off most of the time in the second half of the driving cycle.

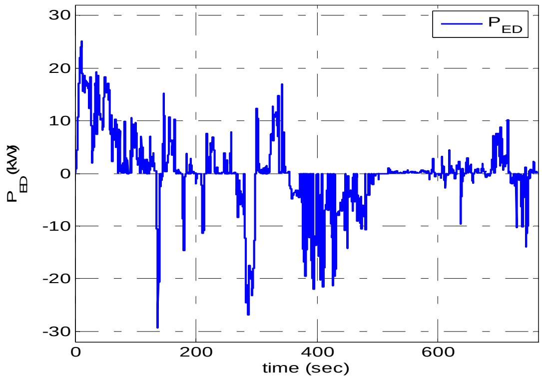

Fig. 15 ED output power profiles for PHEV tracking EPA highway using NMPC strategy

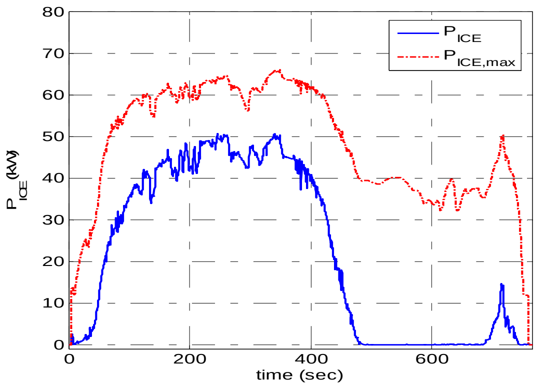

Fig. 16 ICE power usages for PHEV tracking EPA highway using NMPC strategy.

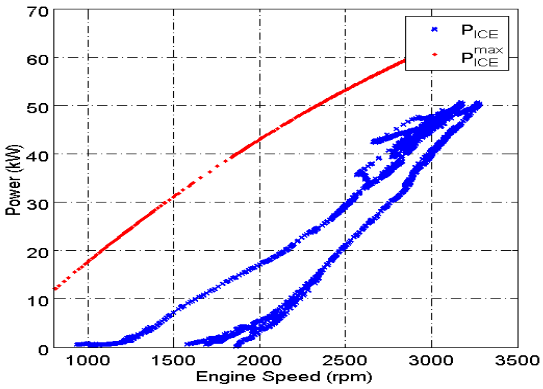

Fig. 17 Trajectories of ICE power vs. engine speed for PHEV tracking EPA highway using NMPC strategy showing acceleration/deceleration hysteresis

The map of the ICE power over the engine speeds' range shows denser data in the fuel efficient region. Hysteresis appears as the result of the dynamics (lag) in the engine power during the acceleration and deceleration as shown in Fig. 17. Fig. 18 shows the operation of the ED over the range of vehicle speeds.

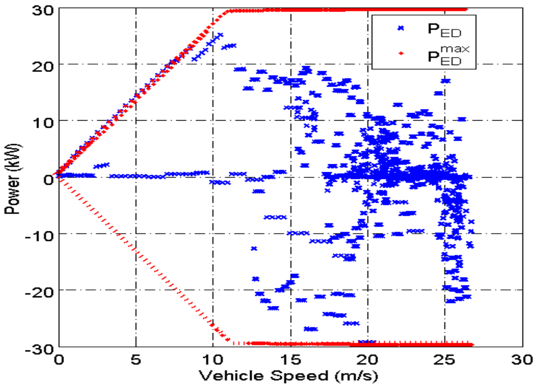

Fig. 18 Trajectories of ED power vs. vehicle for PHEV tracking EPA highway profile using NMPC

In the presence of the sinusoidal road grade over the cycle, the fuel economy is 27.5 mpg, lower than the 32 mpg (similar to current hybrid SUVs on the market) when the road is flat due to (i) frictional braking losses during the negative road grades to maintain velocity tracking and (ii) inefficiencies in energy recovery from regenerative braking. The simulation result in the case of vehicle tracking the EPA highway velocity profile on a flat road is not included in this paper due to space limitations, but it can be found in [45].

One concludes that the NMPC strategy performs very well while sustaining the constraint on the final SOC. Further, the resulting power distributions in this case study is used to justify the concept of five-to-two mode reduction as shown in Fig. 5. The 40 kW line is drawn in the figure to indicate a rough ICE power level that is fuel efficient for a medium engine-speed range.

5.8.3 MPC Tracking of the US06 supplemental FTP Driving Profile: Case 4

In this case study, we again use NMPC to track the 600 second US06 supplemental FTP driving schedule, which demands higher accelerations and more aggressive velocity variation/limits than the standard EPA city and highway schedules as shown in Fig. 19. The coefficients of the PI are the same as those in the previous cases. Fig. 19 again shows that the NMPC almost perfectly tracks the desired velocity profile.

The aggressive nature of the velocity profile forces the ED to operate close to maximum power levels in both modes (Fig. 20 (a)) while the power usage of the ICE mimics (Fig. 20 (b)) the shape of the velocity profile.

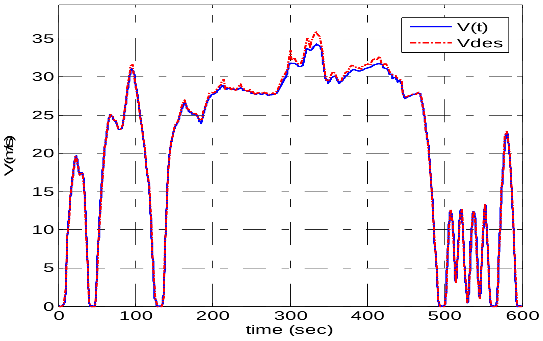

Fig. 19 US06 supplemental FTP driving profile and vehicle tracking performance

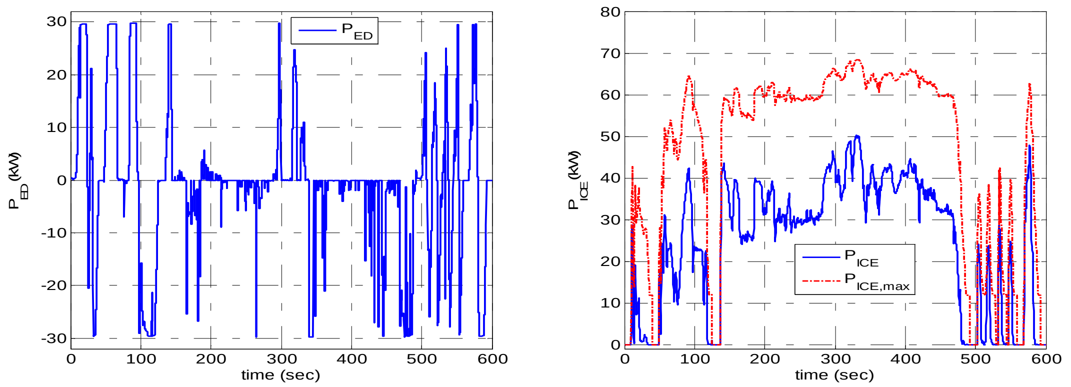

(a) (b)

Fig. 20 (a) ED output power and (b) ICE output power profiles in case 4

To meet the transient acceleration demands, NMPC puts the ED in the motoring mode during acceleration and in the generating mode during deceleration. During the non-transient power demand, the middle of the driving cycle, the ED is often off or provides relatively low power and the ICE provides most of the power as it can operate around its more fuel efficient level. Overall, estimated fuel efficiency averages at 23 mpg, a lower value than the EPA highway profile of 32 due to the more aggressive power demands of this case study. During the first 100 sec of the driving schedule, the HEV operates primarily in the motoring mode draining the battery to an SOC of about 45 percent as shown in Fig. 21(a). The aggressive acceleration driving profile in concert with the relatively low penalty on the SOC deviation from the nominal level contributes to the NMPC selection of this strategy. Afterward, as the penalty on the SOC deviation increases linearly toward the final time of 600 sec, the SOC rises toward the nominal level of 0.6 with more frequent time in mode 1.

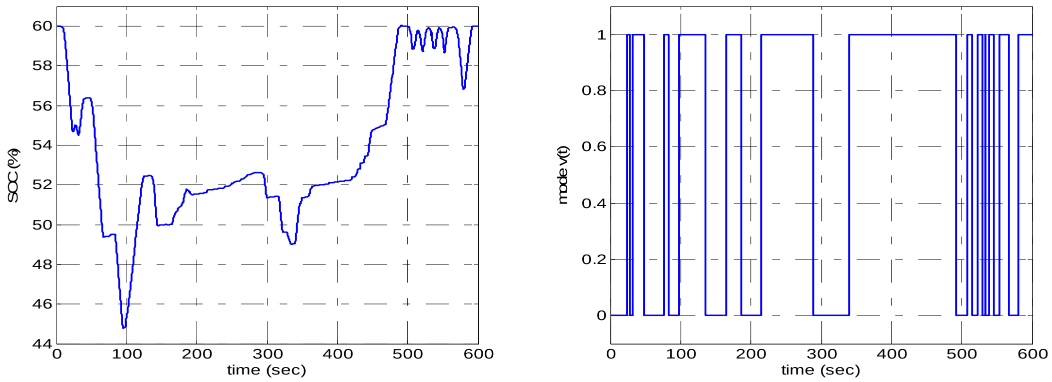

(a) (b)

Fig. 21 Case 4: (a) Battery SOC Profiles; (b) Mode of operation

Mode switching in both cases, using the strategy outlined in section 3.4, is reasonable, and consistent with the velocity variations in the driving profile as shown in Fig. 21(b).

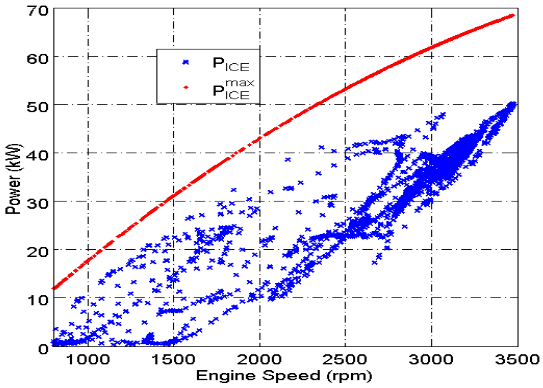

Fig. 22 Trajectories of ICE power vs. engine speed for PHEV tracking US06 FTP profile using NMPC strategy

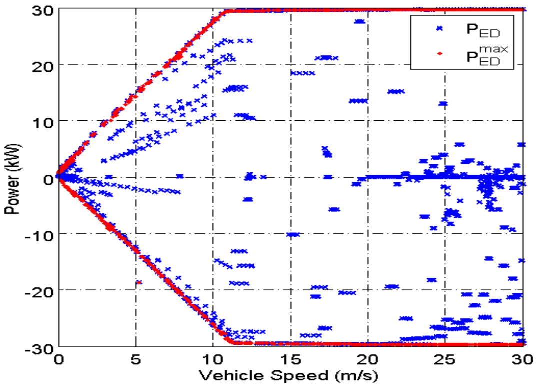

Fig. 23 Trajectories of ED power vs. vehicle for PHEV tracking US06 FTP profile using NMPC strategy

Similar to case 3, the nature of the modified speed envelope strategy for the CVT dictates higher engine speed for higher ICE power as depicted in Fig. 22. Dense engine data is located around 40 kW. In contrast to case 3, wider spread in the trajectories of the ICE on the power-vs-speed map can be observed in this case. Frequent operations on the ED maximum power-vs-speed envelope (in both motoring and generating) are also observed in this case, as depicted in Fig. 23. These characteristics in the ICE and the ED power profiles reflect greater variety of demands in the US06 FTP profile.

6. CONCLUSIONS AND FUTURE WORK

In this investigation, we have shown that the dynamic measurement of the battery state-of-charge was approximated by the partially linearized (control-oriented) battery model for both charging and discharging. A complete mathematical development of the partially linearized battery model was presented in Section II.B and in Appendix A. The model was augmented with an additional differential equation to capture the recovery effect. Then the versatility of the scalable partially linearized model to different battery types and its validation against the actual data for both charging and discharging was demonstrated. The model was found to be reasonably accurate around its nominal input power level for various battery types. The battery model with the incorporated recovery model was exhaustively exercised under a variety of power loads for Li-ion battery lifetime estimation. Actual lifetime measurements and the estimated lifetimes using Rakhmatov and Virudhula battery model were given for comparison. Although the developed model is linear in the input, it captures all the essential nonlinear characteristics of the battery under varying load conditions.

The partial linearized input-output battery model has been used successfully for control-oriented power flow management in an parallel HEV application Therein the application of the hybrid optimal control for solving the power management control problem (PMCP) of the vehicle has been illustrated.

The numerical solution is obtained by converting the original infinite dimensional problem into a finite dimensional nonlinear programming problem (NLP) using the direct collocation technique. Then, the resulting NLP is solved via a sequential quadratic programming algorithm. Requiring a short predictive window, the NMPC strategy is applied to solve the PMCP for the sawtooth, EPA highway, and US06 supplemental FTP driving profiles. The simulations show that the NMPC can track the driving profiles quite well unless there is insufficient available power to achieve the tracking as illustrated in case of the sawtooth profile with positive road grades. In practice, vehicle control strategies are often PID and maps/look-up tables based. The resulting NMPC profiles can help providing additional information on how to improve the existing look-up tables or tuning the gain-scheduling maps in the PID based controllers.

The obtained battery model is very useful for control when an inverter controls the current-voltage levels (and thus power levels) between the battery and any device such as an electric drive, sensor, or actuator. In distributed sensor network application estimation of battery longevity, estimates of scheduled maintenance and replacement are some of the key issues. The usage of the model is computationally inexpensive and can provide reasonably accurate information on the state-of-charge of the batteries. This information will assist in intelligent network activity scheduling, dynamic re-routing, and battery energy aware protocol designs in scenarios where battery maintenance and replacement is impractical.

The accuracy of the partially linearized battery model can be improved by selecting different nominal input powers based on the operating load power. For example, one can create a set of range of load powers and select an associated nominal input power for each range to lower the deviation between load power and nominal input power, and hence to reduce the approximation error. Finally, as a direction for future work, one can incorporate the effect of temperature variation into the partially linearized battery model making the model amenable to more practical applications.

7. REFERENCES

[1] O. Erdinc, B. Vural, and M. Uzunoglu, "A wavelet-fuzzy logic based energy management strategy for a fuel cell/battery/ultra-capacitor hybrid vehicular power system," *Journal of Power Sources,* vol. In Press, Corrected Proof, 2009.

[2] A. G. Pesaran, J.; Keyser, M., "Ultracapacitor Applications and Evaluation for Hybrid Electric Vehicles," in *Advanced Capacitors World Summit 2009*, La Jolla, California, 2009.

[3] J. B. Cao and B. G. Cao, "Neural network sliding mode control based on on-line identification for electric vehicle with ultracapacitor-battery hybrid power," *International Journal of Control, Automation and Systems,* vol. 7, pp. 409-418, 2009.

[4] F. Barbir, H. Gorgun, and X. Wang, "Relationship between pressure drop and cell resistance as a diagnostic tool for PEM fuel cells," *Journal of Power Sources,* vol. 141, pp. 96-101, 2005.

[5] T. E. Springer, T. A. Zawodzinski, and S. Gottesfeld, "Polymer electrolyte fuel cell model," *Journal of the Electrochemical Society,* vol. 138, pp. 2334-2342, 1991.

[6] Q. Shen, M. Hou, X. Yan, D. Liang, Z. Zang, L. Hao, Z. Shao, Z. Hou, P. Ming, and B. Yi, "The voltage characteristics of proton exchange membrane fuel cell (PEMFC) under steady and transient states," *Journal of Power Sources,* vol. 179, pp. 292-296, 2008.

[7] D. Feroldi, M. Serra, and J. Riera, "Energy Management Strategies based on efficiency map for Fuel Cell Hybrid Vehicles," *Journal of Power Sources,* vol. 190, pp. 387-401, 2009.

[8] G. Rizzoni, L. Guzzella, and B. M. Baumann, "Unified modeling of hybrid electric vehicle drivetrains," *IEEE/ASME Transactions on Mechatronics,* vol. 4, pp. 246-257, 1999.

[9] P. Pisu and G. Rizzoni, "A comparative study of supervisory control strategies for hybrid electric vehicles," *IEEE Transactions on Control Systems Technology,* vol. 15, pp. 506-518, 2007.

[10] G. Q. Ao, J. A. Qiang, H. Zhong, L. Yang, and B. Zhuo, "Exploring the fuel economy potential of ISG hybrid electric vehicles through dynamic

programming," *International Journal of Automotive Technology,* vol. 8, pp. 781-790, Dec 2007.

[11] C.-C. Lin, P. Huei, J. W. Grizzle, and K. Jun-Mo, "Power management strategy for a parallel hybrid electric truck," *IEEE Trans. Control Syst. Technol.,* vol. 11, pp. 839-49, 2003.

[12] J. Scordia, M. Desbois-Renaudin, R. Trigui, B. Jeanneret, F. Badin, and C. Plasse, "Global optimisation of energy management laws in hybrid vehicles using dynamic programming," *International Journal of Vehicle Design,* vol. 39, pp. 349-367, 2005.

[13] J. M. Lee and J. H. Lee, "Value function-based approach to the scheduling of multiple controllers," *Journal of Process Control,* vol. 18, pp. 533-542, 2008.

[14] W. B. Powell, "What you should know about approximate dynamic programming," *Naval Research Logistics,* vol. 56, pp. 239-249, 2009.

[15] W. Xiong, Y. Zhang, and C. Yin, "Optimal energy management for a series-parallel hybrid electric bus," *Energy Conversion and Management,* vol. 50, pp. 1730-1738, 2009.

[16] N. J. Schouten, M. A. Salman, and N. A. Kheir, "Energy management strategies for parallel hybrid vehicles using fuzzy logic," *Control Engineering Practice,* vol. 11, pp. 171-177, 2003.

[17] S. Kermani, S. Delprat, R. Trigui, and T. M. Guerra, "Predictive energy management of hybrid vehicle," in *IEEE Vehicle Power and Propulsion Conference*, Harbin, 2008.

[18] A. Bemporad and M. Morari, "Control of systems integrating logic, dynamics, and constraints," *Automatica,* vol. 35, pp. 407-27, 1999.

[19] S. C. Bengea and R. A. DeCarlo, "Optimal control of switching systems," *Automatica,* vol. 41, pp. 11-27, 2005.

[20] M. Zefran, "Continuous Methods for Motion Planning," Ph.D. Ph.D. Thesis, Computer and Information Science, University of Pennsylvania, Philadelphia, 1996.

[21] O. Von Stryk, "Numerical Solution of Optimal Control Problems by Direct Collocation. in Optimal Control—Calculus of Variations, Optimal Control Theory, and Numerical Methods," *International Series of Numerical Mathematics,* vol. 111, pp. 129-143, 1993.

[22] C. P. Neuman and A. Sen, "A suboptimal control algorithm for constrained problems using cublic splines," *Automatica,* vol. 9, pp. 601-13, 1973.

[23] A. Schäfer, P. Kühl, M. Diehl, J. Schlöder, and H. G. Bock, "Fast reduced multiple shooting methods for nonlinear model predictive control," *Chemical Engineering and Processing: Process Intensification,* vol. 46, pp. 1200-1214, 2007.

[24] K. Uthaichana, S. Bengea, and R. DeCarlo, "Suboptimal supervisory level power flow control of a hybrid electric vehicle," in *Proc. of IFAC World Congress*, Prague, 2005.

[25] M. Diehl, H. G. Bock, H. Diedam, and P. B. Wieber, "Fast direct multiple shooting algorithms for optimal robot control," in *Fast Motions in Biomechanics and Robotics*. vol. 340, M. Diehl and K. Mombaur, Eds., ed, 2006, pp. 65-93.

[26] D. DeHaan and M. Guay, "A new real-time perspective on non-linear model predictive control," *Journal of Process Control,* vol. 16, pp. 615-624, 2006.

[27] F. Martinsen, L. T. Biegler, and B. A. Foss, "A new optimization algorithm with application to nonlinear MPC," *Journal of Process Control,* vol. 14, pp. 853-865, 2004.

[28] R. Rao, S. Virudhula, and D. Rakhmatov, "Battery models for energy aware system design," *IEEE Computer,* vol. 36, pp. 1019-1030, 2003.

[29] M. Doyle, T. F. Fuller, and J. S. Newman, "Modeling of galvanostatic charge and discharge of the lithium/polymer/insertion cell," *Journal of Electrochemical Society,* vol. 140, pp. 1526-1533, 1993.

[30] T. F. Fuller, M. Doyle, and J. S. Newman, "Simulation and Optimization of the dual lithium ion insertion cell," *Journal of Electrochemical Society,* vol. 141, pp. 1-10, 1994.

[31] M. Pedram and Q. Wu, "Design consideration for battery-powered electronics," in *Proc. the36th Design Automation Conf.*, 1999, pp. 861-866.

[32] K. C. Syracuse and W. D. Clark, "A statistical approach to domain performance modeling for oxyhalide primary lithium batteries," in *Proc. 1997 IEEE 12th Annual Battery Conf., Application and Advances*, 1997, pp. 162-170.

[33] S. Gold, "A PSPICE macromodel of lithium-ion batteries," in *Proc. IEEE 12th Annual Battery Conf., Application and Advances*, 1997, pp. 215-222.

[34] C. F. Chiasserini and R. Rao, "Energy efficient battery management," *IEEE Journal on Selected Areas in Communication,* vol. 19, pp. 1235-1245, 2001.

[35] D. Rakhmatov and S. Virudhula, "An analytical high-level battery model for use in energy management of portable electronic systems," presented at the Proc. IEEE/ACM International Conf. Computer Aided Design, 2001.

[36] P. Rong and M. Pedram, "An analytical model for predicting the remaining battery capacity of lithium-ion batteries," in *Design Automation and Test in Europe Conference and Expositions*, 2003, pp. 1148-1149.

[37] A. Mainwaring, J. Polastre, R. Szewczyk, D. Culler, and J. Anderson, "Wireless sensor networks for habitat monitoring," in *Proc. ACM 1st Int. Workshop on Wireless Sensor Networks and Applications*, 2002, pp. 88-97.

[38] J. Khan and R. Vemuri, "Energy management in battery-powered sensor networks with reconfigurable computing nodes," in *Proc. Int. Conf. Field Programmable Logic and Applications*, 2005, pp. 543-546.

[39] A. Tiwari, P. Ballal, and F. L. Lewis, "Energy efficient wireless sensor network design and implementation for condition-based maintenance," *ACM Trans. Sensor Networks,* vol. 3, Mar. 2007.

[40] D. Rakhmatov and S. Virudhula, "A model for battery lifetime analysis for organizing applications on a pocket computer," *IEEE Trans. Very Large Scale Integration (VLSI) Systems,* vol. 11, pp. 1019-1030, 2003.

[41] M. R. Jongerden and B. R. Haverkort, "Which battery model to use?," in *Proc. 24th UK Performance Engineering Workshop*, 2008, pp. 76-88.

[42] S. C. Chapra, *Applied numerical methods with MATLAB for engineers and scientists*. New York: McGraw Hill, 2005.

[43] J. Aylor, A. Thieme, and B. Johnson, "A battery state-of-charge indicator for electric wheelchairs," *IEEE Trans. Industrial Electronics,* vol. 39, pp. 398-409, 1992.

[44] D. Rakhmatov and S. Virudhula, "Energy management for battery-powered embedded systems," *ACM Trans. Embedded Computing Systems,* vol. 2, pp. 277-324, 2003.

[45] K. Uthaichana, "Modeling and control of a parallel hybrid electric vehicle," Ph.D., Electrical and Computer Engineering, Purdue, West Lafayette, 2006.

[46] H. L. N. Wiegman and A. J. A. Vandenput, "Battery state control technique for charge sustaining applications," in *Proc. SAE Int. Congress and Exposition*, 1998.

[47] M. Viredaz and D. A. Wallach, "Power evaluation of a handheld computer: A case study," Compaq WRL Research Report, Tech. Rep. WRL-2001-1, Palo Alto, CA2001.

[48] G. L. Nemhauser and L. A. Wolsey, *Integer and Combinatorial Optimization*. New York: Wiley-Interscience, 1988.

[49] C. A. Floudas, *Nonlinear and Mixed-Integer Optimization: Fundamentals and Applications*. New York: Oxford University Press, 1995.

[50] K. Uthaichana, S. Bengea, R. DeCarlo, S. Pekarek, and M. Žefran, "Hybrid model predictive control tracking of a sawtooth driving profile for an HEV," in *Proceedings of the American Control Conference*, Seattle, WA, 2008, pp. 967-974.

[51] P. Gill, Murray, W. and Wright, M., *Practical Optimization*: Academic Press, 1981.

[52] R. Pfiffner and L. Guzzella, "Optimal operation of CVT-based powertrains," *Int. J. Robust Nonlinear Control,* vol. 11, pp. 1003-1021, 2001.

[53] M. Coleman, W. G. Hurley, and C. K. Lee, "An improved battery characterization method using a two-pulse load test," *IEEE Transactions on Energy Conversion,* vol. 23, pp. 708-713, 2008.

[54] S. Pekarek, K. Uthaichana, S. Bengea, R. DeCarlo, and M. Zefran, "Modeling of an electric drive for a HEV supervisory level power flow control problem," in *2005 IEEE Vehicle Power and Propulsion Conference*, Chicago, IL, USA, 2005.

[55] M. Anatone, R. Cipollone, and A. Sciarretta, "Control-Oriented Modeling and Fuel Optimal Control of a Series Hybrid Bus," presented at the SAE 2005 World Congress & Exhibition, , Detroit, MI, 2005.

[56] S.-I. Jeon, S.-T. Jo, Y.-I. Park, and J.-M. Lee, "Multi-mode driving control of a parallel hybrid electric vehicle using driving pattern recognition," *Journal of Dynamic Systems, Measurement and Control, Transactions of the ASME,* vol. 124, pp. 141-149, 2002.

[57] M. Koot, J. T. B. A. Kessels, B. de Jager, W. P. M. H. Heemels, P. P. J. van den Bosch, and M. Steinbuch, "Energy management strategies for vehicular electric power systems," *IEEE Transactions on Vehicular Technology,* vol. 54, pp. 771-82, 2005.

[58] J. Heywood, *Internal Combustion Engine Fundamentals*: McGraw-Hill, 1988.

[59] A. Giua, C. Seatzu, and C. Van Der Mee, "Optimal control of switched autonomous linear systems," Orlando, FL, 2001, pp. 2472-77.

[60] S. Hedlund and A. Rantzer, "Optimal control of hybrid systems," in *Proceedings of the IEEE Conference on Decision and Control*, Phoenix, AZ, USA, 1999, pp. 3972-77.

[61] S. Wei, K. Uthaichana, M. Zefran, R. A. DeCarlo, and S. Bengea, "Applications of numerical optimal control to nonlinear hybrid systems," *Nonlinear Analysis: Hybrid Systems,* vol. 1, pp. 264-279, 2007.

[62] Z. K. Nagy and F. Allgöwer, "Nonlinear model predictive control: From chemical industry to microelectronics," in *Proceedings of the IEEE Conference on Decision and Control*, Nassau, 2004, pp. 4249-4254.

เอกสารแนบหมายเลข3

Output จากโครงการวิจัยที่ได้รับทุนจาก สกว.

1. ผลงานตีพิมพ์ในวารสารวิชาการนานาชาติ

   Uthaichana, K., Bengea, S., DeCarlo, R., Pekarek, S., and Zefran, M. (2011). Hybrid Optimal Theory and Predictive Control for Power Management in Hybrid Electric Vehicle. Journal of Nonlinear Systems and Applications, 2(1), pp. 96-110.

2. การนำผลงานวิจัยไปใช้ประโยชน์

   2.1 เชิงนโยบาย: มีการนำความรู้ที่ได้ไปใช้ในการกำหนดนโยบายการซื้อและการจัดการแบตเตอรี่สำหรับรถไฟฟ้าที่ใช้มหาวิทยาลัยเชียงใหม่มูลค่า 20 ล้านบาท ในปี 2554

   2.2 เชิงสาธารณะ: มีการแลกเปลี่ยนและสร้างเครือข่ายความร่วมมือด้านงานวิจัยกับ stuttgart university

3. ผลงานอื่นๆ

   3.1 Rurgladdapan, J., Uthaichana, K., Kaewkham-ai, B. (2012) Li-Ion battery sizing and dynamic programming for optimal power-split control in a hybrid electric vehicle, ECTI 2012, Cha-Am, Thailand, May 2012.

ภาคผนวก

Journal of Nonlinear Systems and Applications (2011) 96–110
Copyright © 2011 Watam Press *http://www.watam.org/JNSA/*

HYBRID OPTIMAL THEORY AND PREDICTIVE CONTROL FOR POWER MANAGEMENT IN HYBRID ELECTRIC VEHICLE

Kasemsak Uthaichana[*], Raymond DeCarlo[†], Sorin Bengea[‡], Miloš Žefran[§], and Steve Pekarek

Abstract. This paper presents a nonlinear-model based hybrid optimal control technique to compute a suboptimal power-split strategy for power/energy management in a parallel hybrid electric vehicle (PHEV). The power-split strategy is obtained as model predictive control solution to the power management control problem (PMCP) of the PHEV, i.e., to decide upon the power distribution among the internal combustion engine, an electric drive, and other subsystems. A hierarchical control structure of the hybrid vehicle, i.e., supervisory level and local or subsystem level is assumed in this study. The PMCP consists of a dynamical nonlinear model, and a performance index, both of which are formulated for power flows at the supervisory level. The model is described as a bi-modal switched system, consistent with the operating mode of the electric ED. The performance index prescribing the desired behavior penalizes vehicle tracking errors, fuel consumption, and frictional losses, as well as sustaining the battery state of charge (SOC). The power-split strategy is obtained by first creating the embedded optimal control problem (EOCP) from the original bi-modal switched system model with the performance index. Direct collocation is applied to transform the problem into a nonlinear programming problem. A nonlinear predictive control technique (NMPC) in conjunction with a sequential quadratic programming solver is used to compute suboptimal numerical solutions to the PMCP. Methods for approximating the numerical solution to the EOCP with trajectories of the original bi-modal PHEV are also presented in this paper. The usefulness of the approach is illustrated via simulation results on several case studies.

Keywords. Hybrid Optimal Control, Nonlinear Model Predictive Control, Hybrid Electric Vehicles, Power management, Nonlinear Modeling

1 INTRODUCTION

In a hybrid propulsion system, power distribution from two or more energy sources/storages coordinate to deliver the performances demanded by the drivers while considering fuel efficiency and operational constraints. In a parallel hybrid electric vehicle (PHEV), the power demand can be delivered by the main power converter and/or the energy-storage device. Such energy storage devices could be batteries with or without supercapacitors [1, 2]. Examples of main power converters are internal combustion engines (ICEs), fuel cells [3–7], etc. In any case, as illustrated in [8–11], the power distribution among the main PHEV subsystems is computed at the supervisory level. The model of the PHEV at the supervisory level in this investigation is represented as a bi-modal switched system, as opposed to models with higher number of modes.

The description of the PMCP for constructing the model-based control strategies consists of the PHEV dynamical model, and a performance index (PI), both of which are formulated at the supervisory level. Approaches to solve the PMCP in the literatures can be categorized according to computational requirements as the real-time implementable type, and the global optimal type. The dynamic programming (DP) approaches compute optimal solutions over the driving cycles [8, 9, 12]. The curse of dimensionality of DP is well known. Thanks to recent advances in optimization, approximation approaches have been developed and alleviate this problem [13–15]. Since full knowledge of the driving cycles is still required, control using DP is not real-time implementable. Nevertheless, the results can be used as benchmarks for comparing the degree of optimality under replicated driving conditions.

Real-time implementable control strategies for the HEV, not optimal over driving cycles, usually undergo fine-tuning on the actual vehicles for desired performances under various assumptions and driving conditions. The list includes but is not limited to classical instantaneous/static optimization, adaptive equivalent fuel consumption minimization strategy (A-ECMS) [10], simplified rule based , fuzzy logic based [1, 16, 17], and neural network based [4].

The Nonlinear Model Predictive Control (NMPC) technique can provide suboptimal solutions with respect to

---

[*] Kasemsak Uthaichana is with Department of Electrical Engineering, Chiang Mai University, Chiang Mai, Thailand, (e-mail: kasemsak@chiangmai.ac.th). He is supported by grant Thailand Research Fund, Commission on Higher Education.

[†] Raymond DeCarlo and Steve Pekarek are with School of Electrical and Computer Engineering, Purdue University, West Lafayette, Indiana, USA (email: decarlo@ecn.purdue.edu, pekarek@purdue.edu)

[‡] Sorin Bengea is with Control Systems Group, Research Center, United Technologies, East Hartford, Connecticut, USA (email:sbengea@ieee.org)

[§] Miloš Žefran is with Department of Electrical and Computer Engineering, University of Illinois at Chicago, Chicago, Illinois, USA (email: mzefran@uic.edu)

the PI over the predictive-window. The degree of the optimality of the NMPC strategy is bounded by the instantaneous and the global optimizations. Note that the NMPC still requires a few predictive partitions within the optimization window (preview) of the driving profile, but not as extensively as the dynamic programming approach. The problem underlying the NMPC strategy for PMCP in [18] is a mixed integer optimization problem, e.g., [19], which is computationally expensive.

In this study, the embedding technique in [20] is adopted to formulate the PMCP as a (convex) embedded optimal control problem, EOCP, from the original (non-convex) switched optimal control problem, SOCP. Hence, the degree of complexity for the embedded version of the NMPC problem is lower.

Numerical methods for solving optimization problems include single shooting, multiple-shooting and direct collocation [21–24], etc. Difficulties with the single shooting method for the bi-modal PHEV is illustrated in [25]. Therein the necessary conditions are used to solve for the optimal controls. A superior version, called multiple shooting method, is adopted to solve an optimization problem in [26]. Instead of dealing with adjoint equations as in the multiple-shooting method, the direct collocation is adopted in this investigation. The embedding technique in conjunction with the direct collocation method is used to transform the problem into an NLP. The numerical solution to the NLP is computed using sequential quadratic programming (SQP) over a predictive window. More details on other methodologies to obtain solutions to NMPC problems can be found in [27, 28].

The following describes the paper organization. Section 2 summarizes bi-modal switched model for the PHEV. The performance index is detailed in Section 3. The PMCP is formulated as a multi-objective embedded optimal control problem at the supervisory level in Section 4. Section 5 reviews the embedding technique and presents sufficient conditions for existence of optimal solutions. Section 6 describes the numerical methodology. Section 7 presents the hybrid optimal and NMPC solutions for a sawtooth driving profile, and NMPC solutions for the EPA highway and US06 supplemental FTP (EPA high-speed) driving profiles.

2 PHEV as a Bi-Modal Switched System

The computation at the supervisory level is done based on the presumption that the desired power level can be implemented at the subsystem level. The local closed loop controllers must track the corresponding reference power demand, thereby decoupling the supervisory and local level control problems. Hence, the modeling at the supervisory level should reflect the closed loop behaviors of the subsystems.

2.1 Summary of Hardware Descriptions

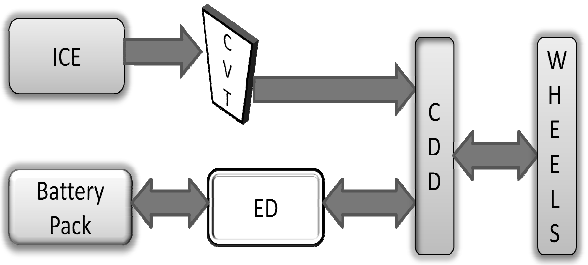

Figure 1: Power flow diagram of PHEV in this study

The main power source is the 1.9 L ICE, coupled to the driveshaft through a continuously variable transmission (CVT) and clutch in the post-transmission configuration. Thirty 13Ah 12V, lead-acid batteries in series are interfaced with a 30 kW induction ED. Hotel loads are handled by a traditional engine-based charging system. The coupling device and differential (CDD) acts as a summing junction for redirecting the power flow among the ICE-CVT, battery-ED, and the wheels. Figure 1 illustrates power distributions among the main subsystems.

2.2 Modes of Operation

In [9], five modes of operation describe the essential behavior of the PHEV. Since the PMCP complexity increases exponentially with increased numbers of modes [29, 30], an effort is put forth in this investigation to reduce the number of modes at the supervisory level.

Through careful consideration of the dynamics in each mode of operation, the essential behavior can be approximated using only two modes. As a preview, the mode reduction concept from five to two is illustrated via the numerical results obtained in this study in Fig. 2. In Fig. 2, $P_{ED} + P_{ICE} = P_{load}$, i.e., the sum of ED power, and ICE power is delivered to the load (the planetary efficiency is ignored for now).

The details of the mode reduction concept, when the HEV is operating, can be described as follows:

- For $v = 0$ ($P_{ED} \geq 0$): the engine-only mode ($P_{ICE} > 0, P_{ED} = 0$) corresponds to zero power flow from the ED which can be achieved by a zero-value of the ED control variable; the motor only mode ($P_{ICE} = 0, P_{ED} > 0$) corresponds to no power flow from the ICE that is also achievable by a zero-value of the engine control variable; in motor assisted mode ($P_{ICE} > 0, P_{ED} > 0$) both ICE power and ED power are strictly positive to the wheels achievable by non-zero control variables of the ED and ICE.

- For $v = 1$ ($P_{ED} < 0$): the regenerative-braking mode ($P_{load} < 0, P_{ED} < 0$) corresponds to a reverse of the ED power flow to charge the battery with ICE power at zero (or nearly so); and the engine-charging-battery mode ($P_{ICE} > 0, P_{ED} < 0$) corresponds to the case when the ED operates as a generator with positive ICE power flow to the ED and possibly to the wheels.

It can be seen that the two modes of operation at the supervisory level coincide with the modes of the ED denoted as $v = 0$ (motoring) and $v = 1$ (generating). The summary of the bi-modal switched system describing the essential dynamics of the power flow at the supervisory level is given next.

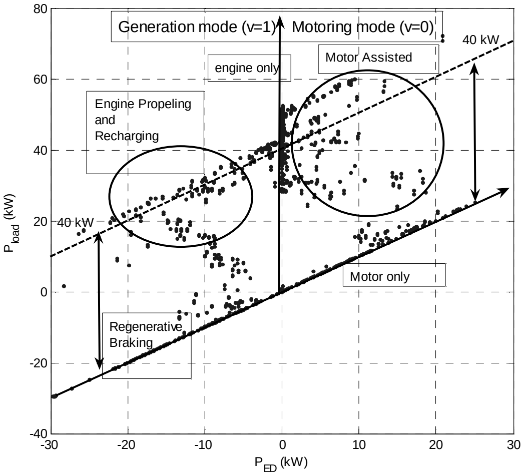

Figure 2: Power Flow strategy obtained in this study using NMPC tracking EPA highway profile showing the concept of mode reduction from five to two

2.3 HEV State Model Overview

The summary of the modeling equations, detailed in [31, 32], are summarized in this subsection. The input-output power relationships of subsystems consist of algebraic and dynamical equations. The input-output relationship is considered algebraic when the its internal power flow dynamics are much faster than others. The essential dynamical state is

$$x(t) \triangleq [P_{ICE}, SOC, V]^T, \tag{1}$$

where P_{ICE} is the ICE power, SOC is the battery state-of-charge, and V is the longitudinal vehicle's velocity. The mode-dependent nonlinear state equation for the PHEV in this study is:

$$\dot{x}(t) = f_{v(t)}(x(t), u_{v(t)}(t)) \tag{2}$$

where $f_v(\cdot)$ denotes the dynamics when motoring, $v = 0$, or when generating, $v = 1$. The modulating controls in modes-0/1 are

$$\begin{aligned} u_{0/1}(t) = \left[u_{ICE}(t), u_{FR}(t), u_{EM/GEN}(t)\right]^{\mathrm{T}} \\ \in \Omega \subset \mathbb{R}^3 \end{aligned} \tag{3}$$

where (i) the compact and convex set,

$$\Omega = [0,1] \times [0,1] \times [0,1] \tag{4}$$

(ii) $u_{ICE}(t) \in [0,1]$ modulates the maximum available ICE power; (iii) $u_{FR}(t)$ modulates the maximum frictional braking; and (iv) $u_{EM/GEN}(t) \in [0,1]$ modulates the maximum available ED power in the mode-0 and mode-1, respectively.

The motivation for this control structure is four-fold. First, the model is scalable in terms of numbers of power sources (ICE's or ED's) so that the corresponding increase in the number of operating modes leads to only a polynomial increase in complexity for numerical optimization methods [33]. Second, the model has a form compatible with hybrid optimal control theory. Third and more critically, the fact that the controls take values in a convex compact set Ω makes the PMCP amenable to hybrid optimization techniques. Fourth, any optimization algorithm searches for the optimal controls and switching function $v(t)$ in a hypercube as opposed to a (non-convex) state and time-dependent region.

2.3.1 State Equation for the ICE

The variable P_{ICE} denotes the unidirectional instantaneous ICE power flow, quantified at the flywheel and including losses due to parasitic loads. The ICE dynamical equation is given by equation (5), i.e.,

$$\begin{aligned} \dot{P}_{ICE} = -\tfrac{1}{\tau_{ICE}} P_{ICE} + \tfrac{1}{\tau_{ICE}} P_{ICE}^{\max}(\omega_{ICE}) \\ \cdot eng(\omega_{ICE}) \cdot u_{ICE}(t) \end{aligned} \tag{5}$$

where τ_{ICE} is the nominal engine power delivery delay averaging the effect of the firing delay, smoke limit map, crankshaft speed, fueling shot mode, etc. Further, this also ensures that the command handed down by the supervisory controller can be followed. $P_{ICE}^{\max}$ is an ω_{ICE} -dependent maximum available ICE power; ω_{ICE} is the CVT controller-selected engine speed using the strategy modified slightly from the speed-envelope for a non-hybrid ICE in [34]. Specifically,

$$\omega_{ICE} = (1-p)\,\omega_{ICE}^{\min}(V) + p\omega_{ICE}^{\max}(V) \tag{6}$$

where $p \in [0,1]$ modulates the speed curve according to the ICE power level; $\omega_{ICE}^{\min}(V)$ and $\omega_{ICE}^{\max}(V)$ are the minimum and the maximum allowable speeds at each vehicle's velocity and illustrated in Fig. 3. For better driveability, ICE-CVT's transition from non-engaged to engaged is not allowed when the vehicle's velocity is too low for jerk reduction. Note that in this study, the capitalized superscript indicates constant whereas lower-case superscripted means parameter dependent.

According to ICE dynamical equation (5), and the constraints on the input, (4), it can be shown that P_{ICE} belongs to the compact and convex set:

$$P_{ICE} \in [P_{ICE}^{MIN}, P_{ICE}^{MAX}] \subset \mathbb{R} \tag{7}$$

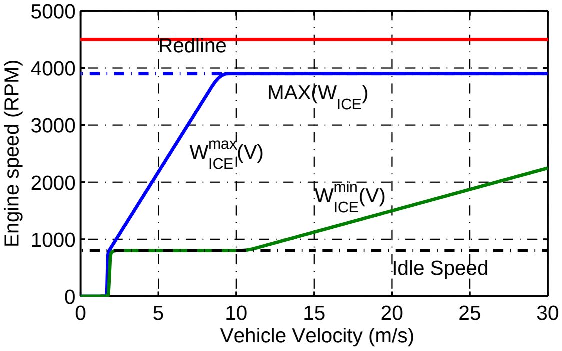

Figure 3: Maps of minimum and maximum engine speeds for each vehicle's velocity

The range of ICE power (7) is not an additional state constraint, but rather is a direct result from the aforementioned relationships. This information is useful during the computation of the solution as the numerical search-space is smaller.

2.3.2 State Equation for Battery Operation

For a relatively new battery, the normalized energy and the SOC are equivalent [35, 36]. The state equation describing the SOC dynamics is derived based on the conservation of power and energy. The parameters are computed to fit the battery data. The *partial* linearization about the mode-dependent nominal battery operating power, $P^v_{bat,nom}$, describing the SOC is given by:

$$\begin{aligned} \dot{SOC}\,(t) &= \tfrac{d_{3,v}}{W^{MAX}_{bat}} \left(P^v_{bat,nom}\right)^2 \\ &- \Big[\ln\left(d_{2,v} + d_{1,v}SOC(t)\right) + 2d_{3,v}P^v_{bat,nom} \\ &+ d_{4,v}\Big] \tfrac{P_{bat}}{W^{MAX}_{bat}} \end{aligned} \tag{8}$$

The validation result of this model against a variety of battery data appear in [37]. In equation (8), W^{MAX}_{bat} is the rated maximum battery energy, P_{bat} is the battery power either drawn by (positive for $v = 0$) or provided by the ED (negative for $v = 1$) and is implicitly controlled by $u_{EM/GEN}$. Specifically,

$$P_{bat} = \begin{cases} P^0_{ED,in}, & v = 0 \\ -P^1_{ED,out}, & v = 1 \end{cases} \tag{9}$$

$d_{k,v}$, $k = 1, ..., 4$ are the appropriate coefficients. The consideration of the recovery, cycling, and aging effects are beyond the scope of this investigation. This formulation makes equation (8) scalable to a variety of battery storage capacities and types.

2.3.3 State Equation for Vehicle Motion

The conventional longitudinal vehicle's velocity is described, not in terms of torques, but rather in terms of the acting power flow as:

$$\begin{aligned} \dot{V} &= -\left[\tfrac{k_{v1}}{m_c}V^2 + k_{v2}\cos\left(\alpha(t)\right)\right] sgn\left(V\right) \\ &-g\sin\left(\alpha(t)\right) + \tfrac{1000}{m_c(V+\varepsilon_V)}\left[P^v_{CDD,wh} - P_{FR}\right] \end{aligned} \tag{10}$$

In equation (10), ε_V is a regularization term; m_c is vehicle mass; $\frac{k_{v1}}{m_c}V^2$ is normalized aerodynamic drag; $k_{v2}\cos(\alpha(t))$ is the rolling resistance; $\alpha(t)$is the time-varying angle of road inclination; $P^v_{CDD,wh}$ is the power delivered from (≥ 0) and to (< 0) the CDD. Finally,

$$P_{FR} = P^{\max}_{FR}(V)u_{FR}(t) \tag{11}$$

is the frictional braking power. As a result from equation (10), the vehicle's velocity is also in an invariant set,

$$V \in \left[V^{MIN}, V^{MAX}\right] \subset R. \tag{12}$$

2.3.4 Mode Dependent ED Modeling Equations

The derivation of the ED algebraic input-output power flow equations for both modes can be found in [38]. The ED in this study, operated under a maximum torque/amp (MTA) control strategy, can be represented at the supervisory level as

$$P^v_{ED} = \eta^v_{ED}(\omega_{ED})P^v_{ED,in} \tag{13}$$

Each term in equation (13) is mode dependent. The ED output power is denoted P^v_{ED} , the efficiency $\eta^v_{ED}(\omega_{ED})$ strongly depends on the choice of closed-loop control, a phenomena largely underweighted in the HEV literature; $\omega_{ED} = \beta{\cdot}V$ is the ED rotor speed; β is a positive constant. The ED input power in modes 0 and 1 is

$$P^0_{ED,in} = P^{max}_{ED,in}\left(\omega_{ED}\right) \cdot u_{EM}(t) \tag{14}$$

$$P^1_{ED,in} = P^{max}_{ED,in}\left(\omega_{ED}\right) \cdot u_{GEN}(t) \tag{15}$$

where $P^{max}_{ED,in}\left(\omega_{ED}\right)$ is the speed dependent ED maximum input power modulated by the control $u_{EM}(t)$ in mode-0, and $u_{GEN}(t)$ in mode-1.

2.3.5 CVT and mode-dependent CDD Power Flow Equations

No power response lag between the input and output CVT powers is assumed at the supervisory level, leading to the algebraic equation

$$P_{cvt,out}(t) = \eta_{cvt}P_{cvt,in} \tag{16}$$

where η_{cvt} is the CVT efficiency; $P_{cvt,in}(t) = P_{ICE}$ is the CVT input power; and the output power is delivered to the CDD, i.e., $P_{cvt,out}(t) = P_{CDD,cvt}$.

The CDD's input/output power flows are given by

$$P^0_{CDD,wh}(t) = \eta_{cdd1}P_{CDD,cvt} + \eta_{cdd2}P^0_{CDD,ED} \tag{17}$$

and

$$P^1_{CDD,ED}(t) = \eta_{cdd2} P_{CDD,cvt} - \eta_{cdd2} P^1_{CDD,wh} \qquad (18)$$

(i) η_{cdd1}, and η_{cdd2} are the appropriate power transfer efficiency among the ED, CVT and wheels; (ii) $P^0_{CDD,ED} = P^0_{ED}$ is the propulsion power coming directly from the output of the ED in mode-0; in mode-1, $P^1_{CDD,ED} = P^1_{ED,in}$ is an output power port of the CDD providing mechanical power to the input of the ED (generator); (iii) in mode-0, $P^0_{CDD,wh} \geq 0$. However, in mode-1, $P^1_{CDD,wh}(t)$ can be either positive or negative. Note that $P^0_{CDD,wh}$ is represented as P_{load} in the mode reduction concept in Section 2.2.

3 PERFORMANCE INDEX

To incorporate the desired behaviors of the HEV operation, we consider the optimization functional for each mode, as follows:

$$\begin{aligned} J_v(x_0, u, [t_0, t_f]) \quad = \quad & g(t_0, x_0, t_f, x_f) \\ & + \int_{t_0}^{t_f} L_v(t, x, u)dt \end{aligned} \qquad (19)$$

The mode-dependent integrand $L_v(t, x, u)$ depends on the optimization objectives, such as minimizing only fuel consumption as in [39], or a combination of fuel consumption and emissions as in [9, 40, 41]. In this research the PI consists of terms that are consistent with the power flow management framework and have meaningful physical interpretations. The integral quadratic PI that uses the same integrand for both modes of operation, i.e., $L_0(t, x, u) = L_1(t, x, u)$ is adopted in this study. The integrand for both modes is

$$\begin{aligned} L_v \quad = \quad & C_V \big(V - V^{des}(t)\big)^2 \\ & + C_{ICE} \left(\tfrac{P_{ICE}}{\eta_{ICE}(\cdot)}\right)^2 + C_{FR}(P_{FR})^2 \end{aligned} \qquad (20)$$

The integrand penalizes the velocity tracking error, $C_V\big(V - V^{des}(t)\big)^2$, the frictional braking power, $C_{FR}(P_{FR})^2$, and the fuel usage. The fuel usage is approximated by ICE power usage divided by fuel conversion efficiency [42], i.e., $C_{ICE}\left(\frac{P_{ICE}}{\eta_{ICE}(\cdot)}\right)^2 = C_{ICE}(P_{fuel})^2$ where $\eta_{ICE}\left(P_{ICE}, V\right)$ is the ICE efficiency that depends on the ICE power-and-speed. Fig. 4 depicts the efficiency map of the ICE superimposed with the iso-efficiency curves.

The penalty on the variation in the boundary conditions, $g(t_0, x_0, t_f, x_f)$, in PI (19) is taken as $C_{bat}(\cdot)\big(SOC(t_f) - SOC^{NOM}\big)^2$. This choice of the penalty pushes the SOC at t_f toward the nominal level, SOC^{NOM}. It is also desirable to operate the SOC in a predefined range to prolong battery lifetime. It will be shown in the simulation results that this choice of penalty on the battery SOC can be used to encourage

$$SOC \in \left[SOC^{MIN}, SOC^{MAX}\right] \subset \mathbb{R} \qquad (21)$$

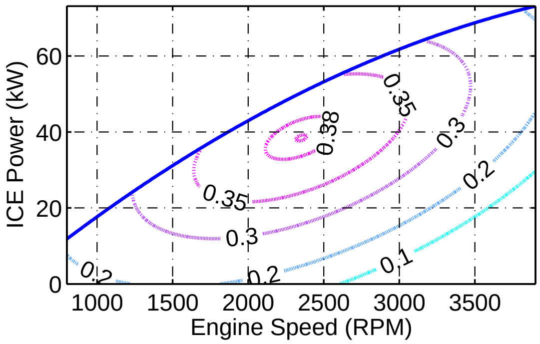

Figure 4: ICE power-vs.-engine speed superimposed with iso-efficiency curves

Note that if the constraints (21) are violated, the penalty term on the SOC must be more stringent. This SOC strategy is intended to enforce a charge-sustaining operation.

A more elaborate PI accounting for drivetrain losses in each mode has the form

$$\begin{aligned} L_v = & C_V^v\left(V - V^{des}\right) + C_{ICE}^v(P_{fuel})^2 \\ & + C_{cvt}^v(P_{cvt,loss})^2 + C_{CDD}^v\left(P_{C,loss}^v\right)^2 \\ & + C_{ED}^v\left(P_{ED,loss}^v\right)^2 + C_{bat}^v\left(P_{bat,loss}^v\right)^2 \\ & + C_{FR}^v(P_{FR})^2 \end{aligned} \qquad (22)$$

where the additional power loss terms are CVT losses, CDD loses, ED losses, and battery losses, whose identity should be clear from the notation. More details on the generalized PI can be found in [31].

4 POWER MANAGEMENT CONTROL PROBLEM AND THE EOCP

For the switched optimal control problem (SOCP), the modal switching function $v(t)$ belongs to a discrete set $\{0, 1\}$, $v(t) \in \{0, 1\}$. In contrast, for the EOCP the modal switching function $v(t)$ takes values in the closed interval $[0, 1]$, a continuum of possible values. The enlargement of $v(t) \in \{0, 1\}$ to $v(t) \in [0, 1]$ constitutes an embedding of the SOCP into a larger family of continuously parameterized problems. This embedding converts a non-convex SOCP into a convex EOCP. As per [20] the SOCP can almost always be solved by first solving the EOCP and any solution of the EOCP can be approximated to any degree of precision by some solution of the switched state model (2). Further, in this study, projection techniques are also presented as alternatives for approximating the EOCP solution by an SOCP trajectory.

4.1 Specification of the embedded optimal control problem

The embedding requires creating a convex combination of the vector fields of the switched state model according to the equation,

$$\begin{aligned} \dot{x}(t) &\triangleq f_E\left(x(t), u_0(t), u_1(t), v(t)\right) \\ &= [1-v(t)]\, f_0\left(x(t), u_0(t)\right) \\ &\quad + v(t) f_1\left(x(t), u_1(t)\right) \end{aligned} \tag{23}$$

where $u_i(t) \in \Omega$, $i = 0, 1$. Clearly if $v(t) = 0$, f_E reduces to the 0-mode vector field and similarly for $v(t) = 1$.

The performance index (PI) of the EOCP results from a similar convex embedding of the PIs associated with each mode of operation of the SOCP:

$$\begin{aligned} &J_E(x_0, u_0, u_1, v, [t_0, t_f]) = g(t_0, x_0, t_f, x_f) \\ &\quad + \int_{t_0}^{t_f} L_E(t, x, u_0, u_1, v) dt \\ &= g(t_0, x_0, t_f, x_f) \\ &\quad + \int_{t_0}^{t_f} \left[(1-v(t))\, L_0(t, x, u_0) \right. \\ &\quad \left. + v(t) L_1(t, x, u_1)\right] dt \end{aligned} \tag{24}$$

with $L_i(t, x, u_i)$, $i = 0, 1$, denoting the convex-in-u_i integrands of the PI. When $v(t) \in \{0, 1\}$, the minimization of (24) subject to (23) defines the SOCP, while when $v(t) \in [0, 1]$, the minimization of (24) subject to (23) constitutes the EOCP. Formally the EOCP (the structure for solving the PMCP) becomes:

$$\min_{u_0, u_1, v} \; J_E(x_0, u_0, u_1, v, [t_0, t_f]) \tag{25}$$

with $J_E(\cdot)$ given by (24), subject to

$$\dot{x}(t) = f_E(x(t), u_0(t), u_1(t), v(t)) \tag{26}$$

with f_E given in (23), $v(t) \in [0, 1]$, and u_0, $u_1 \in \Omega$.

4.2 Relationships between EOCP and SOCP

If the EOCP has a bang-bang type solution (wherein $v(t)$ only takes values in $\{0, 1\}$) then clearly it is also a solution to the original SOCP. Further it can be shown (Corollary 2 in [20]) that the set of trajectories of the switched system (equation (23) with $v(t) \in \{0, 1\}$) is dense in the set of trajectories of the embedded system (equation (23) with $v(t) \in [0, 1]$). Thus when/if the EOCP does not have a bang-bang type solution (wherein $v(t) \in (0, 1)$ for some non-zero measure sets of time) then the EOCP solution can be approximated by a trajectory of the switched system to any desired degree of precision. These relationships between the SOCP and EOCP motivate and justify the effort in determining SOCP solutions by solving the EOCP. Additional relationships between SOCP and EOCP can be found in [20].

4.3 Approximation to Singularities in EOCP

This subsection describes approximation techniques when the control $v(t)$ obtained via the EOCP is not bang-bang. When, $v(t) \in (0, 1)$, i.e., $v(t)$ takes on fractional values, over an interval $t_1 \le t \le t_2$, it would suggest that for the HEV the ED operate simultaneously in both modes for this time interval, an impossibility. In another words, when $v(t) \in (0, 1)$, the SOCP does not have a solution, but epsilon-approximating solutions to the EOCP can be constructed as follows. Given a desired error of approximation, ε, one can construct subintervals $t_1 < T_1 < T_2 .... < t_2$ such that $|T_{i+1} - T_i| < \delta$, where delta is generated based on ε, vector fields, f_i, and cost integrand, L_i. In the case when the switching interval–constrained by the embedded controller loop time, actuator bandwidth, etc–is larger than δ, one would have to increase the approximating error, ε, and re-construct the intervals. The approximating error will need to be sufficiently large to accommodate the constraint $\delta > T_{\min}$, where $T_{\min}$ is the minimum switching period.

The construction of the switching subintervals in the case of complex vector fields, such as the case for the HEV model, can be alleviated by considering empirical based switching intervals such as described below.

One approach to empirical switching is to average the fractional values of $v(t)$ over $t_1 \le t \le t_2$ and the average value, denoted $\bar{v}$, over $t_1 \le t \le t_2$, can be interpreted as a duty cycle, or a pulse width modulation (PWM) control. So there exists a time t' such that for $t_1 \le t < t'$, the system is in mode 0 and for $t' \le t < t_2$ the system is in mode 1 so that the average over the whole interval is $\bar{v} = \frac{t_2 - t'}{t_2 - t_1}$. Thus, a PWM or switched approximation to the embedded $v(t)$ is made.

The previously computed $u_i(t)$ are associated with the embedded solution $v(t)$, not the new approximation. One possibility is to simply use these values for each associated subinterval. A second possibility is to set $v(t)$ equal to its PWM approximation and then find the optimal u_0 and u_1 associated with this choice. Switching can be minimized by beginning the duty cycle for the next interval in the ending mode of the prior interval.

A third possibility is as follows: let $T_{\min}$ be the smallest switching interval of time. For each time unit, $t_1 \le t \le t_2 = t_1 + T_{\min}$, one can project the fractional value of $v(t)$ onto the set $\{0, 1\}$ according to the formula:

$$\left\| \overline{(1-v(t)) \cdot u_0(t)} \right\|_2 \begin{cases} \ge \left\| \overline{v(t) \cdot u_1(t)} \right\|_2 \Rightarrow v(t) = 0 \\ < \left\| \overline{v(t) \cdot u_1(t)} \right\|_2 \Rightarrow v(t) = 1 \end{cases} \tag{27}$$

where over-bars denote averages over the interval $t_1 \le t \le t_2 = t_1 + T_{\min}$. As before one can either use the previously calculated values of u_i or resolve the optimization with $v(t)$ fixed at the desired mode. For the simulation studies of this work, equation (27) was used to fix the bang-bang solution for $v(t)$ and then the optimization was resolved for the best pair of $u_i(t)$ given the fixed mode sequence.

4.4 Embedded PI for PMCP

As mentioned earlier, the integrand and the penalty on the boundary conditions in both modes are the same. The embedded PI for the PMCP is obtained by substituting appropriate terms in the PI (24), i.e.,

$$\begin{aligned} J_E \;=\; & C_{bat}(\bullet)\big(SOC(t_f) - SOC^{NOM}\big)^2 \\ & + \int_{t_o}^{t_f} \Big(C_V\big(V - V^{des}(t)\big)^2 \\ & + C_{ICE}\Big(\tfrac{P_{ICE}}{\eta_{ICE}(\bullet)}\Big)^2 \\ & + C_{FR}\big(P_{FR}^{MAX}(\bullet)u_{FR}(t)\big)^2\Big)\, dt \end{aligned} \tag{28}$$

where the physical meaning of each term is given in Section 3.

5 SUMMARY ON THEORETICAL FOUNDATIONS

When the discrete input $v \in \{0, 1\}$ presents, it renders, in general, the SOCP non-convex. For a variety of assumptions on system vector fields f_v, an SOCP performance index, and mode-switching penalties and constraints, several approaches have been employed in the literature for characterizing and computing SOCP solutions, consisting of: searches over or assumptions on mode sequences and switching instants, after which one computes the continuous control values and the cost to compare the different scenarios. These approaches do not allow the switching function to be chosen in concert with the continuous time control as is the case with the embedded approach.

Discussing neither sufficient conditions for optimality nor account for the singular solution scenarios, Riedinger et al. (1999) applies directly the Maximum Principle to the SOCP. For a larger class of systems, and with a cost that depends on the mode sequence, Sussmann (1999) derives necessary conditions for optimality via a generalized Maximum Principle. Other approaches include preassigned switching sequence method (for a limited class of problems) in [43], and a hybrid Bellman inequality approach in [44]. Mixed integer programming (MIP) approaches have also been employed to find optimal solutions [19]. Solving the problem using MIP methods, however, is non-deterministic polynomial-time hard (NP-hard); indeed the scalability of this technique is problematic [45].

The nonconvexity of the problem and the inapplicability of the mentioned existing techniques—too general and impractical, or very specific results, or insufficient characterization of solutions— to the SOCP has led to the development of the parameterized family of problems, the EOCP, set forth in the previous section.

5.1 EOCP: Sufficient Existence Conditions

This section summarizes the main sufficient conditions for EOCP solutions. Sufficient conditions for optimality are [Theorem 9, in [20]]:

(i) the admissible pair set (control, trajectory) is nonempty;

(ii) the points $(t, x(t))$ are included in a compact set for all$t \in [t_0, t_f]$;

(iii) the terminal set is compact;

(iv) the input constraint set is compact and convex;

(v) the vector fields f_0 and f_1 are linear in their (control) inputs u_0, and u_1, respectively i.e.,

(S1) $f_0(t, x, u_0) = A_0(t, x) + B_0(t, x)u_0$

(S2) $f_1(t, x, u_1) = A_1(t, x) + B_1(t, x)u_1$

(vi) for each$(t, x(t))$, the integrands of the penalty functions, $L_0(t, x, u_0)$ and $L_1(t, x, u_1)$, are convex functions of u_0, and u_1, respectively.

Based on the assumptions made on the input constraint set and on the vector fields f_0 and f_1, one can conclude that conditions (i), (ii), and (iv) are met. Further, a sufficiently large compact set can be substituted for the terminal set, meeting condition (iii). Condition (v) is also met as it can be observed based on the modeling equations from Sections 2. Specifically, the power terms that depend on the continuous control inputs, are factored into the product of a control input and a term that depends on the state, $x(t)$. Utilizing the form of these power terms, and the forms of $L_0(t, x, u_0)$ and $L_1(t, x, u_1)$ one concludes that condition (vi) is also met. Hence the EOCP has a solution.

The above sufficient conditions only guarantee the existence of the EOCP's solutions, but do not provide a solution methodology. In conjunction with the SOCP-EOCP relationships mentioned above, the necessary conditions obtained by direct application of the Maximum Principle [38] provide a method for obtaining at least suboptimal solutions of the SOCP. By using this approach, the optimization problem is transformed into a two-point boundary value problem on the state and adjoint equations. The single shooting method is applied to compute the numerical solution in [25], and the solution is very sensitive with respect to the co-state initial condition. The multiple shooting method can be applied to reduce the sensitivity issue. This paper takes an alternate approach for computing numerical solutions to the EOCP, i.e., via the direct collocation method, described in the next section.

6 NUMERICAL TECHNIQUE AND NMPC

This section briefly describes the direct collocation method and the nonlinear model predictive control (NMPC) strategy. Both are used in conjunction to formulate the PMCP as a nonlinear programming problem (NLP).

6.1 Discretization via Direct Collocation

Given the PI (28) and the state equation and constraints of equations (23), one discretizes these equations using the direct collocation method. The discretization of the PI uses a variation of the trapezoidal rule and constraint equations use the mid-point rule, respectively. These discretized equations convert the EOCP into a finite dimensional NLP where states and inputs are treated as unknown variables. The direct collocation technique consists of several steps that have two main stages: (i) time discretization, and state and input function approximations by a finite number of polynomial basis functions; (ii) approximation of the continuous state dynamics and cost index integrand by discrete-state and discrete-input-dependent counterparts.

Without going through a lengthy derivation, the continuous time interval $[t_0,\ t_f]$ is discretized into a sequence of points $t_0 < t_1 < t_2 < \cdots < t_{N-1} < t_N = t_f$ where, for simplicity, we take $t_j - t_{j-1} = h$, for $j = 1, ..., N$. A "hat" notation is also used to distinguish the numerically estimated state and control values from their actual counterparts that are "hatless", e.g., $\hat{x}_j = \hat{x}(t_j)$, $\hat{u}_{0,j} = \hat{u}_0(t_j)$, $\hat{u}_{1,j} = \hat{u}_1(t_j)$and $\hat{v}_j = \hat{v}(t_j)$. The collocation method used here assumes triangular basis functions for the state and piecewise constant basis functions (derivatives of triangular functions) for the controls. Specifically, the estimated state is given by

$$\hat{x}(t) = \sum_{j=0}^{N} \hat{x}_j \varphi_j(t) \tag{29}$$

where the $\hat{x}_j$'s are to be determined and the triangular basis functions are given by

$$\varphi_j(t) = \begin{cases} \frac{t-t_{j-1}}{h}, & t_{j-1} < t \le t_j \\ \frac{t_{j+1}-t}{h}, & t_j < t \le t_{j+1} \\ 0, & \text{elsewhere} \end{cases} \tag{30}$$

We note two points: the method is not restricted to using triangular basis functions and each of the $\varphi_j(t)$'s is a time shift of the previous one.

As summarized in [24], the theoretical approach for computing the controls is to extend the state space with new state variables, $x_{ext} \in R^{m+1}$, whose derivative are the desired controls, $u(t) \in R^m$ and $v(t) \in [0,1] \subset R$, to be computed. However, our choice of triangular basis functions for the states renders the control inputs piecewise constant and we simply solve directly for these (constant) control values. Specifically, the estimates of the control inputs are given by

$$\begin{bmatrix} \hat{u}(t) \\ \hat{v}(t) \end{bmatrix} = \sum_{j=1}^{N} \begin{bmatrix} \hat{u}_j \\ \hat{v}_j \end{bmatrix} \psi_j(t) \tag{31}$$

where the piecewise constant basis functions are given by

$$\psi_j(t) = \begin{cases} 1 & t_{j-1} < t \le t_j \\ 0 & \text{elsewhere} \end{cases} \tag{32}$$

The essence of the midpoint rule in the collocation method is to enforce the constraints at the midpoints of each interval $[t_{j-1}, t_j]$ for $j = 1, ..., N$. There results the discretized embedded state dynamics

$$\begin{aligned} \hat{x}_j = \hat{x}_{j-1} + h \cdot (1 - \hat{v}_j) \cdot f_0\left(\tfrac{\hat{x}_{j-1}+\hat{x}_j}{2}, \hat{u}_{0j}\right) \\ + h \cdot \hat{v}_j \cdot f_1\left(\tfrac{\hat{x}_{j-1}+\hat{x}_j}{2}, \hat{u}_{1j}\right) \end{aligned} \tag{33}$$

for $j = 1, ..., N$, with $f_0(\cdot)$ and $f_1(\cdot)$ the discretized state dynamics in modes -0 and -1, respectively. Thus, the solution to the EOCP is given by the following NLP: Minimize

$$\begin{aligned} \hat{J}_E = C_{bat}(\boldsymbol{\cdot})\left(\hat{SOC}_N - SOC^{NOM}\right)^2 \\ + \sum_{j=1}^{N} \tfrac{1}{2} h \left\{ L_E\left(t_j, \hat{x}_j, \hat{u}_{0j}, \hat{u}_{1j}, \hat{v}_j, \hat{p}_j\right) \right. \\ \left. + L_E\left(t_{j-1}, \hat{x}_{j-1}, \hat{u}_{0j}, \hat{u}_{1j}, \hat{v}_j, \hat{p}_j\right) \right\} \end{aligned} \tag{34}$$

over the controls $(\hat{u}_j, \hat{v}_j) \in \Omega \times [0,1]$, subject to equation (33) and all other equality/power flow constraints represented as $g(\hat{x}_{j-1}, \hat{x}_j, \hat{u}_j, \hat{v}_j, \hat{p}_j) = 0$. Here $L_E(\cdot)$ is the integrand of equation properly discretized and $\widehat{p}_j$ represents the various power flows in the model.

6.2 Nonlinear Model Predictive Control

The NMPC solution strategy in this study uses a moving four-second predictive-window with the control applied over one-second sub-interval. In particular the NLP for $t = t_j$ is solved over $[t_j, t_{j+1}, t_{j+2}, t_{j+3}, t_{j+4}]$ instead of the entire driving cycle. The resulting control at each iteration is applied only over $[t_j, t_{j+1}]$ to the system model. Using the constant controls computed by NMPC algorithm, the system model is then simulated over $[t_j, t_{j+1}]$ to obtain an updated state at t_{j+1}. This updated state represents what would be measured in a real-world implementation of the NMPC control [28, 46].

We let $t_{f,j}$ denote the final time of each NMPC iteration, and hence is the final time in the PI (28). Further for the NMPC strategy the coefficient penalizing the deviation from nominal SOC, $C_{bat}(t_{f,j})$ is linearly interpolated according to the equation

$$C_{bat}(t_{f,j}) = (t_{f,j}/t_f\ )C_{bat}^{nom} \tag{35}$$

Otherwise, the NMPC control will try to maintain the SOC at SOC^{NOM} over each iteration unduly restricting the use of battery power.

Difficulties arise for real world implementation since this strategy presumes knowledge of t_f. Nevertheless, it can be entered by drivers, or becomes an adaptive function of the recent history of the vehicle's power consumption. The estimation problem of t_f is beyond the scope of this paper.

In the beginning of each NMPC window, we assume the knowledge of the current road grade (e.g., through an accelerometer or future GPS). The control algorithms assume that over each partition of the NMPC window, the road grade is constant at the value at the beginning of the NMPC window. Although the road grade may change over the NMPC window, since the control is only applied over the first partition, after which a new measurement is taken, potential error is believed negligible.

7 SIMULATION RESULTS

The NLP of the PMCP is applicable to various numerical solvers such as AIMMS, TOMLAB, etc. In this study, a sequential quadratic programming (SQP) based NLP solver, *fmincon*, is adopted. This section details simulation results for PHEV tracking different driving profiles. The first set of simulations compare the overall hybrid optimal control and the NMPC tracking the sawtooth driving profile with road grades. The next simulation details the PHEV tracking the standard 765 s EPA Highway driving profile to which is added a sinusoidal road grade to better exercise the controller performance. The second simulation looks at the 600 s US06 FTP supplemental driving schedule. The numerical solutions to various driving profiles are shown below.

7.1 Optimal and NMPC Tracking of Sawtooth Velocity Profile with Road Grades: Cases 1 and 2

The performances of the overall hybrid optimal control and the NMPC strategies are compared using the sawtooth driving profile suggested in [32]. The sawtooth profile demands higher rates of acceleration/deceleration than typical driving cycles. To further test the limits of performance of the vehicle powertrain, positive sinusoidal road grades are superimposed in this paper.

The coefficients of the PI (28) are $C_V = 10$, $C_{ICE} = 10^{-3}$, $C_{FR} = 10^{-4}$, and $C_{bat}(\cdot) = C_{bat}^{nom} = 10^5$. This study compares the performances of two hybrid optimal control strategies. Case 1 uses a control that minimizes the PI of (28) with the above coefficients over the entire driving cycle and is thus optimal over the driving cycle. Case 2 constructs an NMPC version that can be compared to the optimal solution. Figure 5 shows that initially the vehicle in both cases fail to provide perfect tracking. Initial tracking error is due to the insufficient available propelling power from the ICE and ED both of which already operate at their maximum levels, as shown in Fig. 6 for case 1. As per Fig. 6(a), the ICE is off at startup (propelling from ED alone) due to the closed-loop local control constraint, until a minimum operating speed of 800 RPM is reached. Further, the tracking error during the first 14 s for the NMPC version is larger due to the fact that the NMPC decides to turn the ICE on slightly later. The rest of the driving profiles except the peak at 30 s can be tracked relatively well in both cases.

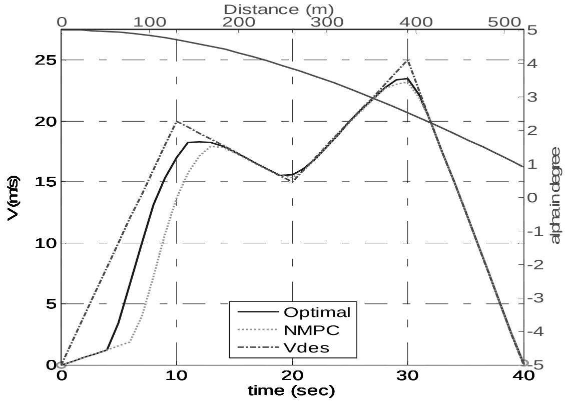

Figure 5: Velocity tracking performance for overall optimal hybrid control and NMPC tracking sawtooth profile with road grades

After 30 s, when the desired velocity is decreasing and the road grades are positive but small; the ICE is turned off (Fig. 6(a)) and the ED provides negative power to charge the battery in both cases as shown in Fig. 6(b). Between 14 and 21 s the ICE in case 1 provides power both to charge the battery and to the wheels, while in case 2, the ICE only provides propelling power. The ICE profiles in this specific region for the NMPC are lower and circled in Fig. 7(a). This contributes to slightly better fuel economy for the NMPC version of 14.7 MPG vs. 14.2 MPG for case 1.

Simultaneously, the ED in case 1 operates as a generator (mode-1) more often, specifically between 14 and 21 s, as depicted in Fig. 6(b) and Fig. 7(b). The NMPC hands down a non-generating decision in this time interval because of a relatively lower penalty (coefficient) on the deviation from nominal SOC according to (35).

Figure 8 depicts the battery SOC profiles. Case 1 shows consistency with the mode of operation and returns to the vicinity of the 60% nominal level at the end of the cycle.

In case 2, SOC deviation is only mildly penalized allowing lower levels than in case 1 during the first half cycle. In the second half of the driving cycle, with an increasing penalty on the deviation from nominal SOC, the NMPC tries to recharge the battery and returns SOC to the level slightly lower than in case 1.

During the last 10 s, the ED operates as a generator

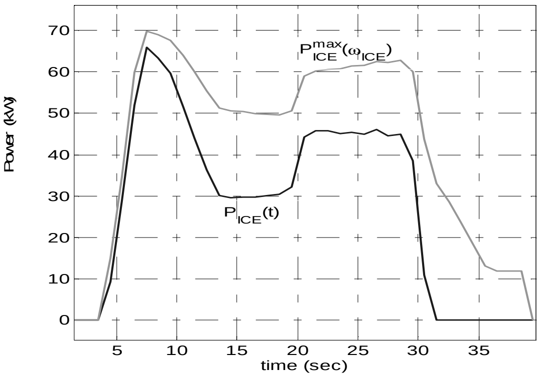

(a) ICE power

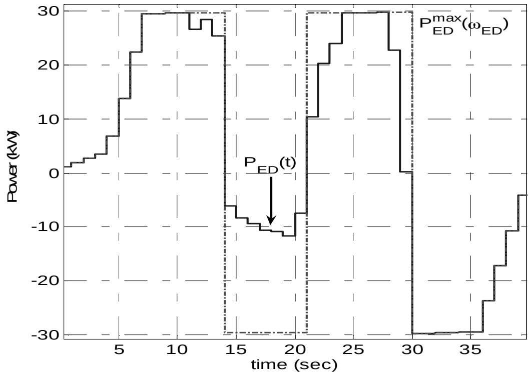

(b) ED power

Figure 6: Output power for tracking sawtooth profile with road grades in case 1

in both cases as expected to provide regenerative braking power. Further, the demanded power is more (negative) than the maximum level that the ED can deliver in both cases as shown in Fig. 6(b). To achieve the desired velocity tracking, the extra kinetic energy is expended in frictional braking as shown in Fig. 9. Indeed, frictional braking is only used during the last 10 s of the driving profile as one would expect.

7.2 NMPC Tracking of EPA Highway Driving Cycle with Road Grade: Case 3

In this case study, the vehicle is to follow the EPA highway driving profile for 765 seconds on a nonzero road grades as shown in Fig. 10. Also shown (solid sinusoidal) in Fig. 10, is the road grades, which has a positive angle (uphill) over the first 382.5 s, and then has a negative angle (downhill) over the final 382.5 s

The coefficients of the PI (28) are the same as those used in the sawtooth driving profiles with a sliding penalty on the deviation of the SOC from nominal as $t \to t_f = 765$ s Fig. 10 shows that the NMPC strategy provides nearly perfect tracking for this case.

Since there is very little penalty on battery usage initially (see (35)) and a relatively significant penalty on fuel

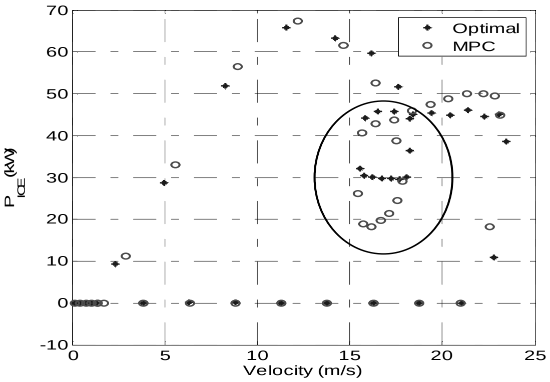

(a) ICE power

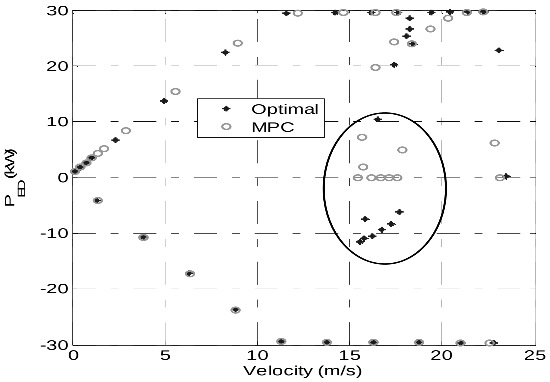

(b) ED power

Figure 7: Output profiles vs vehicle's velocity for overall optimal hybrid control and NMPC tracking sawtooth with road grades showing ICE power and ED power

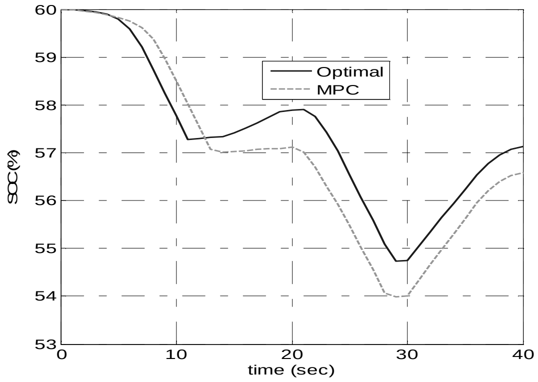

Figure 8: Battery SOC for overall optimal hybrid control and NMPC tracking sawtooth with road grades

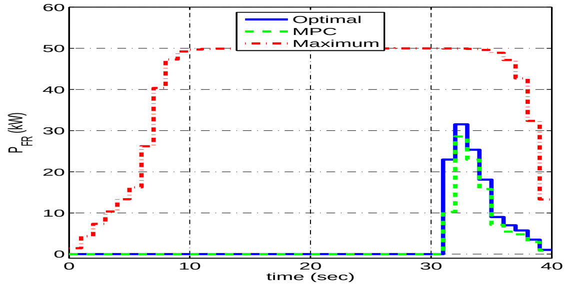

Figure 9: Frictional-braking power for overall optimal hybrid control and NMPC tracking sawtooth with road grades

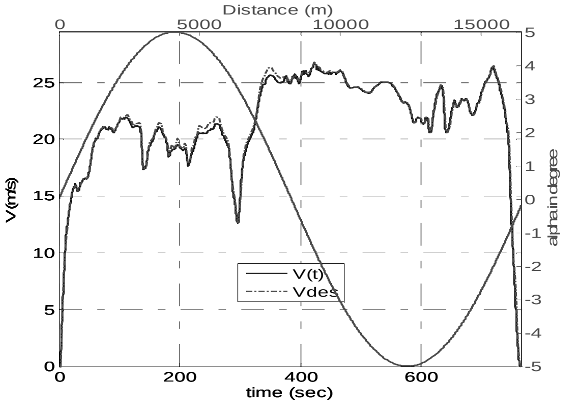

Figure 10: Velocity tracking performances for case 3 on a road grades whose angle in degrees is indicated by the sinusoidal curve with values in degrees on the right vertical axis

consumption, mode 0 is active for 135 s (Fig. 11(a)) at which the desired velocity starts to decrease.

Initially, the ED supplies roughly 20 kW of propelling power, and eventually decays to near zero at 135 s. In contrast, the ICE is initially off, and gradually ramps to supply propulsion demand reach 40 kW at roughly 135 s (Fig. 13). In other words, the NMPC strategy decides to drain the power from the ED-battery pack to as low as 45% during this time period as shown in Fig. 11(b).

After 60 seconds, the ICE power contribution continues to ramp and then remains relatively constant at about 45 kW until 400 seconds as per Fig. 13. Over this period, fuel efficiency is relatively high according to the ICE efficiency map in Fig. 4.

Around 260 sec, the road profile becomes less demanding and the vehicle operates in the generating mode more often. Further, after 382.5 sec, the road grades are negative, which leads to regenerative braking. Figure 12 shows that the ED operates more frequently in the generating mode for recharging the battery back to its nominal value of 0.6. Further, there is little need for propelling power to maintain perfect tracking, hence the ICE is off most of the time in the second half of the driving cycle.

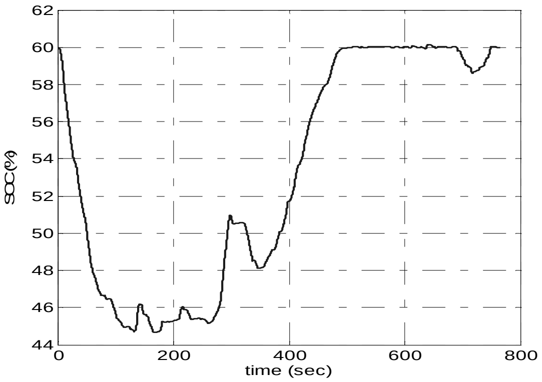

(a) Mode of operation

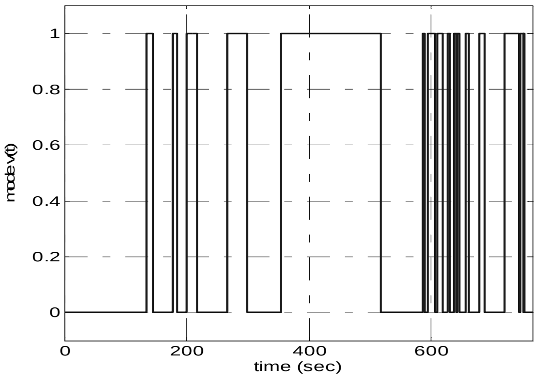

(b) Battery SOC

Figure 11: NMPC strategy for tracking EPA highway profile showing Mode of operation and Battery SOC Profiles

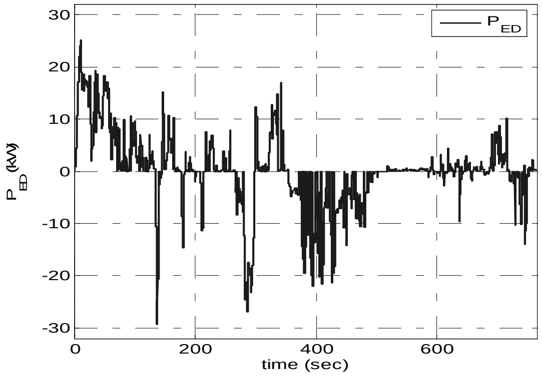

Figure 12: ED output power profiles for PHEV tracking EPA highway using NMPC strategy

The map of the ICE power over the engine speeds' range shows denser data in the fuel efficient region. Hysteresis appears as the result of the dynamics (lag) in the engine power during the acceleration and deceleration as shown in Fig. 14. Figure 15 shows the operation of the

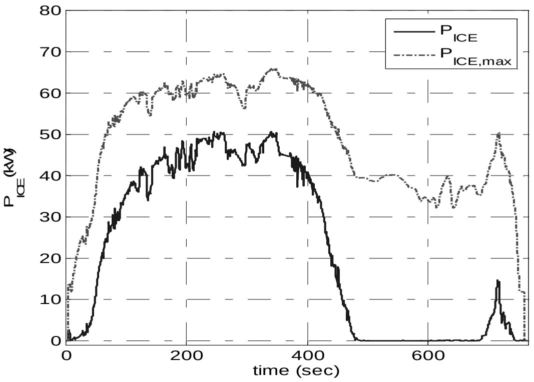

Figure 13: ICE power usages for PHEV tracking EPA highway using NMPC strategy

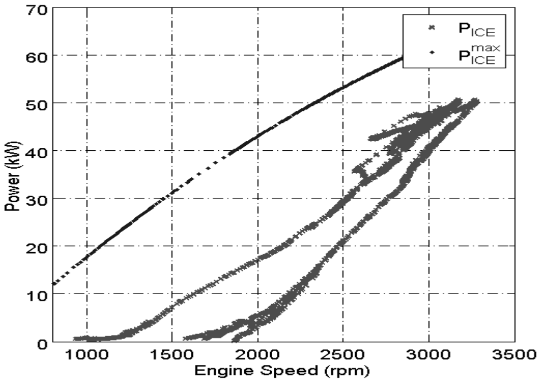

Figure 14: Trajectories of ICE power vs. engine speed for PHEV tracking EPA highway using NMPC strategy showing acceleration/deceleration hysteresis

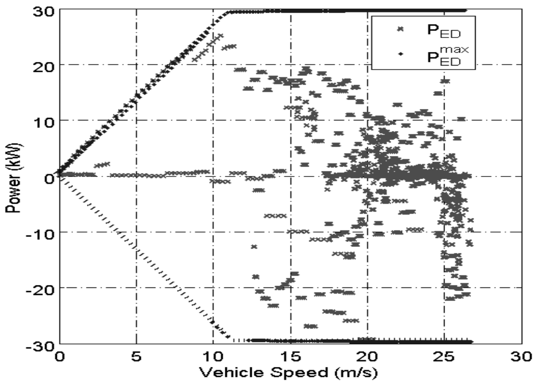

Figure 15: Trajectories of ED power vs. vehicle for PHEV tracking EPA highway profile using NMPC

ED over the range of vehicle speeds.

In the presence of the sinusoidal road grade over the cycle, the fuel economy is 27.5 mpg, lower than the 32 mpg (similar to current hybrid SUVs on the market) when the road is flat due to (i) frictional braking losses during the negative road grades to maintain velocity tracking and (ii) inefficiencies in energy recovery from regenerative braking. The simulation result in the case of vehicle tracking the EPA highway velocity profile on a flat road is not included in this paper due to space limitations, but it can be found in [31].

One concludes that the NMPC strategy performs very well while sustaining the constraint on the final SOC. Further, the resulting power distributions in this case study is used to justify the concept of five-to-two mode reduction as shown in Fig. 2. The 40 kW line is drawn in the figure to indicate a rough ICE power level that is fuel efficient for a medium engine-speed range.

7.3 MPC Tracking of the US06 supplemental FTP Driving Profile: Case 4

In this case study, we again use NMPC to track the 600 second US06 supplemental FTP driving schedule, which demands higher accelerations and more aggressive velocity variation/limits than the standard EPA city and highway schedules as shown in Fig. 16. The coefficients of the PI are the same as those in the previous cases. Figure 16 again shows that the NMPC almost perfectly tracks the desired velocity profile.

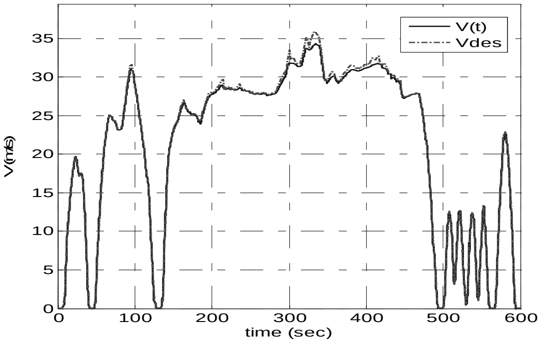

Figure 16: US06 supplemental FTP driving profile and vehicle tracking performance

The aggressive nature of the velocity profile forces the ED to operate close to maximum power levels in both modes (Fig. 17(a)) while the power usage of the ICE mimics (Fig. 17(b)) the shape of the velocity profile.

To meet the transient acceleration demands, NMPC puts the ED in the motoring mode during acceleration and in the generating mode during deceleration. During the non-transient power demand, the middle of the driving cycle, the ED is often off or provides relatively low power and the ICE provides most of the power as it can operate around its more fuel efficient level. Overall, estimated fuel efficiency averages at 23 mpg, a lower value than the EPA highway profile of 32 due to the more aggressive power demands of this case study.

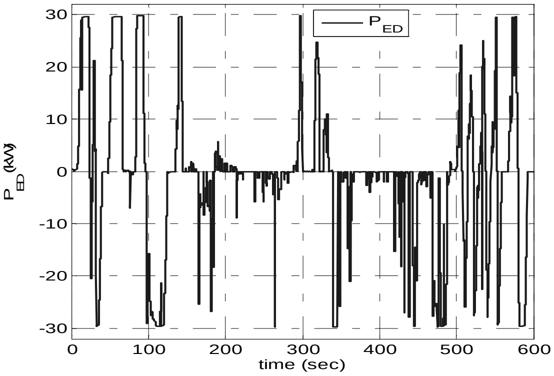

(a) ED output power

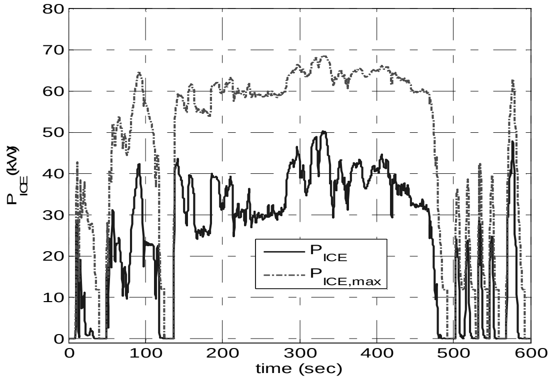

(b) ICE output power

Figure 17: Plots of ED output power and ICE output power profiles in case 4

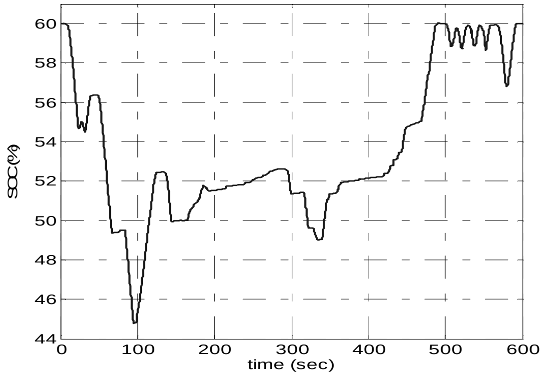

(a) Battery SOC

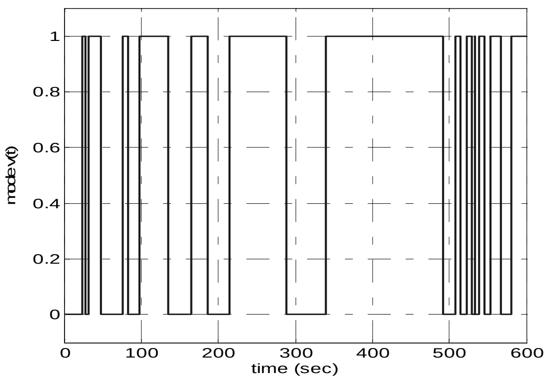

(b) Mode of operation

Figure 18: Case 4: Battery SOC and Mode of operation profiles

During the first 100 sec of the driving schedule, the HEV operates primarily in the motoring mode draining the battery to an SOC of about 45 percent as shown in Fig. 18(a). The aggressive acceleration driving profile in concert with the relatively low penalty on the SOC deviation from the nominal level contributes to the NMPC selection of this strategy. Afterward, as the penalty on the SOC deviation increases linearly toward the final time of 600 sec, the SOC rises toward the nominal level of 0.6 with more frequent time in mode 1.

Mode switching in both cases, using the strategy outlined in section 4.3, is reasonable, and consistent with the velocity variations in the driving profile as shown in Fig. 18(b).

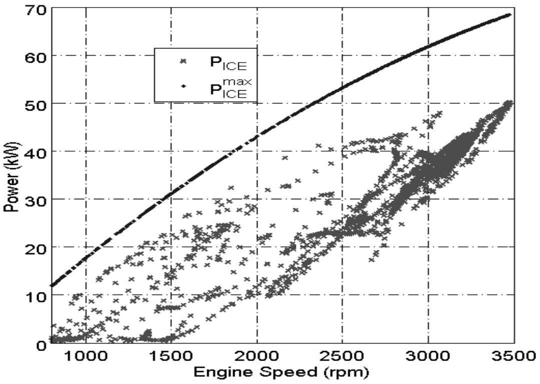

Figure 19: Trajectories of ICE power vs. engine speed for PHEV tracking US06 FTP profile using NMPC strategy

Similar to case 3, the nature of the modified speed envelope strategy for the CVT dictates higher engine speed for higher ICE power as depicted in Fig. 19. Dense engine data is located around 40 kW. In contrast to case 3, wider spread in the trajectories of the ICE on the power-vs-speed map can be observed in this case. Frequent operations on the ED maximum power-vs-speed envelope (in both motoring and generating) are also observed in this case, as depicted in Fig. 20. These characteristics in the ICE and the ED power profiles reflect greater variety of demands in the US06 FTP profile.

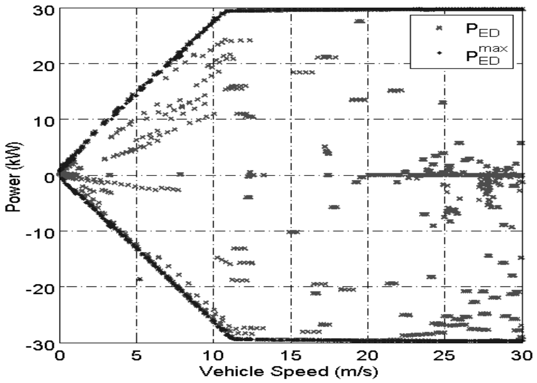

Figure 20: Trajectories of ED power vs. vehicle for PHEV tracking US06 FTP profile using NMPC strategy

7.4 CONCLUSIONS

An application of the hybrid optimal control for solving the power management control problem (PMCP) in a parallel electric hybrid vehicle (PHEV) has been illustrated in this paper. The advantages outlined in [20] motivate solving for the optimal/suboptimal power flow as the solution to the embedded version of the problem, i.e., the EOCP. The solution of the EOCP can be obtained via a number of numerical techniques.

In this study, the numerical solution is obtained by converting the original infinite dimensional problem into a finite dimensional nonlinear programming problem (NLP) using the direct collocation technique. Then, the resulting NLP is solved via a sequential quadratic programming algorithm. Requiring a short predictive window, the NMPC strategy is applied to solve the PMCP for the sawtooth, EPA highway, and US06 supplemental FTP driving profiles. The simulations show that the NMPC can track the driving profiles quite well unless there is insufficient available power to achieve the tracking as illustrated in case of the sawtooth profile with positive road grades. In practice, vehicle control strategies are often PID and maps/look-up tables based. The resulting NMPC profiles can help providing additional information on how to improve the existing look-up tables or tuning the gain-scheduling maps in the PID based controllers.

References

[1] O. Erdinc, B. Vural, and M. Uzunoglu, "A wavelet-fuzzy logic based energy management strategy for a fuel cell/battery/ultra-capacitor hybrid vehicular power system," *Journal of Power Sources*, vol. In Press, Corrected Proof, 2009.

[2] A. Pesaran, J. Gonder, and M. Keyser, "Ultracapacitor applications and evaluation for hybrid electric vehicles," in *Advanced Capacitors World Summit 2009*, (La Jolla, California), 2009.

[3] F. Barbir, H. Gorgun, and X. Wang, "Relationship between pressure drop and cell resistance as a diagnostic tool for pem fuel cells," *Journal of Power Sources*, vol. 141, no. 1, pp. 96–101, 2005.

[4] J. B. Cao and B. G. Cao, "Neural network sliding mode control based on on-line identification for electric vehicle with ultracapacitor-battery hybrid power," *International Journal of Control, Automation and Systems*, vol. 7, no. 3, pp. 409–418, 2009.

[5] D. Feroldi, M. Serra, and J. Riera, "Energy management strategies based on efficiency map for fuel cell hybrid vehicles," *Journal of Power Sources*, vol. 190, no. 2, pp. 387–401, 2009.

[6] Q. Shen, M. Hou, X. Yan, D. Liang, Z. Zang, L. Hao, Z. Shao, Z. Hou, P. Ming, and B. Yi, "The voltage characteristics of proton exchange membrane fuel cell (pemfc) under steady and transient states," *Journal of Power Sources*, vol. 179, no. 1, pp. 292–296, 2008.

[7] T. E. Springer, T. A. Zawodzinski, and S. Gottesfeld, "Polymer electrolyte fuel cell model," *Journal of the Electrochemical Society*, vol. 138, no. 8, pp. 2334–2342, 1991.

[8] G. Q. Ao, J. A. Qiang, H. Zhong, L. Yang, and B. Zhuo, "Exploring the fuel economy potential of isg hybrid electric vehicles through dynamic programming," *International Journal of Automotive Technology*, vol. 8, pp. 781–790, Dec 2007.

[9] C.-C. Lin, P. Huei, J. W. Grizzle, and K. Jun-Mo, "Power management strategy for a parallel hybrid electric truck," *IEEE Trans. Control Syst. Technol.*, vol. 11, no. 6, pp. 839–49, 2003.

[10] P. Pisu and G. Rizzoni, "A comparative study of supervisory control strategies for hybrid electric vehicles," *IEEE Transactions on Control Systems Technology*, vol. 15, no. 3, pp. 506–518, 2007.

[11] G. Rizzoni, L. Guzzella, and B. M. Baumann, "Unified modeling of hybrid electric vehicle drivetrains," *IEEE/ASME Transactions on Mechatronics*, vol. 4, no. 3, pp. 246–257, 1999.

[12] J. Scordia, M. Desbois-Renaudin, R. Trigui, B. Jeanneret, F. Badin, and C. Plasse, "Global optimisation of energy management laws in hybrid vehicles using dynamic programming," *International Journal of Vehicle Design*, vol. 39, no. 4, pp. 349–367, 2005.

[13] J. M. Lee and J. H. Lee, "Value function-based approach to the scheduling of multiple controllers," *Journal of Process Control*, vol. 18, no. 6, pp. 533–542, 2008.

[14] W. B. Powell, "What you should know about approximate dynamic programming," *Naval Research Logistics*, vol. 56, no. 3, pp. 239–249, 2009.

[15] C. S. P. H. Kim, N., "Optimal control of hybrid electric vehicles based on pontryagin's minimum principle," *IEEE Transactions on Control Systems Technology*, 2010. cited By (since 1996) 0; Article in Press.

[16] N. J. Schouten, M. A. Salman, and N. A. Kheir, "Energy management strategies for parallel hybrid vehicles using fuzzy logic," *Control Engineering Practice*, vol. 11, no. 2, pp. 171–177, 2003.

[17] W. Xiong, Y. Zhang, and C. Yin, "Optimal energy management for a series-parallel hybrid electric bus," *Energy Conversion and Management*, vol. 50, no. 7, pp. 1730–1738, 2009.

[18] S. Kermani, S. Delprat, R. Trigui, and T. M. Guerra, "Predictive energy management of hybrid vehicle," in *IEEE Vehicle Power and Propulsion Conference*, 2008 IEEE Vehicle Power and Propulsion Conference, VPPC 2008, (Harbin), 2008.

[19] A. Bemporad and M. Morari, "Control of systems integrating logic, dynamics, and constraints," *Automatica*, vol. 35, no. 3, pp. 407–27, 1999.

[20] S. C. Bengea and R. A. DeCarlo, "Optimal control of switching systems," *Automatica*, vol. 41, no. 1, pp. 11–27, 2005.

[21] C. P. Neuman and A. Sen, "A suboptimal control algorithm for constrained problems using cublic splines," *Automatica*, vol. 9, pp. 601–13, 1973.

[22] A. Schfer, P. Khl, M. Diehl, J. Schlder, and H. G. Bock, "Fast reduced multiple shooting methods for nonlinear model predictive control," *Chemical Engineering and Processing: Process Intensification*, vol. 46, no. 11, pp. 1200–1214, 2007.

[23] O. Von Stryk, "Numerical solution of optimal control problems by direct collocation. in optimal controlcalculus of variations, optimal control theory, and numerical methods," *International Series of Numerical Mathematics*, vol. 111, pp. 129–143, 1993.

[24] M. Zefran, *Continuous Methods for Motion Planning.* Ph.d. thesis, University of Pennsylvania, Philadelphia, 1996.

[25] K. Uthaichana, S. Bengea, and R. DeCarlo, "Suboptimal supervisory level power flow control of a hybrid electric vehicle," in *Proc. of IFAC World Congress*, (Prague), July 2005.

[26] M. Diehl, H. G. Bock, H. Diedam, and P. B. Wieber, "Fast direct multiple shooting algorithms for optimal robot control," in *Fast Motions in Biomechanics and Robotics* (M. Diehl and K. Mombaur, eds.), vol. 340 of *Lecture Notes in Control and Information Sciences*, pp. 65–93, Springer, 2006.

[27] D. DeHaan and M. Guay, "A new real-time perspective on nonlinear model predictive control," *Journal of Process Control*, vol. 16, no. 6, pp. 615–624, 2006.

[28] F. Martinsen, L. T. Biegler, and B. A. Foss, "A new optimization algorithm with application to nonlinear mpc," *Journal of Process Control*, vol. 14, no. 8, pp. 853–865, 2004.

[29] C. A. Floudas, *Nonlinear and Mixed-Integer Optimization: Fundamentals and Applications.* New York: Oxford University Press, 1995.

[30] G. L. Nemhauser and L. A. Wolsey, *Integer and Combinatorial Optimization.* Discrete Mathematics and Optimiazation, New York: Wiley-Interscience, 1988.

[31] K. Uthaichana, *Modeling and control of a parallel hybrid electric vehicle.* PhD thesis, Purdue, West Lafayette, December 2006 2006.

[32] K. Uthaichana, S. Bengea, R. DeCarlo, S. Pekarek, and M. Zefran, "Hybrid model predictive control tracking of a sawtooth driving profile for an hev," in *Proceedings of the American Control Conference*, 2008 American Control Conference, ACC, (Seattle, WA), pp. 967–974, 2008.

[33] P. Gill, W. Murray, and M. Wright, *Practical Optimization.* Academic Press, 1981.

[34] R. Pfiffner and L. Guzzella, "Optimal operation of cvt-based powertrains," *Int. J. Robust Nonlinear Control*, vol. 11, no. 11, pp. 1003–1021, 2001.

[35] M. Coleman, W. G. Hurley, and C. K. Lee, "An improved battery characterization method using a two-pulse load test," *IEEE Transactions on Energy Conversion*, vol. 23, no. 2, pp. 708–713, 2008.

[36] R. Rao, S. Virudhula, and D. Rakhmatov, "Battery models for energy aware system design," *IEEE Computer*, vol. 36, pp. 1019–1030, 2003.

[37] V. Agarwal, K. Uthaichana, R. DeCarlo, and L. H. Tsoukalas, "Development and validation of a battery model useful for discharging and charging power control and lifetime estimation," *IEEE Transactions on Energy Conversion*, vol. 25, pp. 821–835, August 2010.

[38] S. Pekarek, K. Uthaichana, S. Bengea, R. DeCarlo, and M. Zefran, "Modeling of an electric drive for a hev supervisory level power flow control problem," in *2005 IEEE Vehicle Power and Propulsion Conference*, (IEEE Cat. No.05EX1117C), (Chicago, IL, USA), IEEE, 2005.

[39] M. Anatone, R. Cipollone, and A. Sciarretta, "Control-oriented modeling and fuel optimal control of a series hybrid bus," in *SAE Technical Papers 2005-01-1163*, 2005.

[40] S.-I. Jeon, S.-T. Jo, Y.-I. Park, and J.-M. Lee, "Multi-mode driving control of a parallel hybrid electric vehicle using driving pattern recognition," *Journal of Dynamic Systems, Measurement and Control, Transactions of the ASME*, vol. 124, no. 1, pp. 141–149, 2002.

[41] M. Koot, J. T. B. A. Kessels, B. de Jager, W. P. M. H. Heemels, P. P. J. van den Bosch, and M. Steinbuch, "Energy management strategies for vehicular electric power systems," *IEEE Transactions on Vehicular Technology*, vol. 54, no. 3, pp. 771–82, 2005.

[42] J. Heywood, *Internal Combustion Engine Fundamentals.* McGraw-Hill, 1988.

[43] A. Giua, C. Seatzu, and C. Van Der Mee, "Optimal control of switched autonomous linear systems," in *Proceedings of the IEEE Conference on Decision and Control*, vol. 3, (Orlando, FL), pp. 2472–77, Institute of Electrical and Electronics Engineers Inc., 2001.

[44] S. Hedlund and A. Rantzer, "Optimal control of hybrid systems," in *Proceedings of the IEEE Conference on Decision and Control*, vol. 4, (Phoenix, AZ, USA), pp. 3972–77, IEEE, Piscataway, NJ, USA, 1999.

[45] S. Wei, K. Uthaichana, M. Zefran, R. A. DeCarlo, and S. Bengea, "Applications of numerical optimal control to nonlinear hybrid systems," *Nonlinear Analysis: Hybrid Systems*, vol. 1, no. 2, pp. 264–279, 2007.

[46] Z. K. Nagy and F. Allgwer, "Nonlinear model predictive control: From chemical industry to microelectronics," in *Proceedings of the IEEE Conference on Decision and Control*, vol. 4 of *2004 43rd IEEE Conference on Decision and Control (CDC)*, (Nassau), pp. 4249–4254, 2004.

Li-Ion battery sizing and dynamic programming for optimal power-split control in a hybrid electric vehicle

Jariya Rurgladdapan*[,1], Kasemsak Uthaichana*[,2], Boonsri Kaewkham-ai*[,3]

*Department of Electrical Engineering, Faculty of Engineering, Chiang Mai University
Chiang Mai, Thailand
[1]jar-may@hotmail.com, [2]kasemsak@chiangmai.ac.th, [3]boonsri@eng.cmu.ac.th

***Abstract*—This study considers the tradeoff between the weight and the storage capacity among different sizes of LiFePO4 battery packs for optimal powertrain design in a parallel hybrid electric vehicle (HEV). Proper power-split strategy between the engine power and the battery power can improve the performance of the designed powertrain. Dynamic programming (DP) approach is adopted to compute the optimal power-split and to evaluate the performance of each battery storage capacity. The fuel economy of HEV with different battery capacities are evaluated against different driving schedules i.e. Japan 10/15 mode, UDDS, HWFET, UN/ECE, and SFTP. Since the solution to the DP is computed offline (within a few minutes for each profile), some rule extractions are illustrated and can be used to improve the powertrain control strategy onboard.**

Keywords-hybrid electric vehicle; li-ion battery; dynamic programming; battery sizing; optimal power control

I. INTRODUCTION

Increasing energy efficiency is critical in the automotive industry as more stringent requirement is imposed by the government of US, EU, among many others. Hybrid electric vehicle (HEV) enhances the overall energy efficiency by the addition of the electric drive and battery pack as the secondary source of power. Primary power sources of HEV can be the traditional (diesel or gasoline) fossil fuels, or a cleaner option such as proton exchange membrane fuel cell (PEMFC). Abundant literatures are available for the control of fossil fuel hybrid [1-3], or PEMFC hybrid [4, 5]. The sizing ratio of the primary source to the battery pack is important. If the battery pack is too large, the vehicle becomes heavy by the battery weight, and unnecessary losses in the energy occur; the overall efficiency is decreased. On contrary, with insufficient battery storage capacity onboard, the battery pack is put on burden to keep up with the power demand. In this situation, the battery's state of charge (SOC) would likely undergo wider range of operating condition [6-8]. This can dramatically decrease the state of health (SOH), and shorten the battery lifetime [9]. The hardware can be well designed, but without proper power management strategy, full HEV benefits will not be realized. Hence, the battery sizing along with the choice of power distribution between the engine and the battery-electric drive (ED) are critical in the design of the hybrid powertrain.

This paper presents an application of dynamic programming (DP) approach [10, 11] to design the optimal battery sizing along with the proper power split on the hybrid powertrain. The HEV powertrain is the lithium-ion-phosphate (LiFePO4) battery connected to an ED and a gasoline engine to propel the Honda civic chassis. The advantages of this battery include long lifetime, and more immune than other types of Li-Ion batteries to the thermal runaway issue. The power-split among the battery-ED and the gasoline engine is computed via the DP approach. The vehicle is subject to various driving schedules such as Japan 10/15mode, Urban Dynamometer Driving Schedule (UDDS), Highway Fuel Economy Test (HWFET), United Nations Economic Commission for Europe (UN/ECE), and Supplemental Federal Test Procedure (SFTP). Since, the optimization using DP requires complete knowledge of the driving profile, the computation is currently done offline. The fuel economy for different LiFePO4 battery sizings are computed and compared. The best average fuel economy is the main criteria for making the recommendation on the optimal battery size. To obtain useful information for real-time control, a few rule-based strategies are extracted from the simulation results. The rest of this paper is as follows. Section 2 describes the HEV model at the power management level. Section 3 summarizes the numerical technique in this work. The simulation results are presented in section 4. The conclusion is presented last.

II. HEV MODEL

In this study, the considered HEV is a Honda Civic with a mass of 1189 kg equipped with a 1.4L gasoline engine. Parallel to the internal combustion engine (ICE) are pack(s) of 244V LiFePO4 connected to a 10kW induction motor in the pre-transmission configuration. The mathematical details of the powertrain components are given next.

A. Internal Combustion Engine

The maximum power of this engine is 61 kW@5700 rpm and the maximum torque is 119 Nm@3300 rpm. Fig. 1 shows the engine efficiency $\eta_{ICE} = \eta_{ICE}(\omega_{ICE}, T_{ICE})$ as a function of the engine speed ω_{ICE}, and the engine torque T_{ICE} (Nm). The ICE efficiency is moderate to high in the region of 2000-5000 rpm, as shown in Fig. 1. Due to the physical constraint,

---

The work by Kasemsak Uthaichana was financially supported by grant Thailand Research Fund, Commission on Higher Education.

ω_{ICE} must operate within limits, and the engine torque cannot exceed the maximum ICE torque, $T_{ICE}^{\max}$, i.e.,

$$1000 \le \omega_{ICE} \le 6000, \text{ and } \quad T_{ICE} \le T_{ICE}^{\max}(\omega_{ICE}) \qquad (2.1)$$

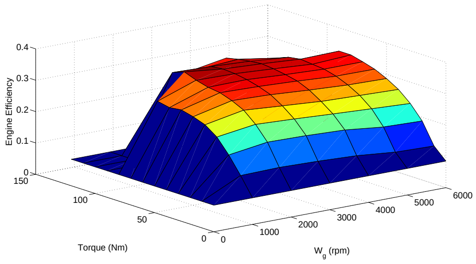

Fig. 1 ICE efficiency as a function of ICE speed and engine torque.

B. *The Electric Drive*

The 10kW ED subsystem is a 3-phase induction motor connected to an inverter. In mode-0, ED is a motor where the propelling power is drawn from the battery pack. In mode-1, the mechanical power is converted to the electrical power via the ED operating as a generator. The operating efficiency of the ED, η_{ED}, as a function of the ED speed, ω_{ED} and the magnitude ED torque, $|T_{ED}|$, is depicted in Fig. 2.

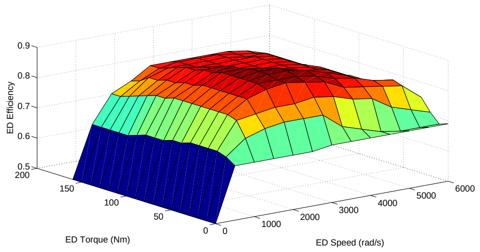

Fig. 2 The ED efficiency as a function of the ED speed and ED torque.

The ED operation is subject to the following maximum and minimum constraints,

$$0 \le \omega_{ED} \le 6000, \text{ and } |T_{ED}| \le T_{ED}^{\max}(\omega_{ED}) \qquad (2.2)$$

where $T_{ED} \ge 0$ in mode-0, and $T_{ED} < 0$ in mode-1; $T_{ED}^{\max}$ is the maximum ED torque (Nm). Since the ED dynamics is much faster than other subsystems, algebraic relationship between its maximum input $P_{ED,in}^{\max}$ (kW) with the modulating control u_{ED} and the output power P_{ED} (kW) through η_{ED} is given by

$$P_{ED} = \eta_{ED} \cdot P_{ED,in}^{\max} \cdot u_{ED} \qquad (2.3)$$

C. *Lithium Iron Phosphate battery (LiFePO4)*

The secondary source of power in the HEV is (A123) the LiFePO4 battery with energy density of 108 Wh/kg. Each battery pack consists of forty-four 2.3Ah 3.3V LiFePO4 battery connected in series. Efficiency of battery depends on the current level. Based on the simple Thevenin equivalent circuit, the battery charging and discharging current I_{bat} can be calculated by

$$I_{bat}(t) = \frac{-V_{oc} - \sqrt{V_{oc}^2 + 4R_{i,bat} \cdot P_{bat}(t)}}{2R_{i,bat}} \qquad (2.4)$$

V_{OC} is the open circuit voltage; $R_{i,bat} = R_{i,bat}(SOC)$, the internal battery resistance varies with the SOC; $P_{bat}(t)$ is the battery power at its terminal, (≥ 0) in mode-0, and (< 0) in mode-1.

D. *Lower powertrain and Vehicle dynamic*

Connected to the driveshaft is the gear box with differentials and the wheels. The gear selection depends on the driving speed, and is scheduled according to Table I.

TABLE I GEAR LEVEL DEPENDING ON SPEED OF DRIVING

Gear	**Driving Speed (m/s)**	
	Increasing Speed	**Decreasing Speed**
1	0-4.9	0-1.8
2	5-9.9	1.9-9.6
3	10-14.3	9.7-11.8
4	14.4-19.3	11.9-14.7
5	more than 19.3	more than 14.7

Power demand of the vehicle to overcome the aerodynamic drags, the vehicle inertia, and the rolling friction is presented as

$$P_{dem} = (mv\dot{v} + k_{v1}v^3 + mvk_{v2}) \qquad (2.5)$$

where m is vehicle mass; v is driving speed; $\dot{v}$ is vehicle acceleration rate; k_{v1} is vehicle aerodynamic drag coefficient; k_{v2} is the rolling loss coefficient.

III. DYNAMIC PROGRAMMMING

The advantage of DP is that the optimal solution found is the global optimizer. The obvious drawback is the well-known curse of dimensionality, i.e., excessive computational time in the problem with large dimensions of the state and the control. To circumvent this problem, the control problem has been methodologically reduced to a single state and a single control. Given the discrete state equation of the form,

$$x_{k+1} = f(x_k, u_k) \qquad (3.1)$$

where x_k is the state variable, and u_k is the control at each k time grid, for $k \in \{0, ..., N\}$. First, the state and the control must be quantized into a number of levels, N_X, and N_U. The DP computes for the optimal control sequence $\{u_0, u_1, ..., u_{N-1}\}$, where u_k is applied for the time interval

$\left[k, k+1\right)$, by optimizing the objective function (3.2) backward in time from N to 0.

$$J(x_0) = h\left(x_N\right) + \sum_{k=0}^{N-1} I_D(x_k, u_k) \qquad (3.2)$$

where $h\left(x_N\right)$ is the final penalty function, I_D is the cost integrand at time k. The optimization problem is decomposed into steps by first evaluating the final penalty, i.e.,

$$J_{N,N}(x_N) = h(x_N) \qquad (3.3)$$

for each quantized level of x_N. At the K iteration backward in time where $k = N - K$, the problem becomes the search for the optimal control $u^*_{N-K}(x_{N-K})$ for each of the possible current state x_{N-K}. The optimal cost-to-go

$$J^*_{N-K,N}\left(x_{N-K}\right) = \min_{u_{N-K}} \left\{ I_D\left(x_{N-K}, u_{N-K}\right) + J^*_{N-(K-1),N}\left(f\left(x_{N-K}, u_{N-K}\right)\right)\right\}$$

Once, the process propagates back to the beginning $(K = N, \text{or } k = 0)$. The optimal control $\{u_k^*\}$ is available for almost all initial state x_0, with the optimal cost $J^*_{0,N}\left(x_0\right)$.

IV. PROBLEM FORMULATION

To formulate the HEV control problem amenable to the DP approach, time interval is set at 1 s, sufficient for the ICE and the gear to reach its steady state conditions. The state variable is the SOC, $x_k = SOC_k$ and the control is $u_k = u_{ED}$.

A. *Objective function*

The fuel consumption is objective function to be minimized by the control strategy as in (3.4)

$$J(x_0) = \sum_{k=0}^{N-1} \dot{m}_f = \sum_{k=0}^{N-1} \left(\frac{T_{ICE} \cdot \omega_{ICE}}{\eta_{ICE} \cdot LHV} \right) \qquad (3.4)$$

where LHV is the low heating value of 42.5 MJ/kg. The average fuel economy (FE) can be computed as

$$FE = \frac{1}{L} \sum_{k=0}^{N-1} v_k \cdot 1 \qquad (3.5)$$

where L is volume of total fuel usage for the sequence $\{v_k\}$.

B. *Other Constraints*

Besides the subsystem constraints described in section 2, other operating constraints include the state constraint

$$SOC_{\min} = 0.4 \le SOC \le SOC_{\max} = 0.8 \qquad (3.6)$$

V. SIMULATION RESULTS

A. *Simulation Setting and Results*

The SOC is quantized into 61 grids with the initial and the final state of 0.6 ,i.e. $SOC_N = SOC_0 = 0.6$. The ED input is created with 21 grids where the lowest grid is -1 and highest grid is 1 modulating the maximum power.

Various fuel economy obtained under different driving profiles as the results of DP are summarized in TABLE II.

TABLE II FUEL ECONOMY FOR DIFFERENT BATTERY SIZINGS

Battery Packs	**JAPAN**	**HWFET**	**UDDS**	**UN/ECE**	**SFTP**	**average**
1	29.337	30.139	25.425	38.025	26.582	29.902
3	31.842	31.886	29.988	45.686	29.518	33.784
4	32.012	32.039	30.163	46.000	29.917	34.026
5	32.108	32.087	30.208	46.143	**29.954**	34.100
6	**32.154**	32.107	30.258	46.190	29.925	34.127
7	32.133	32.126	30.246	46.247	29.954	**34.141**
8	32.114	32.123	**30.266**	**46.284**	29.921	**34.142**
9	32.121	**32.135**	30.226	46.263	29.871	34.123
10	32.080	32.132	30.214	46.201	29.827	34.091

The HEV with 7-8 battery packs yield higher average fuel economy than the others. UN/ECE profile is the easiest driving schedule; hence, its fuel economy is the highest. In contrast, SFTP is the most aggressive cycle, and the fuel economy reflects accordingly. Considering the difference in the average fuel economy among 4-10 packs is less than 0.14 km/l, the HEV with 4 battery packs provides the appropriate balance between fuel economy and the battery cost/weight. This is equivalent to roughly 1.3 kWh of battery storage energy onboard. If lowering the battery cost is a higher priority, one can also drop the number of battery packs to 3 on the powertrain with 0.24 km/l drop in average fuel economy. The SOC of HEV in all driving schedules are in range 0.54-0.63 within the limit of 0.4-0.8 as illustrated in Fig. 3

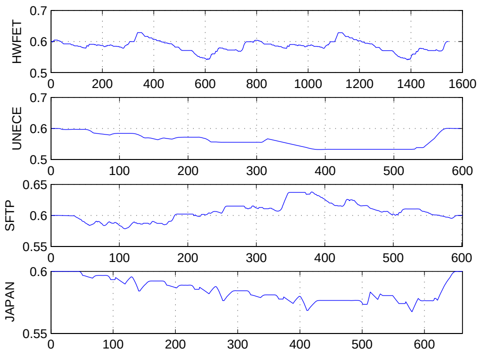

Fig. 3 SOC of battery in each driving schedules

Powertrain characteristics results are shown in Fig. 4-7. The solid squares refer to driving conditions where ED power is positive. The Dash-dotted squares correspond to batteries being recharged, and the dash squares refer to the engine supplying power. Upon further analysis, we can extract the following rules for proper power split on the hybrid powertrain.

For vehicle speed less than 18 km/hr, only the ED supplies the propelling power as shown in Fig. 4.

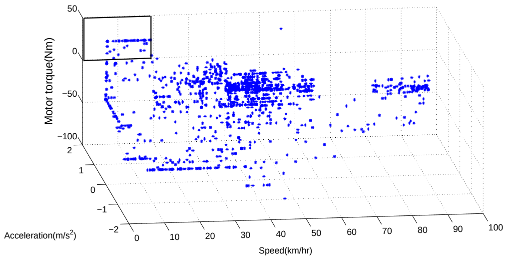

Fig. 4 The ED supplies power during acceleration and speed below 18 km/hr

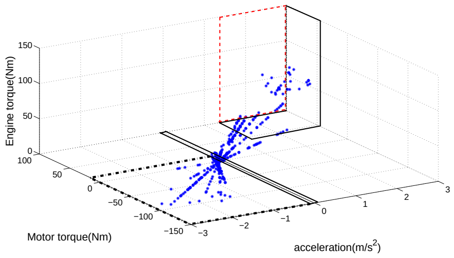

Fig. 5 Power spilt depends on acceleration rate

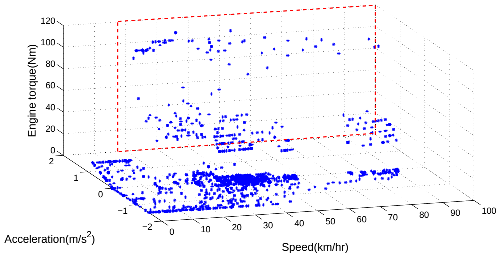

Fig. 6 Engine supplies power for speed increasing higher than 18 km/hr

Once the vehicle is over 18 km/hr: only engine supplies power when vehicle accelerates less than 1.5 m/s^2, but both supply the power when acceleration rate is higher than 1.5 m/s^2 as shown in Fig. 5 and Fig. 6. During the constant speed, only the ED supplies the power. During the deceleration, the regenerative braking occurs, where the ED converts the extra kinetic energy into the battery charging power. The charging also occurs for positive but decreasing acceleration rate as the extra engine energy recharges the battery as shown in Fig. 7.

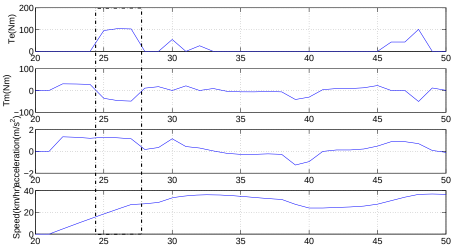

Fig. 7 Vehicle and powertrain characteristics for UDDS

VI. CONCLUSION

This paper has computed the fuel economy of a parallel hybrid electric vehicle with different numbers of LiFePO4 battery packs connected to an electric drive (ED), and a gasoline engine. The vehicle performance was evaluated against five standard driving schedules. The overall SOC variation is less than 10 percent from the nominal level prolonging the battery state of health. The results obtained from the dynamic programming approach have revealed that the set of 4 battery packs, total capacity of 1.3 kWh, is the most appropriate option. Note that finer grids on the state and the control have been tried but insignificant change in the result was observed. The rules for proper power split on the hybrid powertrain depending on the acceleration rate and the driving speed were also extracted. This information could be used to improve the HEV control strategy onboard

REFERENCES

[1] K. Uthaichana, S. Bengea, R. DeCarlo, S. Pekarek, and M. Žefran, "Hybrid model predictive control tracking of a sawtooth driving profile for an HEV," in *Proceedings of the American Control Conference*, Seattle, WA, 2008, pp. 967-974.

[2] C.-C. Lin, P. Huei, J. W. Grizzle, and K. Jun-Mo, "Power management strategy for a parallel hybrid electric truck," *IEEE Trans. Control Syst. Technol.*, vol. 11, pp. 839-49, 2003.

[3] G. Rizzoni, L. Guzzella, and B. M. Baumann, "Unified modeling of hybrid electric vehicle drivetrains," *IEEE/ASME Transactions on Mechatronics*, vol. 4, pp. 246-257, 1999.

[4] A. Fadel and B. Zhou, "An experimental and analytical comparison study of power management methodologies of fuel cell-battery hybrid vehicles," *Journal of Power Sources*, vol. 196, pp. 3271-3279, 2011.

[5] P. Thounthong, S. Raul, and B. Davat, "Energy management of fuel cell/battery/supercapacitor hybrid power source for vehicle applications," *Journal of Power Sources*, vol. 193, pp. 376-385, 2009.

[6] S. Pang, J. Farrell, J. Du, and M. Barth, "Battery State-of-Charge Estimation," in *American Control Conference*, Arlington, VA, 2001.

[7] P. Rong and M. Pedram, "An analytical model for predicting the remaining battery capacity of lithium-ion batteries," in *Design Automation and Test in Europe Conference and Expositions*, 2003, pp. 1148-1149.

[8] J. Van Mierlo, P. Van den Bossche, and G. Maggetto, "Models of energy sources for EV and HEV: fuel cells, batteries, ultracapacitors, flywheels and engine-generators," *Journal of Power Sources*, vol. 128, pp. 76-89, 2004.

[9] V. Agarwal, K. Uthaichana, R. A. Decarlo, and L. H. Tsoukalas, "Development and validation of a battery model useful for discharging and charging power control and lifetime estimation," *IEEE Transactions on Energy Conversion*, vol. 25, pp. 821-835, 2010.

[10] W. B. Powell, "What you should know about approximate dynamic programming," *Naval Research Logistics*, vol. 56, pp. 239-249, 2009.

[11] T. Bradley, "Modeling, design and energy management of fuel cell systems for aircraft," Georgia Institute of Technology, Georgia Institute of Technology, United States -- Georgia, 2008.